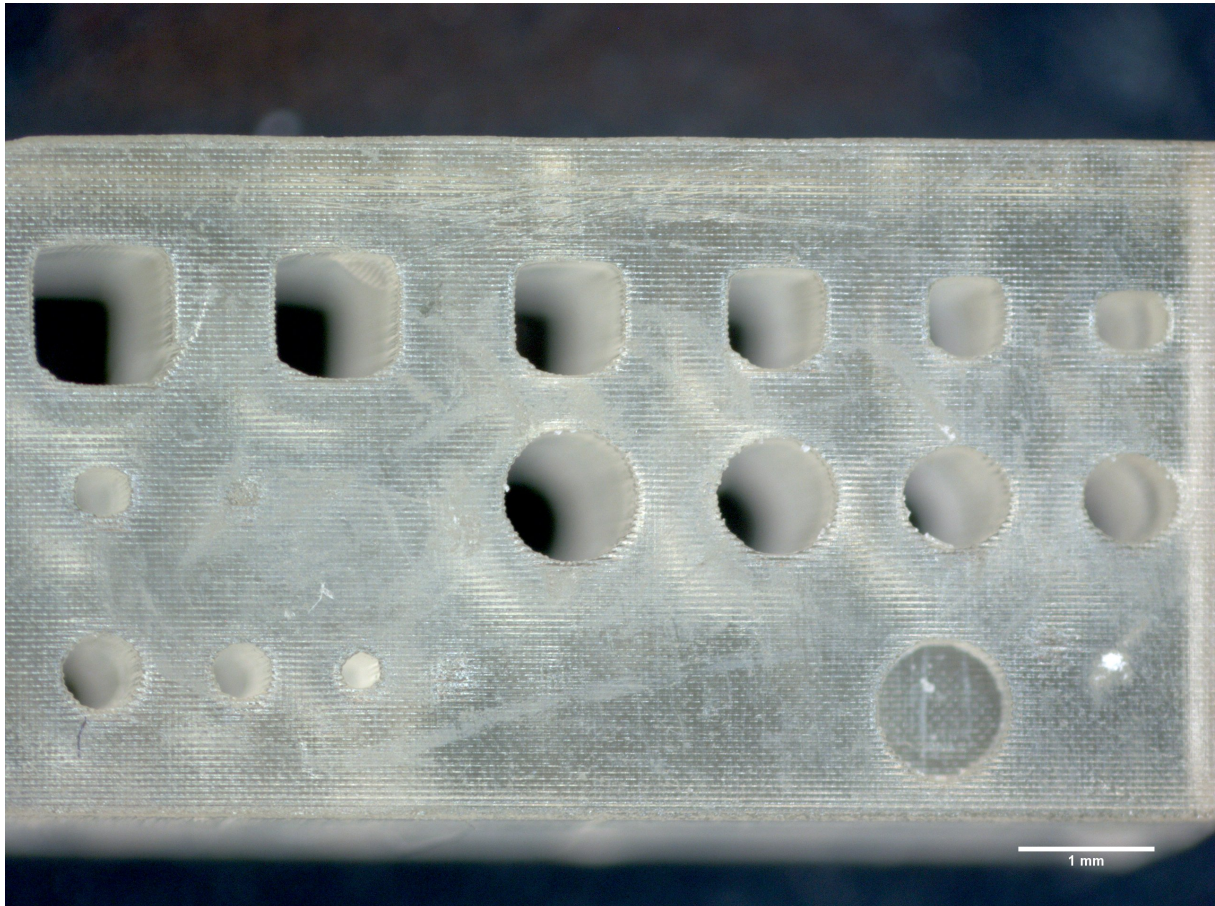


# *Rapid Prototyping of Microfluidic Systems using 3D Printing*

---



Authors:

Bjarke Nørrehvedde Jensen  
Thor Lindgren Videbæk Pedersen

3<sup>rd</sup> AND 4<sup>th</sup> SEMESTER

GROUP 5.317 B

NANOBIOTECHNOLOGY

AALBORG UNIVERSITY

3<sup>rd</sup> OF JUNE 2020





**AALBORG UNIVERSITY**  
STUDENT REPORT

**Title:**

Rapid Prototyping of Microfluidic Systems  
using 3D Printing

**Project:**

Nanobiotechnology 3<sup>rd</sup> and 4<sup>th</sup> Semester

**Project Period:**

September 2019 - June 2020

**Projectgroup:**

5.317 B

**Participants:**

Bjarke Nørrehvedde Jensen  
Thor Lindgren Videbæk Pedersen

**Supervisor:**

Leonid Gurevich  
Peter Fojan

**Total Page Number: 101**

**Appendix: Page 99-101**

**Finished: 03.06.2020**

**Third/Fourth Semester, Department of  
Materials and Production**

Nanobiotechnology

Skjernvej 4A

9220 Aalborg

<http://www.nano.aau.dk>

**Abstract:**

The purpose of this master thesis project is to explore the limitations of a commercially available 3D printer for the use in printing microfluidic systems. The custom designed microfluidic systems are simulated, printed, tested, and evaluated. The achievable minimum feature size, chemical leaching, and solvent/acid resistance was tested. The designed microfluidic systems could be printed using the chosen 3D printer. The microfluidic systems designed for chemotaxis of *C. elegans* showed promise in the simulations, but failed the experimental testing. The flow focusing droplet generator design was successfully incorporated into an electrospinning setup for continuous electrospinning of emulsions into beads-on-a-string fibers.

---

# Preface

---

This report is written by group 5.317B in the autumn and spring semester of 2019/2020 from the 4<sup>th</sup> of September 2019 to the 3<sup>rd</sup> of June 2020. It was developed as a master thesis in the 3<sup>rd</sup> and 4<sup>th</sup> semester of the masters program of Nanobiotechnology, at the Department of Materials Science and Engineering at Aalborg University. The report describes the optimal printing settings of the Anycubic DLP 3D printer, leaching of unknown compounds from 3D prints, simulating the assumption of a smooth channel surface, surface coating and treatments, and a test of the corrosion and solvent resistance of the DLP resin used in the project. Three different microfluidic systems are designed, simulated, printed, and tested to evaluate the use of a commercially available 3D DLP printer. Two of the microfluidic systems are designed for the use in chemotaxis experiments with *C. elegans*. The third microfluidic system is a droplet generator design used in conjunction with an electrospinning setup for continuous electrospinning of emulsions into fibers.

Citations are written as numbers in brackets which relates to a specific source in the bibliography. These sources list the shortened name and surname of the authors, title, journal, volume, page numbers, and year of publication listed in this order. In cases of three or more authors, the first author's name is written followed by et al. All gene names are written in italic. Figures without references were created by the authors of this report. Both figures, equations, and tables are numbered in ascending order, separately. The group had Leonid Gurevich and Peter Fojan, both associate professors at the Department of Materials Science and Engineering, as supervisors for this project.

Bjarke N. Jensen

Bjarke Jensen

Thor Pedersen

Thor Pedersen



---

# Abbreviations and Constants

---

## Glossary

- 3D - 3 dimensional
- CAD - Computer aided design
- DLP - Digital light processing
- DMD - Digital micromirror device
- DNA - Deoxyribonucleic acid
- GB - Gigabyte
- LCD - Liquid crystal display
- LCoS - Liquid crystal on silicon
- MEQ - Minimum element quality
- MFS - Minimum feature size
- PCR - Polymerase chain reaction
- RAM - Random access memory
- SEM - Scanning electron microscope
- SLA - Stereolithography
- Std. - Standard deviation
- stl - Stereolithography (file format)
- UV - Ultraviolet
- WJ - Worm junction

## Chemical Compound & Names

- DCM - Dichloromethane
- DMF - Dimethylformamide
- HCl - Hydrochloric acid
- NMP - N-Methyl-2-pyrrolidone
- NPS - 2-nitrophenyl phenylsulfide
- PCL - Polycaprolactone
- PDMS - Polydimethylsiloxane
- PEGDA - Poly(ethylene glycol) diacrylate
- PSN - Polyureasilazane
- PVA - Polyvinyl alcohol
- SDS - Sodium dodecyl sulfate



---

# Contents

---

<b>1</b>	<b>State of the Art</b>	<b>1</b>
<b>2</b>	<b>Theory</b>	<b>5</b>
2.1	3D Printing . . . . .	5
2.2	Resins for 3D printing . . . . .	8
2.3	Cytotoxicity of 3D SLA and DLP prints . . . . .	9
2.4	Fluid-flow simulations . . . . .	10
2.4.1	Reynolds number . . . . .	10
2.5	Chemotaxis of <i>Caenorhabditis elegans</i> . . . . .	11
2.6	Electrospinning . . . . .	12
<b>3</b>	<b>Materials and Methods</b>	<b>17</b>
3.1	Materials . . . . .	17
3.2	Anycubic Photon DLP 3D Printer . . . . .	18
3.3	File preparation for 3D printing . . . . .	18
3.4	Post 3D Print Processing . . . . .	19
3.5	Minimum Feature Size . . . . .	19
3.6	COMSOL simulations . . . . .	20
3.6.1	Meshing . . . . .	20
3.6.2	Structure optimization . . . . .	20
3.6.3	Droplet Generator Simulations . . . . .	21

3.7	Worm Junction Experiments . . . . .	22
3.8	Gradient generator . . . . .	22
3.9	Droplet Generator . . . . .	23
3.10	Electrospinning . . . . .	23
3.11	Solvent Experiments . . . . .	24
3.12	Leaching Experiment . . . . .	25
<b>4</b>	<b>Results and Discussion</b>	<b>27</b>
4.1	Minimum Feature Size . . . . .	27
4.2	Surface Roughness Effect on Flow . . . . .	36
4.3	Surface Treatment and Coating . . . . .	39
4.4	Solvent Experiments . . . . .	41
4.5	Leaching Experiments . . . . .	42
4.6	Worm Junction - Chemotaxis . . . . .	46
4.6.1	Simulations of Worm Junction - Chemotaxis . . . . .	47
4.6.2	Worm Junction Print . . . . .	49
4.6.3	Fluorescein Experiments . . . . .	51
4.7	Gradient generator and chamber . . . . .	53
4.8	Droplet Generator . . . . .	67
4.8.1	Droplet Generator Experiment . . . . .	68
4.8.2	Simulating the Droplet Generator . . . . .	72
4.9	Electrospinning . . . . .	75
<b>5</b>	<b>Conclusion</b>	<b>85</b>

<b>6</b>	<b>Future Implications</b>	<b>87</b>
	<b>Bibliography</b>	<b>89</b>
<b>7</b>	<b>Appendix</b>	<b>99</b>

---

# 1. State of the Art

---

The usage of 3 dimensional (3D) printing is in rapid development for implementation in many different fields due to manufacturing benefits such as faster production times, less material waste, production of complex geometries, and the ability to print unique multi-material configurations [1].

A group from RWTH Aachen used 3D printing for rapid prototyping of a parallelized microfluidic droplet generator for the use in preparing monodisperse microgels [2]. Since droplet generators usually only have one generating channel the throughput is low, so parallelization of the channels would serve as a mean of increasing the throughput. This has already been achieved through careful stacking and alignment of PDMS layers at a cost of difficult production and inefficient use of space as long distribution channels were required to ensure proper distribution of flow [3]. The group developed a successful compact channel stacking design going from 3 stacked channels to 28 stacked channels which was enabled through the use of 3D printing. The stacked droplet generator was able to create monodisperse droplets with a diameter of  $500\ \mu\text{m}$ , and the group postulated that a higher density of smaller channels, and thus smaller droplets with a similar accumulated throughput, can be created by using two-photon 3D lithography [2].

A group from Brigham Young University developed and built a custom digital light processing (DLP) 3D printer capable of reliably fabricating flow channels with dimensions as small as  $18\ \mu\text{m} \times 20\ \mu\text{m}$ , after finding that most commercially available 3D printers are unable to create true microfluidic flow channels ( $<100\ \mu\text{m}$ ). The small channel dimensions was achieved through the use of a  $2560 \times 1600$  micromirror array resulting in an image plane resolution of  $7.6\ \mu\text{m}$  and a projected area of  $19.35 \times 12.10\ \text{mm}^2$  when using a 1:1 imaging system. Larger effective printing areas could be achieved through translating the light engine in the XY plane. The group developed a new resin using 2-nitrophenyl phenyl sulfide (NPS), a UV photoabsorber suitable for printing small channels that was soluble in PEGDA. Exposing the edge of the channels an additional time after the primary exposure allowed for additional control over the dimensions of the resulting channels [4].

A small collection of microfluidic systems developed using rapid prototyping with 3D printers can be seen in Table 1.1.

Table 1.1: 3D printed microfluidic system and their applications. Based upon the article by Chenpeng *et. al.* [5].

<b>Minimum feature size</b> (X/Y, Z)	<b>Printer</b>	<b>Printer resolution specifications</b> (X/Y, Z)	<b>Application</b>
1 mm, -	Projet HD 3500 Plus	30 $\mu\text{m}$ , -	Fluidic components for alpha-fetoprotein detection [6].
3 mm, 1.5 mm	Objet Connex 350	42 $\mu\text{m}$ , -	Monitored drug transport with cells [7].
500 $\mu\text{m}$ , 1 mm	Miicraft	50 $\mu\text{m}$ , 100 $\mu\text{m}$	Components for Protein quantitation [8].
220 $\mu\text{m}$ , 220 $\mu\text{m}$	Shapeways print service	25 $\mu\text{m}$ , 100 $\mu\text{m}$	DNA ligation and PCR [9].
500 $\mu\text{m}$ , 500 $\mu\text{m}$	Ultimaker 2 and Miicraft	- , 100 $\mu\text{m}$	Droplet generator for cell encapsulation [10].
500 $\mu\text{m}$ , -	Perfactory Minimultilense	32 $\mu\text{m}$ , 30 $\mu\text{m}$	Droplet generators array for monodisperse microgels [2].
250 $\mu\text{m}$ , -	Miicraft DMD	50 $\mu\text{m}$ , 50 $\mu\text{m}$	Mixer, droplet generator for nitrite detection [11].
300 $\mu\text{m}$ , 150 $\mu\text{m}$	B9 Creator	-, 50 $\mu\text{m}$	Active microfluidic valves [12].
162 $\mu\text{m}$ , 150 $\mu\text{m}$	Asiga Pico Plus	27 $\mu\text{m}$ , 1 $\mu\text{m}$	Multiplexed pump and valve system [13].
108 $\mu\text{m}$ , 60 $\mu\text{m}$	Asiga Pico Plus	27 $\mu\text{m}$ , 1 $\mu\text{m}$	Resin optimization to print true microfluidic channels [14].
20 $\mu\text{m}$ , 25 $\mu\text{m}$	Custom 3D printer	7.6 $\mu\text{m}$ , 8.3 $\mu\text{m}$	Resin optimization and custom built 3D printer [4].

As described above it is possible to use 3D printing for rapid prototyping of true microfluidic systems, but that commercially available 3D printers have their limitations. So, for a laboratory that is currently unable of going the optimal route of building a custom 3D printer, what are the limitations of a relatively cheap commercially available 3D printer for the use in rapid prototyping of microfluidic systems?

The project will be testing the limitations of a commercially available Anycubic Photon DLP 3D printer by designing and printing microfluidic systems using it. The

microfluidic systems will be simulated using the finite element simulation software COMSOL Multiphysics where the results will be used to compare the printed microfluidic systems. The microfluidic systems will be designed for two different applications; one for chemotaxis of *Caenorhabditis elegans* and one for droplet generation made for the use in electrospinning. In addition to designing and printing microfluidic systems, the limiting factors of print resolution and cleaning of printed channels will be addressed.



---

## 2. Theory

---

### 2.1 3D Printing

In general, manufacturing methods can be separated into two different categories; subtractive manufacturing (Top Down) and additive manufacturing (Bottom Up). With subtractive manufacturing the desired geometry is achieved by removing material from an initial block. Examples of this type of manufacturing method would be milling, turning, grinding, laser cutting, drilling, water jet cutting, and photolithography. For additive manufacturing the final geometry can be created by adding layers upon layers of material without removing any. Methods that can be classified as additive manufacturing are stereolithography (SLA), binder printing, inkjet printing, fused deposition modeling, selective laser sintering, and laminate object manufacturing [1].

Many of these additive methods are employed in 3D printing, which is already being applied in a variety of fields and is continuously becoming more readily available [15]. One of the methods is SLA, which was developed in 1986 by Charles Hull. The method uses an UV light source or an electron beam to initiate a polymerization reaction of photoactive resin or monomer solution, which is usually acrylic or epoxy-based, into polymers. When the polymerization reactions have finished and the layer has solidified in the desired pattern, a new layer of non-polymerized resin/monomer solution is added to form the next layer. This process is repeated until the final geometry is achieved whereafter the supports and non-polymerized resin is removed from the print [1, 15, 16, 17, 18]. Additional post-treatment of the print can be done in the form of heating or photo-curing to increase surface quality or to alter mechanical properties [1, 15]. Figure 2.1 shows a schematic representation of a SLA setup.

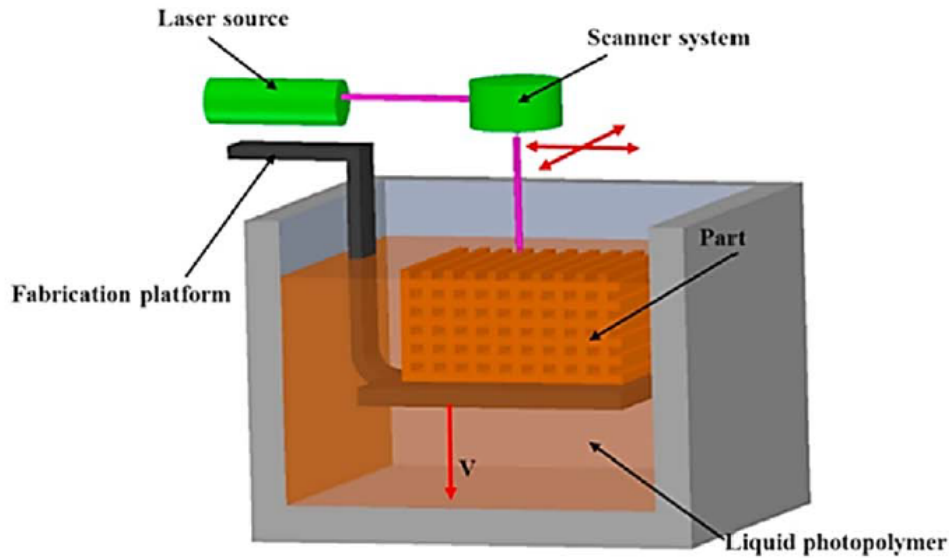


Figure 2.1: Schematic of the additive manufacturing method SLA [15].

SLA makes use of a laser and a scanner system making it possible to achieve a minimum feature size (MFS) as low as  $10\ \mu\text{m}$  without compromising the print quality [15]. SLA can make seamless layer-by-layer stacking since the layer thickness can be adjusted from  $1\ \mu\text{m}$  to  $50\ \mu\text{m}$  depending on the light source and the exposure of each layer. However, the layer thickness also constrains the resolution that can be achieved. The possible layer thickness is limited by the machines capabilities and the printing material [1, 15]. The resulting layer thickness is dependent on the printing parameters of the print such as exposure time, light intensity, and the concentration of the photo-absorber and photo-initiator in the resin [17, 19]. The exposure time and light intensity determines how much of the print material becomes polymerized. Too much exposure time and/or light intensity will lead to overcuring which results in poor surface quality and inaccurate dimension, whereas too little and the printed layers will not stick together [16]. The drawbacks of SLA printing are the limited available printing materials, the relatively slow printing time, usage of expensive materials, and the complex curing process during printing as well as the polymerization reaction kinetics [16, 17, 18, 20].

A newer method of 3D printing that is based on SLA is DLP 3D printing. With the new method a digital micromirror device (DMD), liquid crystal on silicon (LCoS), or liquid crystal display (LCD) is used instead of the scanner system used in SLA. The DMD is composed of thousands of moving micromirrors that can be in an on or off position, based

on the loaded images. This makes the DMD function as a dynamic mask, that reflects the light in the desired pattern, which via the optical system interacts with the resin causing it to polymerize. LCoS and LCD displays achieves the same as DMD by projecting the images and thus functioning as a dynamic mask. Additionally, the displays can use LEDs that have longer lifespan, low cost, compact size, and low heat dissipation compared to traditional lamps used for polymerization. Figure 2.2 shows a schematic representation of a DLP setup with a DMD.

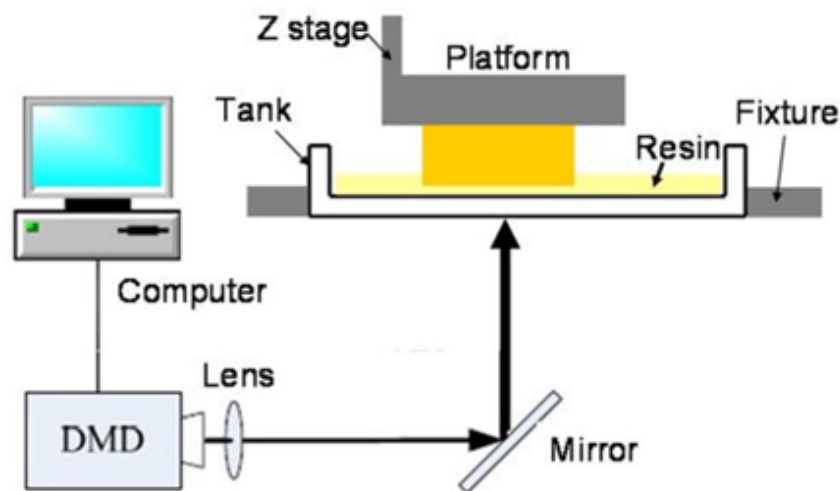


Figure 2.2: Schematic of a DLP 3D printing setup [16].

By changing to the DMD, LCoS, or LCD a whole layer can be exposed simultaneously instead of exposing every point individually, drastically reducing the printing time [16, 17, 18, 19]. This change allows operation within a wide range of wavelengths, and usage of a variety of resins that can be customized for unique specifications. However, this introduces the resolution of the DMD, LCoS, or LCD, as a limiting factor in the possible achievable MFS [19]. Except for these changes the same difficulties that SLA have are also present for DLP 3D printing. One of these difficulties that is most important is the control of the MFS. For many commercially available printers it is currently almost impossible to achieve true microfluidic channels ( $<100 \mu\text{m}$ ), and are often only able to create voids in the large microfluidic regime ( $100\text{-}500 \mu\text{m}$ ). To get in the true microfluidic range it would require specialized equipment setups and printing materials [1, 15, 19, 21, 22, 23].

## 2.2 Resins for 3D printing

Just as important as the mechanical specifications of the 3D printer is in setting the limitations of the possible MFS of 3D prints, so is the chemical composition of the resin. The resin is monomer and/or epoxy based together with a photoinitiator and/or photoabsorber. The chemical composition of the resin determines the possible MFS, chemical resistance, structural hardness, Young's modulus, optical transparency, and the cytotoxicity of the print [24].

The printing resin is based on photopolymers of crosslinking mono-, di-, and trifunctional monomers and of hyperbranched oligomers that function as both diluents and cross-linkers [24, 25, 26]. Some printing resins employ a mixture of acrylate polymers and epoxy polymers to create interpenetrating polymer networks that modify the material properties into what is desired. The resulting prints have reduced shrinkage, higher accuracy in printing, are more chemically resistant, and are stronger as they overcome the limitations of single polymer systems [24, 27, 28].

Photoinitiators are molecules that generate reactive species like cations or free radicals through the absorption of light, usually in the range of 250 nm to 450 nm matching the light source of the 3D printer. These reactive species are what initiates the polymerization chain reaction that solidifies the resin [29, 30]. The important parameters of photoinitiators is the reactivity (excited state production, reactivity of the initiating species, and efficiency of the interaction processes) and the absorption properties (absorption spectra and molar extinction coefficients) [30]. Additionally, they must be soluble in the printing resin [23].

Photoabsorbers are used in 3D printer resin to reduce the penetration depth of light into the resin during printing. Without photoabsorbers the light will be spread and penetrate further than wanted causing polymerization of resin in places that should otherwise become voids [26]. One solution to reduce exposure of void regions is to reduce the layer exposure time, but this has the unintended side effect of reducing the crosslinking of the layer and therefore also the hardness and Young's modulus of the layer [23]. Therefore, a good photoabsorber has a high spectral overlap with the light source resulting in an as small penetration depth as possible and thus a smaller possible layer thickness of the

print. H. Gong *et. al.* has made a paper that describes a useful model that relates the polymerization depth to the exposure time, resins absorption coefficient, and the spectral overlap. The model is used for finding the photoabsorber that achieves the best printing results for the given resin composition and can be used for designing new resins [23].

## 2.3 Cytotoxicity of 3D SLA and DLP prints

The biocompatibility of microfluidic systems fabricated using 3D printing is critical for the use in biological and biomedical applications. Leaching of chemicals from the 3D print becomes a prevalent issue in bioassays as they are conducted in aqueous media. One of the complications in determining the biocompatibility of 3D resins is the lack of information on the chemical composition of commercially available resins, as the manufactures only reports known hazardous materials in the safety data sheet. Additionally, research of open source and patent documents indicates that the formulas are complex with some containing more than 20 compounds making predicting the cytotoxicity difficult [24, 31].

In general compounds are released from polymerized objects through two principal mechanisms; through erosion/degradation and through leaching into aqueous medium [32]. Erosion of the polymerized object may be caused by thermal, mechanical, photo, or chemical factors, ex. if the object is dissolvable in the solvent used in the experiment the object is intended for [24, 32]. Leaching of residual compounds from polymerised objects into aqueous solutions is dependent upon the geometry of the printed object, the characteristics of the resin components, and upon the extent of polymerization [33]. The degree of conversion of monomers into polymers in resins is reported to be under 80%, and that the rate of leaching is found to be highest in the first 24 hours of contact with an aqueous medium [34, 35].

A reduction in cytotoxicity has been achieved through an introduction of a post-curing step in the fabrication of objects 3D printed using photopolymer resins. The post-curing step reduces the cytotoxicity through either reacting unreacted components under UV light (UV-curing), or through letting the potentially toxic compounds leach out before use (sonication and/or soaking in water) [24, 36, 37, 38]. The effectiveness of UV-curing may vary from print to print as some areas may receive more or less UV light depending

upon the geometry of the print [24].

## 2.4 Fluid-flow simulations

Fluid-flow through a microfluidic system can be simulated using finite-element analysis softwares such as COMSOL Multiphysics. The calculations of fluid-flow is based upon the Navier-stokes equations that describe the motion of fluid and can be seen as the fluid equivalent of Newtons second law of motion, see Equation 2.1.

$$\rho \frac{\partial \mathbf{u}}{\partial t} + \rho(\mathbf{u} \cdot \nabla)\mathbf{u} = \nabla \cdot [-p\mathbf{I} + \mu(\nabla\mathbf{u} + (\nabla\mathbf{u})^T)] + \mathbf{F} \quad (2.1)$$

Equation 2.1 is the Navier-Stokes equation for incompressible fluids which relates inertial forces, pressure forces, viscous forces, and the external forces applied to the fluid [39]. The equations are solved together with the continuity equation that describes the conservation of mass, see Equation 2.2:

$$\frac{\partial \rho}{\partial t} + \nabla \cdot (\rho\mathbf{u}) = 0 \quad (2.2)$$

While the continuity equation describes the conservation of mass, the Navier-Stokes equation describes the conservation of momentum [39].

### 2.4.1 Reynolds number

Reynolds number is a measure of how turbulent a given flow is and is used in microfluidics to determine if the flow is laminar or turbulent enough for the given purpose of the microfluidic cell [39]. The number is the ratio of inertial forces to viscous forces, see equation 2.3.

$$\mathbf{Re} = \rho u L / \mu \quad (2.3)$$

Here  $u$  is the velocity,  $L$  is the representative length, and  $\mu$  is the viscosity. The flow is creeping for Reynold numbers  $\text{Re} < 1$ , laminar for  $1 < \text{Re} < \approx 2000$ , and turbulent for  $\text{Re} > 2000$ . For small Reynold numbers the viscous forces dominates resulting in a

dampening effect that reduces or prevents disturbances, but as the velocity increases or viscosity decreases, so does the dampening effect resulting in turbulence [39].

## 2.5 Chemotaxis of *Caenorhabditis elegans*

*C. elegans* are widely studied nematodes that are used as a model organism for the study of neural development as its neural system comprises of only 302 neurons [40, 41]. It has chemosensory neurons situated on both ends of its approximately 1 mm long body in the amphid, phasmid, and inner labial sensory openings [42, 43]. Their highly developed chemosensory system that allows them to detect water-soluble (gustatory) and volatile (olfactory) compounds associated with danger, food, or other animals. The chemosensory cues can elicit chemotaxis, changes in overall motility, rapid avoidance, and entry into or exit from alternative dauer developmental stages [43]. Additionally, *C. elegans* can integrate context and experience into its behavior by modifying its chemosensory preference through sensory adaptation, developmental history, and associative learning [44]. The movement pattern of *C. elegans* in liquid consists of C, l, S, and rarely O shapes. It moves with rare, brief pauses of 50-100 ms resulting in an approximate speed of 2.4 mm/s. As the nematode moves both forward and backwards while swimming, it has been noted that much of the distance covered is cancelled by movement in the opposite direction [42].

Chemotaxis is the movement of cells or microorganisms in response to a chemical gradient with the goal of seeking an energy source or to avoid a fatal situation [45]. The standard method of chemotaxis of *C. elegans* is based on a plate assay due to its simplicity and ease of use. The nematodes are placed on a plate with a chemical compound of interest. They then move to their optimum chemical gradient where they are immobilized by sodium azide. The method has the downside of having to optimize the starting location to both the control and test areas, while still maintaining a significant sample size without causing too much interaction between the worms [46, 47]. One way of increasing the throughput of the assay while maintaining minimal interaction between each worm is by swapping to a microfluidic assay. The nematodes can be injected into the microfluidic system continuously, as it can be designed as a sorting system that "ejects" the nematodes in an outlet corresponding to their optimum chemical concentration [45, 48, 49, 50]. An example

of a chemotaxis microfluidic system designed by Hwang *et. al.* can be seen in Figure 2.3.

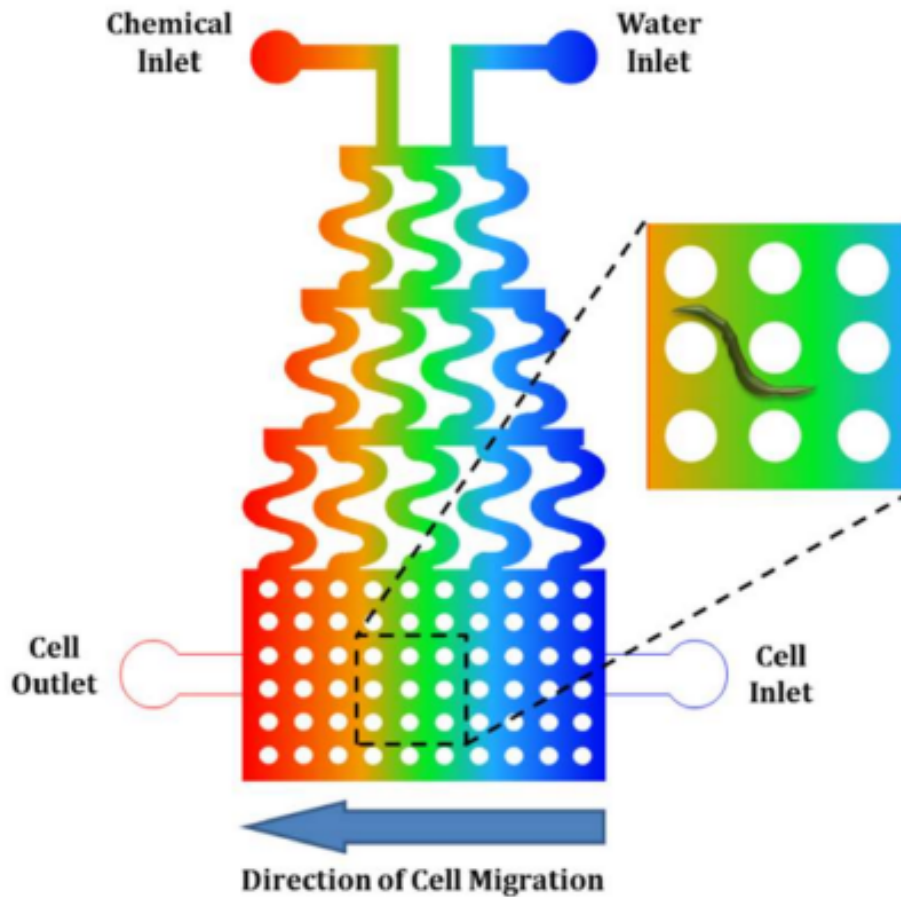


Figure 2.3: A microfluidic device designed for chemotaxis of *C. elegans*. The chemical gradient is generated using a serpentine design, and the pillars are used to mimic dirt and colloids inside soil [45, 48].

## 2.6 Electrospinning

Electrospinning is an electrohydrodynamic process, where a liquid droplet is charged forming a Taylor cone, generating a jet that as it travels undergoes stretching resulting in the formation of fibers. The basic setup used for electrospinning consists of a high-voltage power supply, a conductive collector, a syringe pump, and a spinneret, which usually is a blunt-tip hypodermic needle [51]. The process of electrospinning can in general be divided into four steps:

(1): Deformation of the liquid droplet into a Taylor cone as charge is accumulated on the surface of the droplet until the point where the electrostatic repulsion equals the surface tension and viscoelastic force of the liquid.

(2): Extrusion and extension of a straight charged jet from the Taylor cone continuing as long as an adequate amount of liquid is supplied to the cone.

(3): Thinning of the jet and increased bending instability (whipping instability) caused by the applied electric field where stronger electric fields cause higher whipping instability, and thus more jet thinning.

(4): Solidification of the jet as the solvent evaporates, and collection of the fibers on the grounded plate where the morphology of the fibers are determined by the stage of whipping instability at which the fibers are collected [51].

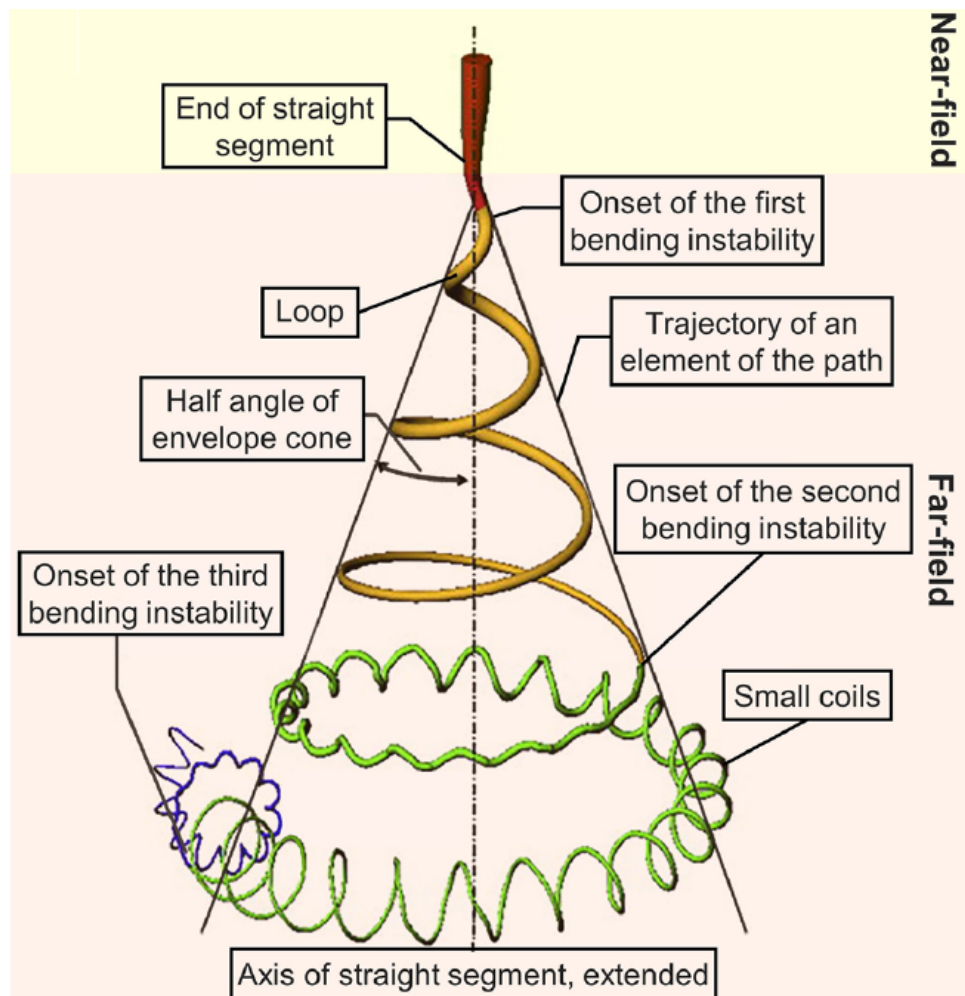


Figure 2.4: Diagram showing the movement and states the jet undergoes as it travels from the Taylor cone. Near-field is 0 mm to 5 mm and far field is >5 mm [51].

The morphology of the fibers can be largely controlled through adjustments of the processing parameters; applied voltage, flow rate of the liquid, and the distance between the tip of the spinneret and the collector [51]. Higher voltages tends to form thinner fibers

as it pulls harder on the jet, but may have the side effect of also pulling out more material resulting in thicker fibers [52, 53]. An increase in flow rates generally results in thicker fibers as more material is readily pulled. The distance between the spinneret and the collector plate determines at what stage of instability the fiber is collected with thinner but more chaotically orientated fibers at longer distances [51].

Additional parameters that can be adjusted are the solvent volatility and dielectric constant and the polymer concentration and electrical conductivity in addition to environmental parameters such as relative humidity, solvent vapor saturation, and temperature. The solvent volatility influences how quickly the solvent evaporates, so if it is too high the jet may solidify almost immediately upon leaving the spinneret. If it is too low the fibers may still be wet upon reaching the collector [51]. The dielectric constant of the solvent influences the accumulation of charge on the surface of the jet, so with an increasing dielectric constant an increase in applied voltage is required to achieve a stable jet [54]. The polymer concentration influences the viscosity and surface tension of the polymer solution. A lower polymer concentration favors thinner fibers, but if it becomes too low no fiber will be produced. Likewise, if the viscosity becomes too high it becomes difficult to eject the solution from the spinneret. The conductivity of the polymer solution affects the accumulation of charge on the surface of the droplet. A too low conductivity prevents charge from moving from the center of the solution to the surface. A too high conductivity prevents charge from staying on the surface of the droplet. Both a too high and too low conductivity results in no formation of a Taylor cone and subsequent jet ejection [55, 56]. The conductivity can be adjusted through the addition of ionic compounds such as salts [57]. The relative humidity and temperature affects the rate of solvent evaporation, thus resulting in similar effects as low and high solvent volatility [58]. The ambient temperature also affects the surface tension and viscosity of the polymer solution, with both being reduced at elevated temperatures resulting in thinner fibers. If the temperature becomes too high the solvent evaporates too quickly negating the thinner fiber effect previously stated [59]. The inner diameter of the spinneret tip influences the fiber diameter by decreasing the initial jet as the inner spinneret tip diameter decreases resulting in thinner fibers [60, 61]. This correlation is also observed for near-field electrospinning [62].

Electrospinning with solutions containing particles or emulsions tends to form fibers with bead-like structures situated inside or outside the fiber depending on the conditions [63, 64, 65, 66]. The dispersed phase is situated on the inside of the fiber when electrospinning emulsions, see Figure 2.5. It has been proposed that the dispersed phase has a tendency to accumulate at the center of the jet during the elongation phase of electrospinning [63].

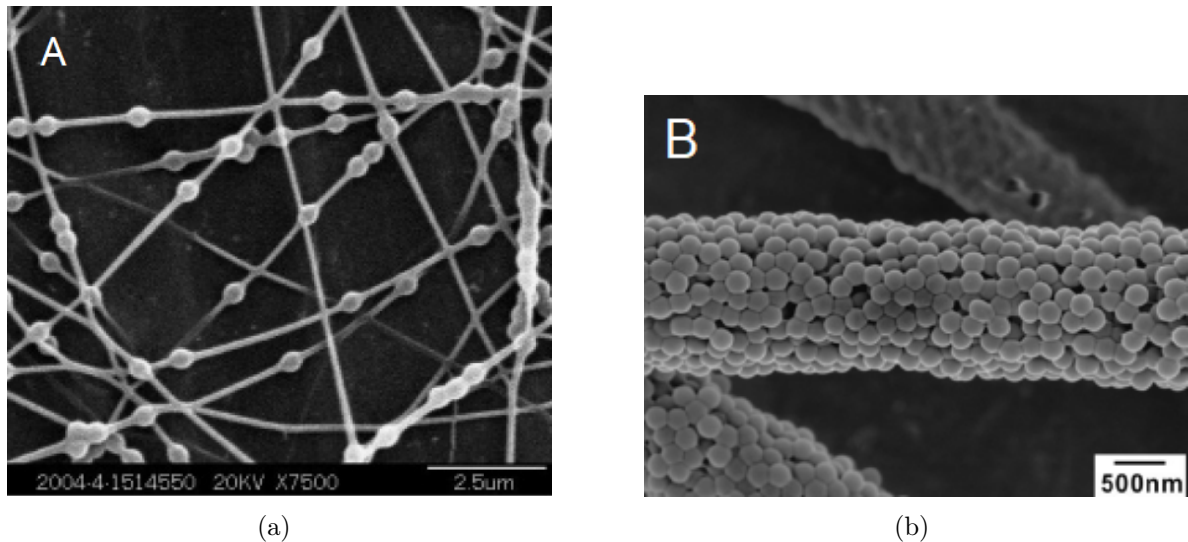


Figure 2.5: (a): SEM image of 10% PVA fibers spun with Ca-alginate emulsion [63]. (b): PVA/PSN fibers at a weight ratio of 1:4 [66].



---

## 3. Materials and Methods

---

### 3.1 Materials

Table 3.1: List of chemicals used for the experiments.

<b>Chemical</b>	<b>Cas no.</b>	<b>Lot no.</b>	<b>Supplier</b>
1-Butanol	71-36-3	SHBB2622V	SIGMA-ALDRICH
Acetic acid	64-19-7	STBH0492	SIGMA-ALDRICH
Acetone	67-64-1	19C054006	VWR Chemicals
Acetonitrile	75-05-8	18C291590	VWR Chemicals
Dichloromethane	75-09-2	V7L562087M	Iris Biotech GmbH
Dimethylformamide	68-12-2	145129B	Iris Biotech GmbH
Ethanol	64-17-5	18L204014	VWR Chemicals
Ethanolamine	141-43-5	045K0644	SIGMA-ALDRICH
Ethylacetat	141-78-6	—	SIGMA-ALDRICH
Fluorescein	2321-07-5	452981	SIGMA-ALDRICH
Grape seed oil	—	—	Coop
Hydrochloric acid	7647-01-0	I3520	Honeywell
Isopropanol	67-63-0	19304005	VWR Chemicals
Methylcyclohexane	108-87-2	STBG5592V	Honeywell
N-Methyl-2-pyrrolidone	872-50-4	26651	Advanced ChemTech
Nile red	7385-67-3	BCCC2326	SIGMA-ALDRICH
Nitric acid (65%)	7697-37-2	SZBC3130V	SIGMA-ALDRICH
1-Octadecene	112-88-9	MKBD0024	SIGMA-ALDRICH
Phosphoric acid (85%)	7664-38-2	BCBG9726V	SIGMA-ALDRICH
Value Clear DLP Resin	—	—	PrimaCreator
Polyvinyl alcohol $M_w$ 89-98	9002-89-5	MKBC5520	SIGMA-ALDRICH
Tetrachloroethylene	127-18-4	SZBC1800V	SIGMA-ALDRICH
Triethylamine	121-44-8	BCBD4896V	SIGMA-ALDRICH

Table 3.2: Equipment used for the experiments.

Device	Description	Supplier
3D Printer	Anycubic Photon DLP	Anycubic
Inverted Microscope	IX71	OLYMPUS
Microscope Camera	Axiocam 105 Color	ZEISS
Quartz Suprasil High Performance Cell	10 mm pathway	Hellma
Single Syringe Pump	Model NE-1010	New Era Pump Systems
Stereo Microscope	Stemi 508	ZEISS
Transilluminator (UV lamp)	Model BTS-20.LM	UVitec
UV-VIS spectrophotometer (UV-1800)		Shimadzu
Electrospinner	Custom setup	-

## 3.2 Anycubic Photon DLP 3D Printer

All the 3D printed structures are printed using the Anycubic Photon DLP 3D printer.

The technical specifications for the printer are listed in 3.3.

Table 3.3: Technical specifications of Anycubic Photon DLP 3D printer.

Parameter	Name/Value
Printer Technology	DLP
Printer Technique	LCD Shadow Masking (Dynamic Mask)
Light-source	Integrated UV-LED 25 W (405 nm)
XY Resolution	47 $\mu\text{m}$ (2560x1440)
Z-axis Accuracy	1.25 $\mu\text{m}$
Suggested Layer Thickness	25-100 $\mu\text{m}$
Suggested Print Speed	10-18 mm/hr
Rated Power	40 W
Materials	405 nm UV-resin
Printing Volume	115mm x 65 mm x 155 mm

## 3.3 File preparation for 3D printing

The parts used for the experiments have been designed/drawn using Autodesk Inventor Professional 2020. After drawing the part in Inventor the part is converted into a stl-file so it can be opened in the slicer program Anycubic Photon Slicer64. The slicer program is used to add, rotate, and/or scale the structures and to add supports to the structure

before slicing. The most optimal printing angle and support position is evaluated on a structure to structure basis. When the slicing is done the file is ready to be transferred to the 3D printer.

The structures are printed using the Anycubic Photon DLP 3D printer with clear PrimaCreator Value Clear DLP Resin. A slice thickness between 10  $\mu\text{m}$  and 50  $\mu\text{m}$  is used with an exposure time between 6 and 8 seconds and an off time of 6.5 seconds. The first eight layers have an exposure time of 70-90 seconds.

## 3.4 Post 3D Print Processing

After a 3D print is complete the parts are removed from the printing platform followed by the removal of the support structures from the parts. Any channels in the structure are cleaned by blowing high-pressure nitrogen into the channel pressing out any non-polymerized resin. The parts are then submerged and flushed using isopropanol to remove non-polymerized monomers followed by a wash using water and a nitrogen blow drying. Afterwards the parts are put on the windowsill for multiple hours or under a transilluminator BTS-20.LM 312 nm UV lamp for 15-30 minutes to fully polymerize. When the residual resin on the parts have polymerize the parts can be coated to achieve transparency using either hairspray, clear resin, clear coat nail polish, or polishing with high grain sandpaper followed by applying clear tape.

## 3.5 Minimum Feature Size

To investigate the achievable MFS, a series of prints with varying channel sizes ranging from 0.1 mm to 1 mm was designed. Additionally parameters that could affect the MFS was also varied. The additional parameters that are tested is channel design (circular, square channels), layer thickness, angle to the building platform and exposure time. The prints were prepared using the methods in Section 3.3 and Section 3.4. After taking a snapshot of the prints with a Stemi 508 stereo microscope and an Axiocam 105 Color the channel dimensions were measured using ImageJ.

## 3.6 COMSOL simulations

The parts were simulated using the finite element simulation program COMSOL Multiphysics version 5.5. The structures were drawn and designed in Autodesk Inventor and exported into COMSOL Multiphysics as a CAD file.

### 3.6.1 Meshing

The optimal mesh for each simulated part was found by making a series of simulation with an increasing number of meshing elements. The results were evaluated through the continuity equation, as the flow at the center of the structure should be equal to the flow at the inlets. The estimated error was found by calculating the difference between the volumetric flow at the center of the simulated structure and at the inlets/outlets. The error estimation was plotted versus the number of meshing elements, and the point at which no further significant error reduction can be achieved through the increase in number of meshing elements was estimated. The resulting number of meshing elements was then used for further simulations. Based on recommendations from COMSOL a minimum element quality (MEQ) of at least 0.1 was used whenever achievable.

### 3.6.2 Structure optimization

The volumetric flow difference between the outlets of the gradient generator was minimized by using the optimization module in COMSOL Multiphysics. The function used for optimization can be seen in equation 3.1.

$$\lim_{x \rightarrow 0} x = \sum (Q_i - Q_{i+1})^2 \quad (3.1)$$

Where  $Q_i$  is the volumetric flow rate at outlet  $i$ , and  $Q_{i+1}$  is the volumetric flow rate at the neighbouring outlet. The optimization variables were set to be the radii of the channels connecting the inlets to the mixing component. The radius variables were coupled to their mirrored counterparts to reduce optimization complexity. The optimization was done on a layer by layer basis, whereby only the radii of one layer was optimized at a time. The radii of the previous layer was kept constant, but the flow between the previous outlets were kept as optimization constraints to avoid alternative flow routes.

### 3.6.3 Droplet Generator Simulations

The droplet generator was simulated in COMSOL Multiphysics. The simulations are based on a polyvinyl alcohol (PVA) in water solution and grape seed oil, with a varying size scale of the channels. The user specified values used for the simulations are listed below.

Table 3.4: User specified values used for droplet generator simulations in COMSOL Multiphysics unless otherwise specified.

<b>Parameter</b>	<b>Value</b>
Contact Angle	$\pi$ rad
Density 8% PVA	$1023 \text{ kg/m}^3$
Density 14% PVA	$1039 \text{ kg/m}^3$
Density Grape Seed Oil [67]	$919 \text{ kg/m}^3$
Flow of Continuous Phase	$0.20 \text{ ml/min}$
Flow of Dispersed Phase	$0.05 \text{ ml/min}$
Interface Thickness	$5 \cdot 10^{-5} \text{ m}$
Reinitialization parameter	0.01 to 0.12 $\text{m/s}$
Interfacial Tension Grape Seed Oil	$24.0 \text{ mN/m}$
Scale	0.4 to 1
Slip Length	$5 \cdot 10^{-6} \text{ m}$
Viscosity 8% PVA	$9.0727 \text{ mPa} \cdot \text{s}$
Viscosity 14% PVA	$36.851 \text{ mPa} \cdot \text{s}$
Viscosity Grape Seed Oil [68]	$46.6 \text{ mPa} \cdot \text{s}$

The density and viscosity of the PVA solutions was estimated using Eq. 3.2 and Eq. 3.3. Both of these equations are based on fitted experimental data [69, 70].

$$\rho = 1.0020 + 0.2629 \cdot \omega \quad (3.2)$$

$$\mu = 0.0014 \cdot e^{0.2336 \cdot C} \quad (3.3)$$

In Eq. 3.2,  $\rho$  is the density [g/ml] and  $\omega$  is the PVA mass fraction [69]. The equation is temperature dependent and only works at 20 °C for the given coefficients. The concentration,  $C$ , in Eq. 3.3 is the concentration of PVA in wt% [70].

### 3.7 Worm Junction Experiments

The Worm Junctions (WJs) were tested by injecting a fluorescein solution into inlet 1 and water into inlet 2, both at a rate of 2 ml/min, using two Single Syringe Pump NE-1010 syringe pumps. Since only the relative absorption between the outlets were required for the experiment the fluorescein concentration was random but kept between an resulting absorbance of 0.1 and 0.8 to ensure linearity according to Lambert-Biers law. Any bubbles created during the fluid injection were removed to avoid changes in the flow profile. The setup was kept planar to avoid gravity induced unequal flow between the two outlets. Equal flow between the two outlets was estimated by collecting samples from both outlets simultaneously and comparing the volume. The sample collection was started after 30 seconds to ensure equilibrium of the system. The samples were collected in pairs, one from the outlet on the fluorescein solution side and one from outlet on the water side. The relative absorbance of fluorescein in the samples was measured at 474 nm using a UV-VIS spectrophotometer (UV-1800) (Shimadzu).

### 3.8 Gradient generator

The gradient generators were tested by injecting a fluorescein solution into inlet 1 and water into inlet 2, both at a rate of 1 ml/min, using two Single Syringe Pump NE-1010 syringe pumps. Since only the relative absorption between the outlets were required for the experiment the fluorescein concentration was random but kept between a resulting absorbance of 0.1 and 0.8 to ensure linearity.

The setup was kept planar to avoid gravity induced unequal flow between the outlets. Equal flow between the five outlets was estimated by collecting samples from all outlets simultaneously and comparing the volume. The sample collection was started after 30 seconds to ensure equilibrium of the system. The relative absorbance of fluorescein in the samples was measured at 474 nm using a UV-VIS spectrophotometer (UV-1800) (Shimadzu).

## 3.9 Droplet Generator

To test the droplet generator a solution of 8% PVA and 14% PVA in water together with a solution of grape seed oil and Nile red is used. The continuous phase flow was initiated first to wet the walls whereafter the dispersed phase was initiated such that both phases are flowing. This is done to avoid an inversion of the phases, which may happen if both flows are initiated simultaneously. The flow rate for the PVA solution is constant at 200  $\mu\text{L}/\text{min}$ , and the flow rate of grape seed oil is varied from 20  $\mu\text{L}/\text{min}$  to 120  $\mu\text{L}/\text{min}$ . The droplet generator is connected to a clear silicone tube for easy detection of droplets, see Figure 3.1. When a continuous generation of droplets is achieved a snapshot of the droplets is taken using a Steini 508 stereo microscope with an Axiocam 105 Color. ImageJ is then used for size determination of the droplets.

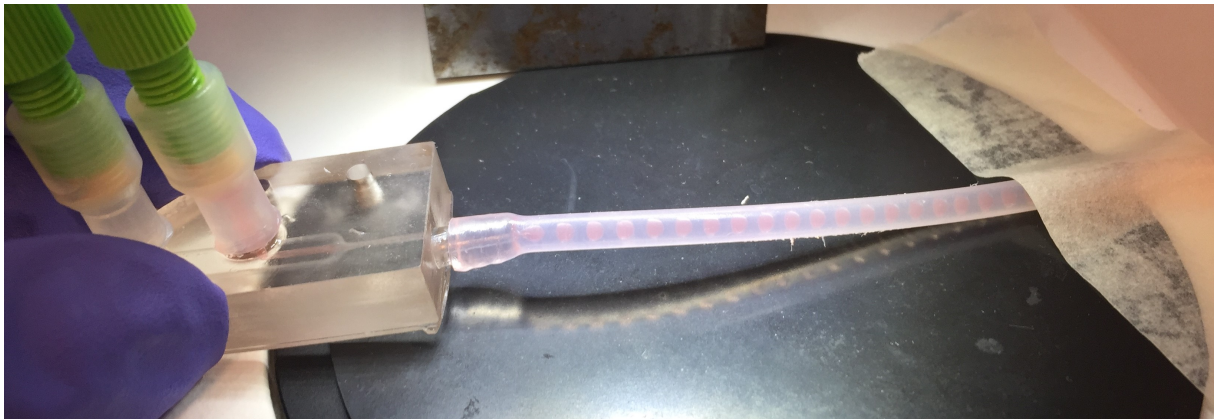


Figure 3.1: Image of the experimental setup used for testing the diameter of the droplets generated using the 3D printed droplet generator. No inclination of the tube was present during testing.

## 3.10 Electrospinning

Further testing of the droplet generator is done by using it in combination with electrospinning for continuous electrospinning of emulsions into fibers. The solutions used for electrospinning are solutions of 8% PVA, 10% PVA, and 14% PVA in water and a grape seed oil with Nile red solution. The solutions are injected with a ratio of 5:1 or 5:2, using 50  $\mu\text{L}/\text{min}$  PVA and 10  $\mu\text{L}/\text{min}$ , 20  $\mu\text{L}/\text{min}$  grape seed oil. The applied voltage is between 15 kV and 20 kV and is adjusted until stable spinning is observed. The droplet generator was incorporated into the system where it generates emulsions directly into the

PVA solution. The resulting fibers with emulsions are characterized using ImageJ via snapshots taken using an OLYMPUS IX71 inverted microscope.

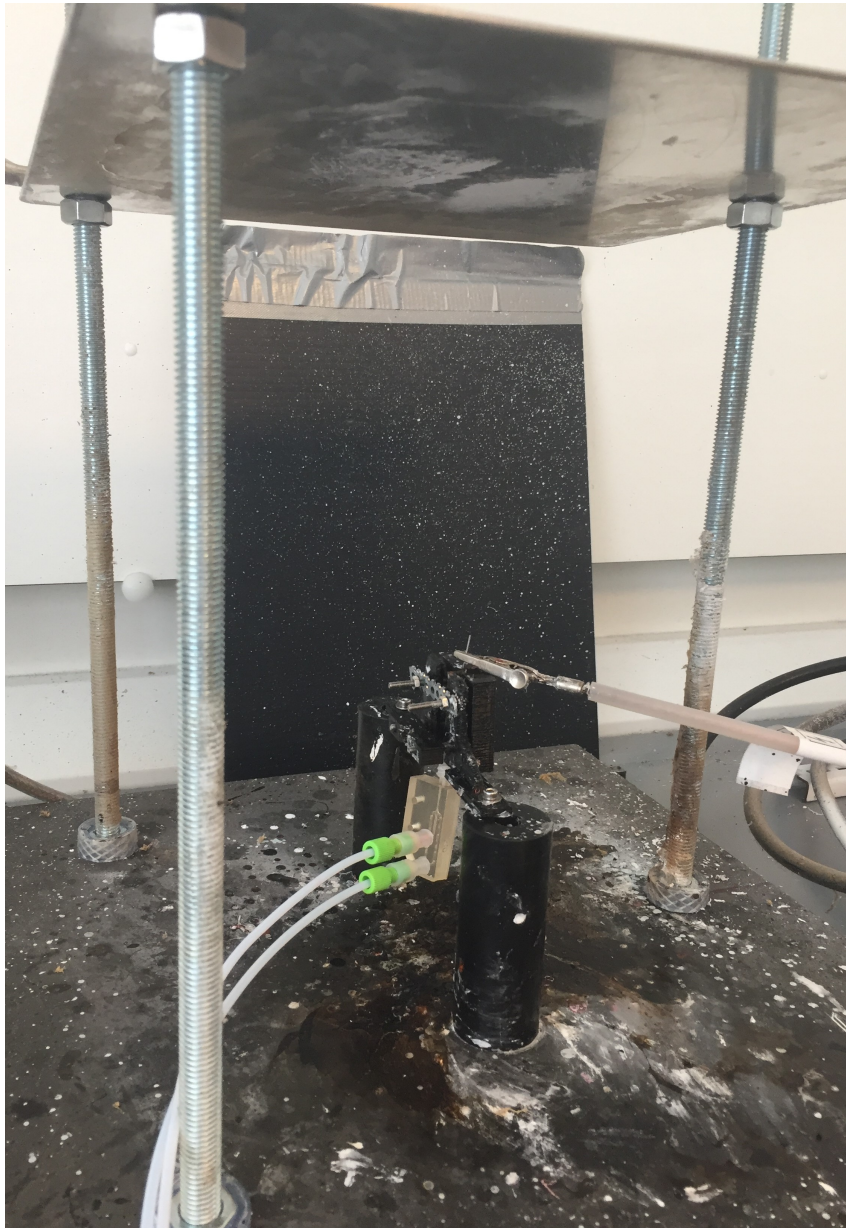


Figure 3.2: Image of the experimental setup used for electrospinning with the droplet generator connected directly to the spinneret.

### 3.11 Solvent Experiments

To test the corrosion- and solvent-resistance of the 3D prints a set of prints was submerged in acids and organic solvents. A piece made of the first eight layers, where each layer has been exposed to UV for 70 seconds, is immersed in approximately 20 mL of either an

acid or an organic solvent for 24-30 hours at room temperature. Afterwards the 3D print pieces are removed, dried using compressed nitrogen, and investigated using a Stemi 508 stereo microscope with an Axiocam 105 Color. The chemicals that have been tested are:

- 1-Butanol
- 1-Octadecene
- Acetic acid (10%, 20%, 30%, 40%)
- Acetone
- Acetonitrile
- Dichloromethane (DCM)
- Dimethylformamide (DMF)
- Ethanol
- Ethanolamine
- Ethylacetat
- Hydrochloric acid (HCl) (10%, 20%, 30%, 40%)
- Isopropanol
- Methylcyclohexane
- N-Methyl-2-pyrrolidone (NMP)
- Nitric acid (6.5%, 13%, 19.5%)
- Phosphoric acid (8.5%, 17%, 25.5%)
- Tetrachloroethylene
- Triethylamine

## 3.12 Leeching Experiment

To investigate the leeching of unknown residual compounds from the 3D prints into liquid medium an experiment measuring the absorption at different intervals is made. The absorption of the samples are measured using UV-VIS spectrophotometer (UV-1800) (Shimadzu) at 230 nm and a 10 mm Quartz Suprasil High Performance Cell. A set of 8 samples are prepared with a standardised (1 cm x 1 cm x 3 mm) 3D print that are submerged in 3 mL of Milli-Q water. One sample never have the water changed and functions as the baseline, 1 has the water changed every 6 hrs, and the other 6 samples are spilt up into pairs where the water is changed every 1 hr, 2 hrs, or 3 hrs. The samples are measured every hour after the first water change except for the baseline and "changed every 6 hours".

A leeching test was performed using the WJ. This was done by connecting a 20 mL syringe filled with Milli-Q water to the WJ and continuously injecting the water until the syringe is empty (within 5 min). The water is then collected and the absorption measured at 230 nm using a 10 mm Quartz Suprasil High Performance Cell and a UV-VIS spectrophotometer (UV-1800) (Shimadzu). The WJ is then submerged in Milli-Q water for one hour, whereafter the experiment is repeated.



---

## 4. Results and Discussion

---

### 4.1 Minimum Feature Size

The intent of the project is to use 3D printing to create microfluidic systems with the smallest dimensions possible with the Anycubic Photon 3D printer. Therefore, the achievable channel MFS was investigated by making a series of prints of a structure with square and circular channels with varying sizes from 0.1 mm to 1 mm, see Figure 4.1. The structures were printed with varying layer thicknesses, exposure times, and angles to the building platform, where 0 degrees is when the channels are perpendicular to the platform, to further test what the limitations are. An overview of the tested parameters, as described in Section 3.5, with the corresponding tables can be seen in Table 4.1.

Table 4.1: The different settings used to investigate the achievable MFS with their associated table.

Layer Thickness	Angle to Platform	Exposure Time	Design	Table
10 $\mu\text{m}$	0, 20, 45, 70, 90	6 s, 8 s	Square	4.2
			Circular	4.3
20 $\mu\text{m}$	0, 20, 45, 70, 90	6 s, 8 s	Square	4.4
			Circular	4.5
50 $\mu\text{m}$	0, 20, 45, 70, 90	6 s, 8 s	Square	4.6
			Circular	4.7

The results of each setting are presented in Table 4.2 to Table 4.7. The first number represents the height of the channel and the number below is the width of the channel. Each number is based on an average of at least two prints. The open channels are colored according to the error percentage where the most deviating number (height or width) is compared to the designed size. Grey is for closed channels, green (0-5% error), yellow (5-10% error), orange (10-20% error) and red (>20% error) are used for the open channels. Different symbols are also used,  $\emptyset$  shows that there are conflicting results, \* is if an indentation or a mark can be seen instead of a channel and \*\* if nothing can be seen where a channel should be. Settings marked with both \* and \*\* indicates that some prints had an indentation/mark and some had no indentation/mark.

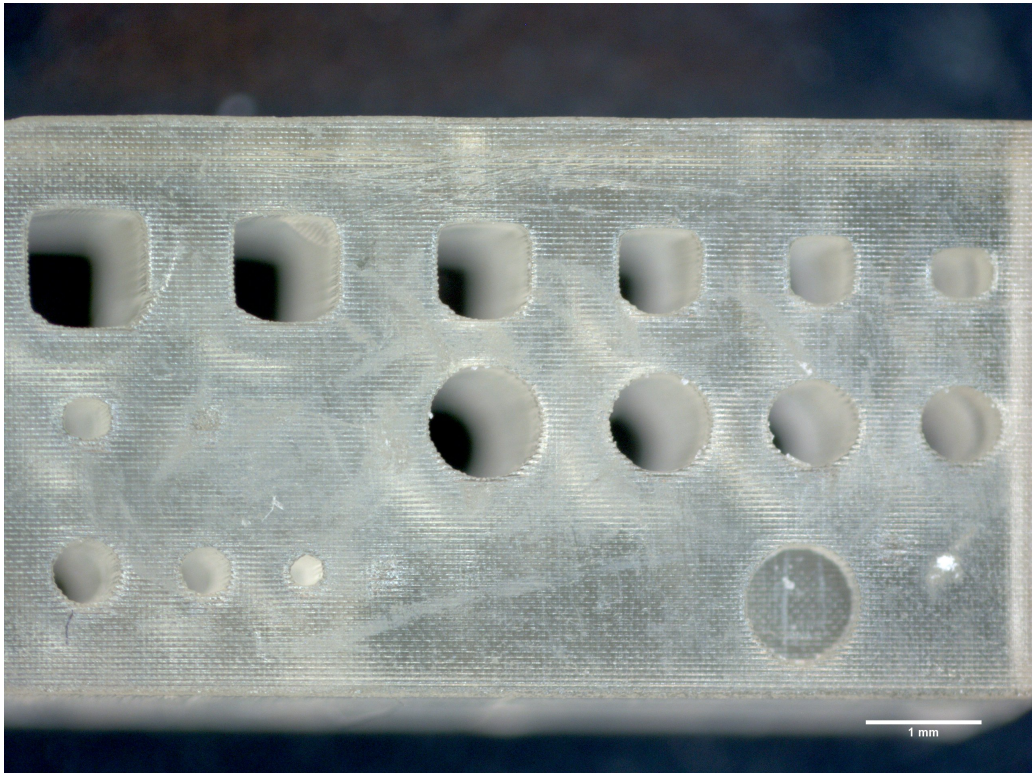


Figure 4.1: Snapshot taken under a microscope of the structure used for finding the minimum achievable feature size. The structure was printed with a  $10\ \mu\text{m}$  layer thickness at a  $0$  degree angle to the print direction with a 6 second layer exposure time.

Table 4.2: Results of printing square channels with 10  $\mu\text{m}$  layer thickness. The first number is the height, the second is the width and every color other than grey represents open channels with different error percentages. Green: <5% error, Yellow: 5-10% error, Orange: 10-20% error, Red: >20% error. \* small indentation/mark but no channel, \*\* no indentation/mark can be seen,  $\emptyset$  conflicting results.

Layer Thickness	$\Theta$ to platform	Exposure Time	1x1	0.9x0.9	0.8x0.8	0.7x0.7	0.6x0.6	0.5x0.5	0.4x0.4	0.3x0.3	0.2x0.2	0.1x0.1
10 $\mu\text{m}$	0	6 s	1.033	0.930	0.857	0.736	0.604	0.461	0.330	*	*/**	**
			1.059	0.948	0.839	0.714	0.584	0.526	0.399			
	0	8 s	0.970	0.862	0.787	0.670	0.545	0.432	0.295	*	*/**	**
			0.999	0.881	0.789	0.663	0.544	0.469	0.344			
	20	6 s	1.061	0.954	0.841	0.753	0.622	0.543	0.375	*	*/**	**
			1.096	0.994	0.886	0.742	0.656	0.592	0.447			
	20	8 s	1.031	0.929	0.807	0.709	0.586	0.493	0.337 $\emptyset$	*	*	*
			1.077	0.971	0.862	0.753	0.653	0.570	0.413			
	45	6 s	1.028	0.900	0.803	0.704	0.619	0.497	0.386 $\emptyset$	0.255	*	*
			1.040	0.908	0.805	0.692	0.604	0.518	0.423	0.328		
	45	8 s	0.999	0.884	0.763	0.671	0.563	0.466	0.351	*	*	*/**
			0.989	0.879	0.798	0.668	0.562	0.483	0.386			
	70	6 s	1.022	0.916	0.802	0.709	0.611	0.507	0.398	0.302	*	**
			1.167	1.017	0.905	0.817	0.712	0.607	0.509	0.402		
	70	8 s	1.002	0.898 $\emptyset$	0.764 $\emptyset$	0.676 $\emptyset$	0.566 $\emptyset$	0.478	0.362	*	*	*/**
			1.085	0.959	0.829	0.741	0.652	0.571	0.458			
	90	6 s	1.019	0.911	0.797	0.701	0.620	0.530	0.403	0.314	*	*
			1.157	1.034	0.948	0.837	0.744	0.678	0.568	0.455		
	90	8 s	1.032	0.929	0.832	0.730	0.620	0.522	0.424	0.317	*	*
			1.058	0.956	0.837	0.739	0.632	0.582	0.440	0.333		

Table 4.3: Results of printing circular channels with 10  $\mu\text{m}$  layer thickness. The first number is the height, the second is the width and every color other than grey represents open channels with different error percentages. Green: <5% error, Yellow: 5-10% error, Orange: 10-20% error, Red: >20% error. \* small indentation/mark but no channel, \*\* no indentation/mark can be seen,  $\emptyset$  conflicting results.

Layer Thickness	$\Theta$ to platform	Exposure Time	1x1	0.9x0.9	0.8x0.8	0.7x0.7	0.6x0.6	0.5x0.5	0.4x0.4	0.3x0.3	0.2x0.2	0.1x0.1
10 $\mu\text{m}$	0	6 s	0.979	0.860	0.730	0.653	0.601	0.426	0.283	*	*/**	**
			0.997	0.900	0.792	0.712	0.572	0.455	0.295	*	*/**	**
	0	8 s	0.928	0.818	0.684	0.602	0.501	0.355	*	*	*/**	**
			0.948	0.850	0.749	0.660	0.541	0.383	*	*	*/**	**
	20	6 s	1.056	0.945	0.841	0.749	0.555	0.472	0.298	*	*/**	**
			1.057	0.945	0.878	0.785	0.611	0.488	0.343	*	*/**	**
	20	8 s	1.011	0.916	0.794	0.689	0.510	0.381	*	*	*	*/**
			1.008	0.917	0.821	0.722	0.539	0.421	*	*	*	*/**
	45	6 s	1.003	0.883	0.790	0.667	0.597	0.430 $\emptyset$	0.360	*	*/**	*/**
			1.006	0.883	0.819	0.713	0.600	0.469	0.369	*	*/**	*/**
	45	8 s	0.958	0.850	0.763	0.650	0.551	0.404 $\emptyset$	0.334	*	*	*/**
			0.983	0.862	0.793	0.685	0.568	0.431	0.353	*	*	*/**
	70	6 s	1.002	0.896	0.790	0.705	0.542	0.466	0.351	0.226	*	**
			1.093	0.969	0.882	0.792	0.660	0.554	0.446	0.323	*	**
	70	8 s	0.930	0.838	0.758	0.662 $\emptyset$	0.551	0.466	0.315	*	*	*/**
			1.063	0.947	0.834	0.747	0.614	0.502	0.386	*	*	*/**
	90	6 s	0.990	0.873	0.767	0.673	0.601	0.509	0.395	0.298	*	*
			1.128	1.043	0.957	0.873	0.741	0.645	0.510	0.415	0.228	*
90	8 s	1.000	0.926	0.819	0.696	0.594	0.489	0.390	0.290	0.228	*	
		1.032	0.929	0.833	0.756	0.647	0.536	0.426	0.314	0.233	*	

Table 4.4: Results of printing square channels with 20  $\mu\text{m}$  layer thickness. The first number is the height, the second is the width and every color other than grey represents open channels with different error percentages. Green: <5% error, Yellow: 5-10% error, Orange: 10-20% error, Red: >20% error. \* small indentation/mark but no channel, \*\* no indentation/mark can be seen,  $\emptyset$  conflicting results.

Layer Thickness	$\Theta$ to platform	Exposure Time	1x1	0.9x0.9	0.8x0.8	0.7x0.7	0.6x0.6	0.5x0.5	0.4x0.4	0.3x0.3	0.2x0.2	0.1x0.1
20 $\mu\text{m}$	0	6 s	1.067 1.083	0.970 0.933	0.883 0.841	0.786 0.713	0.664 0.624	0.546 0.517	0.315 0.380	*	*	**
		8 s	0.995 1.017	0.907 0.873	0.809 0.784	0.701 0.657	0.578 0.563	0.477 0.450	0.281 $\emptyset$ 0.323	*/**	**	**
	20	6 s	1.082 1.105	0.989 0.998	0.873 0.895	0.781 0.748	0.632 0.649	0.527 0.558	0.402 0.447	*	*	**
		8 s	0.968 1.028	0.869 0.912	0.752 0.821	0.675 0.672	0.550 0.563	0.428 0.445	0.309 0.361	*	*	*/**
	45	6 s	1.032 1.050	0.915 0.940	0.832 0.851	0.737 0.723	0.650 0.645	0.525 0.532	0.390 0.418	*	*	*
		8 s	0.982 0.992	0.866 0.889	0.772 0.794	0.671 0.671	0.595 0.595	0.470 0.488	0.328 0.343	*	*	**
	70	6 s	1.049 1.107	0.944 0.986	0.823 0.855	0.709 0.769	0.622 0.666	0.524 $\emptyset$ 0.573	0.393 0.440	0.307 0.349	*/**	**
		8 s	1.043 1.033	0.909 0.924	0.797 0.807	0.717 0.711	0.554 $\emptyset$ 0.616	0.500 0.542	0.382 0.411	0.307 0.320	*	*
	90	6 s	1.063 1.130	0.942 1.007	0.855 0.877	0.730 0.794	0.645 0.665	0.541 0.634	0.422 0.460	0.321 0.341	*	*
		8 s	1.062 1.017	0.945 0.942	0.848 0.811	0.717 0.723	0.617 0.626	0.525 0.569	0.436 0.404	0.320 0.310	*	*

Table 4.5: Results of printing circular channels with 20  $\mu\text{m}$  layer thickness. The first number is the height, the second is the width and every color other than grey represents open channels with different error percentages. Green: <5% error, Yellow: 5-10% error, Orange: 10-20% error, Red: >20% error. \* small indentation/mark but no channel, \*\* no indentation/mark can be seen,  $\emptyset$  conflicting results.

Layer Thickness	$\Theta$ to platform	Exposure Time	1x1	0.9x0.9	0.8x0.8	0.7x0.7	0.6x0.6	0.5x0.5	0.4x0.4	0.3x0.3	0.2x0.2	0.1x0.1
20 $\mu\text{m}$	0	6 s	1.021	0.925	0.803	0.700	0.583	0.449	0.290	*	*/**	**
			1.017	0.925	0.827	0.740	0.559	0.454	0.298			
		8 s	0.958	0.852	0.743	0.635	0.514	0.374	*	*/**	**	**
			0.955	0.853	0.756	0.651	0.508	0.385				
	20	6 s	1.090	0.993	0.862	0.748	0.592	0.486	0.338	*	*	**
			1.067	0.972	0.855	0.749	0.625	0.502	0.363			
		8 s	0.961	0.866	0.767	0.630	0.534	0.394	*	*	*	**
			0.983	0.900	0.767	0.664	0.556	0.441				
	45	6 s	1.011	0.906	0.819	0.692	0.583	0.459	0.347	*	*	*/**
			1.020	0.908	0.815	0.721	0.612	0.494	0.373			
		8 s	0.950	0.856	0.760	0.640	0.558	0.415	0.321	*	*	**
			0.966	0.840	0.760	0.659	0.579	0.470	0.331			
	70	6 s	0.976	0.894	0.781	0.686	0.547	0.445	0.358	*	*	**
			1.059	0.970	0.861	0.795	0.631	0.521	0.433			
		8 s	0.969	0.895	0.790	0.679	0.536	0.431	0.329	*	*	*/**
			1.010	0.921	0.818	0.736	0.580	0.483	0.364			
	90	6 s	0.988	0.893	0.817	0.706	0.602	0.490	0.390	0.294	0.197	*
			1.094	0.982	0.874	0.819	0.708	0.592	0.468	0.364	0.263	
		8 s	0.984	0.885	0.807	0.684	0.582	0.469	0.387	0.289	*	**
			1.015	0.923	0.826	0.782	0.634	0.537	0.406	0.283		

Table 4.6: Results of printing square channels with 50  $\mu\text{m}$  layer thickness. The first number is the height, the second is the width and every color other than grey represents open channels with different error percentages. Green: <5% error, Yellow: 5-10% error, Orange: 10-20% error, Red: >20% error. \* small indentation/mark but no channel, \*\* no indentation/mark can be seen,  $\emptyset$  conflicting results.

Layer Thickness	$\Theta$ to platform	Exposure Time	1x1	0.9x0.9	0.8x0.8	0.7x0.7	0.6x0.6	0.5x0.5	0.4x0.4	0.3x0.3	0.2x0.2	0.1x0.1
50 $\mu\text{m}$	0	6 s	1.050	0.912	0.847	0.752	0.592	0.596	0.378 $\emptyset$	*	*/**	**
			1.085	0.827	0.774	0.711	0.581	0.617	0.367	*	**	**
	8 s	1.019	0.851	0.783	0.682	0.524	0.502	0.199	*	**	**	
		1.043	0.823	0.741	0.667	0.538	0.526	0.233	*	**	**	
	20	6 s	1.101	0.983	0.918	0.776	0.660	0.508	0.319	*	*	**
			1.097	0.939	0.840	0.740	0.652	0.528	0.369	*	*	**
	8 s	0.995	0.909	0.789	0.707	0.560	0.466	0.297	*	**	**	
		1.067	0.917	0.816	0.712	0.598	0.506	0.298	*	**	**	
	45	6 s	1.049	0.940	0.846	0.744	0.655	0.533	0.398	*	*	**
			1.034	0.918	0.835	0.718	0.635	0.533	0.422	*	*	**
	8 s	1.005	0.900	0.805	0.701	0.624	0.508	0.404	*	*	*/**	
		1.024	0.906	0.816	0.715	0.624	0.511	0.336	*	*	**	
	70	6 s	1.020	0.927	0.802	0.710	0.591	0.521	0.382	0.289	*	**
			1.058	0.949	0.836	0.680	0.576	0.508	0.405	0.286	*	**
	8 s	1.014	0.909	0.808	0.711	0.594	0.501	0.414	*	*	**	
		1.016	0.893	0.791	0.663	0.564	0.495	0.421	0.308	*	*	
	90	6 s	1.002	0.915	0.819	0.714	0.612	0.529	0.414	0.313	*	*
			1.050	0.921	0.835	0.746	0.665	0.597	0.416	0.338	*	*/**
8 s	1.037	0.935	0.809	0.729	0.615	0.523	0.438	0.284	*	**		
	1.047	0.943	0.822	0.754	0.618	0.519	0.426	0.284	*	**		

Table 4.7: Results of printing circular channels with 50  $\mu\text{m}$  layer thickness. The first number is the height, the second is the width and every color other than grey represents open channels with different error percentages. Green: <5% error, Yellow: 5-10% error, Orange: 10-20% error, Red: >20% error. \* small indentation/mark but no channel, \*\* no indentation/mark can be seen,  $\emptyset$  conflicting results.

Layer Thickness	$\Theta$ to platform	Exposure Time	1x1	0.9x0.9	0.8x0.8	0.7x0.7	0.6x0.6	0.5x0.5	0.4x0.4	0.3x0.3	0.2x0.2	0.1x0.1	
50 $\mu\text{m}$	0	6 s	1.004 0.974	0.869 0.877	0.756 0.724	0.739 0.830	0.557 $\emptyset$ 0.563	0.375 $\emptyset$ 0.368	*	*	**	**	
		8 s	0.925 0.937	0.822 0.853	0.680 0.680	0.679 0.707	0.439 0.468	0.325 0.347	*	*	**	**	
	20	6 s	0.972 0.991	0.896 0.902	0.773 0.785	0.714 0.698	0.552 0.583	0.461 0.488	0.279 $\emptyset$ 0.304	*	*	**	**
		8 s	0.985 0.983	0.892 0.887	0.762 0.757	0.656 0.658	0.483 0.532	0.383 0.430	*	*	**	**	
	45	6 s	1.033 1.014	0.916 0.898	0.831 0.805	0.709 0.714	0.609 0.613	0.502 0.508	0.372 0.391	*	*/**	**	**
		8 s	1.008 0.999	0.906 0.908	0.807 0.805	0.693 0.690	0.566 0.532	0.437 0.407	0.324 0.312	*	*/**	**	**
	70	6 s	1.003 1.024	0.902 0.938	0.810 0.815	0.693 0.711	0.595 0.614	0.481 0.490	0.379 0.397	*	*	**	**
		8 s	0.993 1.007	0.891 0.922	0.770 0.799	0.690 0.703	0.598 0.606	0.466 0.482	0.339 0.357	*	*/**	**	**
	90	6 s	1.011 1.070	0.916 0.948	0.819 0.849	0.731 0.739	0.442 0.645	0.439 0.521	0.390 0.439	0.291 0.313	*	*	**
		8 s	1.034 1.036	0.941 0.963	0.844 0.846	0.734 0.738	0.610 0.607	0.518 0.518	0.413 0.406	*	*	**	**

The smallest open channel size that could be successfully printed is 0.4x0.4 mm, however this size does have limited success as well as conflicting results whereas the 0.5x0.5 mm size is more consistent. It is also possible to have 0.3x0.3 mm and 0.2x0.2 mm channels, but they would appear infrequently as a partial indentation/mark and are closed. These tendencies are contradictory to what is expected because the theoretical limit for the MFS should theoretically be the resolution of the light source, which is an LCD screen with a 2560x1440 resolution and a XY DPI of 47  $\mu\text{m}$ . However, due to scattering of UV light within the solution, light penetrating into previous layers, and the viscosity of the resin the possibility of reaching the theoretical limit becomes less feasible. Scattering of light within the solution spreads UV to parts that should not be cured, which is a problem that becomes increasingly more prominent the smaller the channels become, since the spreading distance is constant. Likewise, light penetrating into already cured layers causes unwanted curing because of the high viscosity of the resin. The high viscosity causes uncured parts, like channels, in previous layers to remain filled with resin since they do not empty out fast enough during the short downtime between each layer. The scattering and penetration of light between layers is reduced by the photoabsorbers added to resins, but the effectiveness varies from resin to resin.

It seems that the square channels are a better design than the circular channels since a total of 52, 53 and 63 channels, at 10  $\mu\text{m}$ , 20  $\mu\text{m}$ , and 50  $\mu\text{m}$ , are open with the square design, whereas only 47, 45, 56, at 10  $\mu\text{m}$ , 20  $\mu\text{m}$ , and 50  $\mu\text{m}$  are open with the circular design. This is contradictory to theory, seen from a cleaning perspective, since it requires less pressure to clean a circular channel than a square channel, as demonstrated in Appendix A. A possible explanation for why circular channels are harder to print lies in the geometry of the circle. While a square has a constant MFS equal to its side length, a circle goes from a MFS of 0 to its diameter. Thus, the parts of the circle with features smaller than the MFS will likely be overexposed resulting in an closed or oval shaped channel.

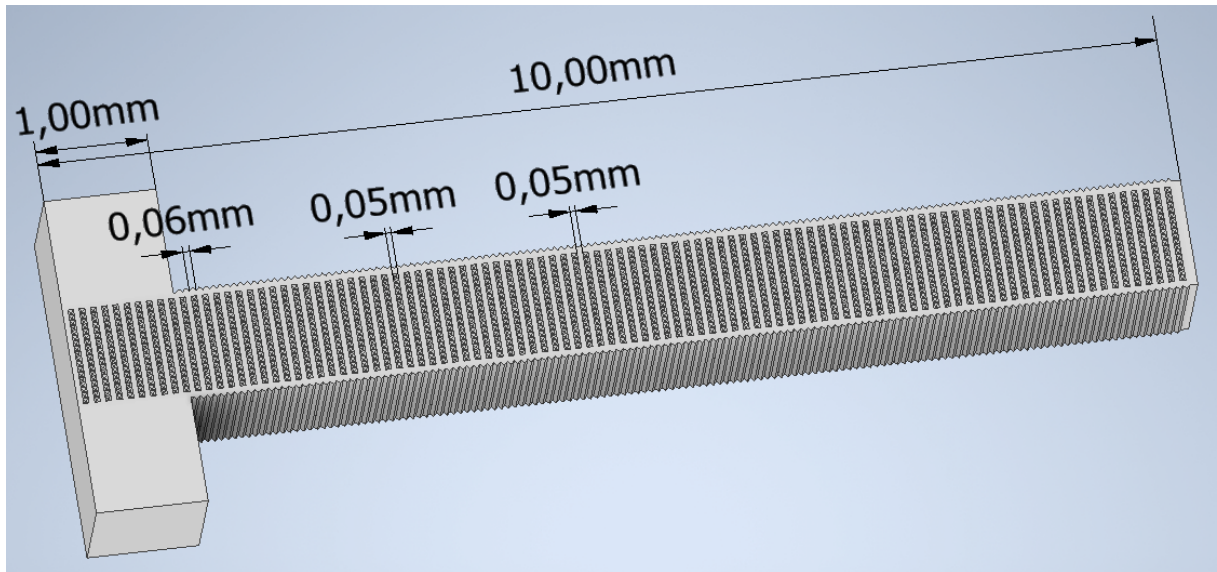
An exposure time of 8 seconds seems to cause overexposure of smaller channels, sealing them, whereas 6 seconds exposure causes the smaller channel sizes to remain open. Increasing the layer thickness enables printing open channels at an angle of 90 degrees (channels that are parallel to the platform). Smaller layer thicknesses with the same

angle have closed channels. Despite the layer thickness and exposure time the angle that yields the best channel sizes is 45 degrees since the number of open channels and the error percentage tends to be the highest and lowest, respectively. One thing to take note of, when comparing the error percentage and the shape of the channels, is the warping of the channels. This warping becomes more apparent for smaller channels, where square channels will have a side that bends instead of being straight, and circular channels will become oval. The change to the channels is visible in Figure 4.1 and is present in every MFS print.

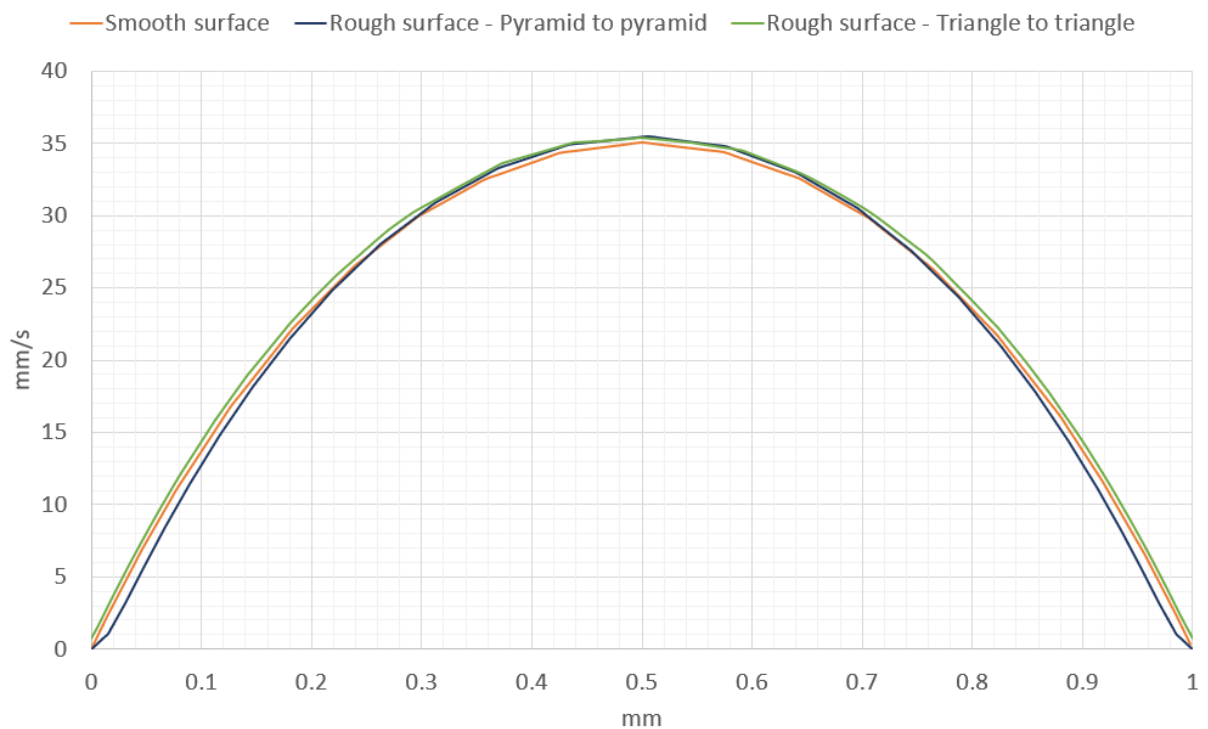
All the prints made to investigate the MFS are printed with clear resin from PrimaCreator, and if a different resin is used it might not yield the same values or tendencies presented here. Even if the resin is made to be used with a 405 nm light source, the chemical composition and concentrations can differ, thereby changing the optimal settings and achievable sizes that are possible to print.

## 4.2 Surface Roughness Effect on Flow

The surface of 3D prints has microscopic surface roughness, see Figure 4.1. To investigate the effect the surface roughness has on the flow through a channel and to investigate if the assumption of a smooth surface in simulations of 3D printed microfluidic systems is reasonable, simulations with and without surface roughness were made. The surface roughness was simulated using rows of small pyramidal structures on two sides pointing into the channel and crosschannel triangular structures on the remaining two sides. The dimensions of the surface roughness are based on measurements from Figure 4.1. The pyramids were 50  $\mu\text{m}$  wide/long and 20  $\mu\text{m}$  tall, while the crosschannel triangular structures were 30  $\mu\text{m}$  tall and 60  $\mu\text{m}$  wide. A space of 50  $\mu\text{m}$  between each row of pyramids were required as the program would otherwise crash. Fluorescein diffusion across the channel was simulated to calculate the influence of surface roughness on mixing of diluted species through a channel. The diffusion was simulated for 90 seconds using  $D_c = 4.25 \cdot 10^{-6} \frac{\text{cm}^2}{\text{s}}$ ,  $V_{total} = 4 \frac{\text{mL}}{\text{min}}$ ,  $C = 1 \frac{\text{mmol}}{\text{mL}}$ , and 31353585 meshing elements with a MEQ of 0.01. The simulation error was 1.55% for the rough surface version, and 0.34% for the smooth surface version. The simulated channel with surface roughness can be seen in Figure 4.2(a) and the flow profiles from both simulations can be seen in Figure 4.2(b).



(a)



(b)

Figure 4.2: (a): Channel with surface roughness used for simulating the effect the rough surface has on diffusion of diluted species through the channel. (b): Cross section channel flow profile from simulations with and without the observed surface roughness found on 3D printed structures.

A small difference can be observed between the flow profiles, see Figure 4.2. The flow profile for the channel with a rough surface (evaluated from pyramid to pyramid) has an increased velocity in the center of the channel, and a decreased velocity when approaching

the walls indicating flow stagnation. The stagnation layer is approximately 0.015 mm on both sides which is 1.5% of the total channel width. The maximum velocity was 35.04 mm/s for a smooth channel and 35.51 mm/s for a rough channel, which is an 1.34% increase in velocity. The flow profile evaluated from triangle to triangle follows the flow profile of a smooth surface.

The diffusion of fluorescein into the water stream was simulated to investigate if the added surface roughness caused mixing through minor disturbances in the flow. The rough surface caused an 8.6% reduction in concentration in the water phase, which is possibly explained by the focusing of the flow towards the middle of the channel reducing the residence time in the channel and thus the diffusion time. While the difference in stagnation, velocity, and concentration between the two simulations is measurable, the trade off between accuracy and simulation time must be evaluated. The simulations made for this report have an estimated error between 0.1% and 3.5%, which is within the same velocity error range caused by not taken surface roughness into account. The concentration error is larger than this range, but due to the requirements of simulating a rough surface, this must be accepted. The relatively small structure used for this simulation required  $\approx 85$  GB of RAM, and took 7 times more time to simulate compared to a smooth surface making it unrealistic upscaling it to the structure sizes used for future simulations. Thus, the gain in simulation accuracy is too small to justify the large increase in computational power and time required to achieve it. Additionally, the large requirement of meshing units to fully mesh the surface reduces the number of available meshing units for simulating diffusion. Simulating diffusion requires a well defined mesh since diffusion is dependent upon the concentration gradient of the diffusing compound. A rough mesh overestimates the diffusion length per time step resulting in more diffusion than expected. To put it into perspective a smooth surface version of the channel with a well defined mesh that more accurately depicts the concentration gradient has a concentration of 4.23% in the water stream, see Figure 4.2(a). A simulation with the same settings but with a rougher mesh has a concentration of 13.24% in the water stream. So while accounting for a rough surface is a more accurate representation of reality it comes at a cost in mesh resolution and thus the accuracy of the results.

## 4.3 Surface Treatment and Coating

Transparency of microfluidic systems is a vital feature for detecting flow issues such as clogs or bubbles. However, due to the inherent surface roughness of 3D printed objects even structures printed using clear resin are only partially transparent. To increase the transparency of the 3D printed microfluidic systems, a series of coating materials and surface treatments were tested to find the best mix between transparency, ease of application, and longevity, see Figure 4.3. The coatings were applied after the prints were cleaned and fully polymerized as described in Section 3.4.

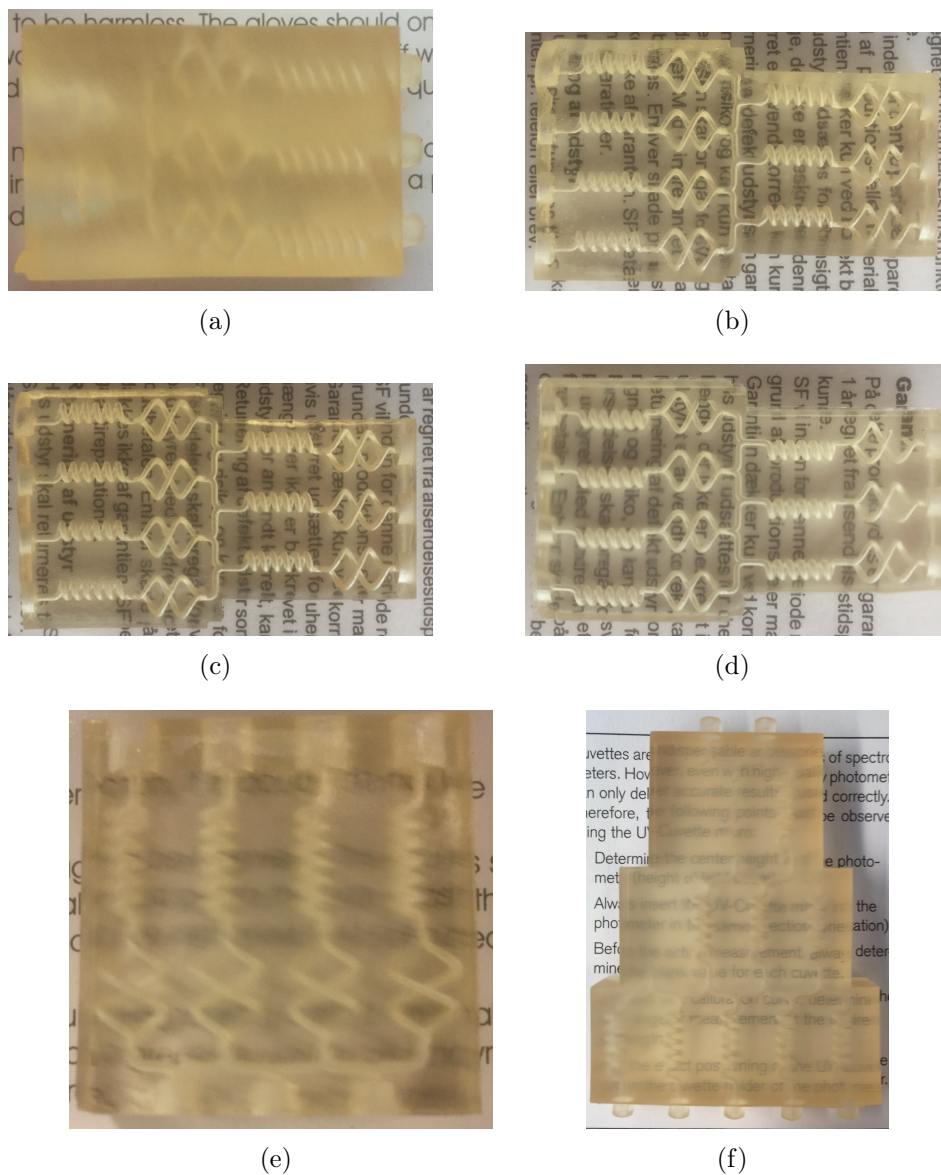


Figure 4.3: Results of coating/surface treating prints to achieve better transparency. (a): No coating, (b): nail polish, (c): clear resin, (d): clear tape, (e): hairspray, (f): polished with 10  $\mu\text{m}$  grain sand paper.

Figure 4.3 shows the effect of coating 3D printed structures with nail polish (b), clear resin (c), clear tape (d), hairspray (e), or polishing (f) has on the transparency of the structure. Coating with nail polish, clear resin, or clear tape gives a transparent print showing the inner channel geometry clearly, but coating with hairspray or polishing only gives a marginal increase in transparency, when compared to a non-coated print. The highest transparency is achieved using clear resin, clear tape, or nail polish, but each have their disadvantage. Clear resin requires further UV treatment, and may feel sticky even after prolonged UV exposure. Applying clear resin evenly over the surface is required to limit scattering of light, which may be difficult due to the high viscosity of resin. Clear tape achieves the smoothest surface, but also requires the largest amount of work to apply. The tape must be applied perfectly to avoid bubbles or creases, and requires cutting of excess tape. The highest transparency is achieved with polishing of the surface before applying clear tape. Water or glue-dissolving substances will easily damage the tape causing it to partly or completely fall off. Nail polish requires the least amount of work of the three to apply, but the transparency, like clear resin, depends on how well the nail polish is distributed on the surface. Nail polish is less viscous than resin making it easier to apply with a small brush, and dries quickly making it a preferable option to clear resin. The disadvantage is that it dissolves easily in acetone and is damaged by ethanol, so the structure cannot be cleaned with acetone without accidentally also damaging the coating. Hairspray and polishing the surface does not achieve the same level of transparency as the rest. Hairspray has the advantage of being the easiest to apply, but can easily be removed again with water making it unfavourable to use for microfluidic systems, as water can spill onto the outer surface during cleaning or from possible leaks. Polishing the surface is the most stable of the surface treatments, but requires quite a lot of work for only a marginal increase in transparency. The polishing treatment can be limited to key points of the structure to reduce the work required, but the structure must be made with polishing in mind, as reaching and polishing these points can become difficult. Given the advantages and disadvantages of each method of surface treatment/coating, nail polish was used for its ease of use and stability in water.

## 4.4 Solvent Experiments

The corrosion resistance and solvent resistance of the resin used for 3D printed microfluidic systems limits their possible applications since acids and organic solvents can cause erosion or degradation of the structure. The corrosion resistance and solvent resistance of the 3D printed microfluidic systems was tested with an experiment using acids and organic solvents according to the method described in Section 3.11. The chemicals used and the resulting effect are shown in Table 4.8.

Table 4.8: Effect of some acids and organic solvents on structures 3D printed from PrimaCreator Value DLP Clear Resin. The results are after 24-30 hours of chemical exposure. — indicates no visual damage to the structure.

Chemical	Damage/effect
1-Butanol	—
1-Octadecene	—
Acetic acid (10%, 20%, 30%, 40%)	—
Acetone	Minor surface etching
Acetonitrile	Bending, cracks
DCM	Partially dissolved
DMF	—
Ethanol	—
Ethanolamine	—
Ethylacetat	Cracks
HCl (10%, 20%, 30%, 40%)	—
Isopropanol	—
Methylcyclohexane	—
NMP	—
Nitric acid (6.5%, 13%, 19.5%)	Etching
Phosphoric acid (8.5%, 17%, 25.5%)	Etching
Tetrachloroethylene	—
Triethylamine	—

The chemicals that damage the prints and should not be used in a 3D printed microfluidic system are acetone, acetonitrile, DCM, ethylacetat, nitric acid and phosphoric acid. As specified in Table 4.8 acetone, nitric acid and phosphoric acid causes etching of the surface, DCM causes the part to partially dissolve, and acetonitrile and ethylacetat causes structural deformation of the print. All other tested chemicals did not show any effect on the 3D prints. It should be noted that prolonged exposure to acetic acid did not

cause structural damage but instead removed the discoloration a print would have after extended exposure to light. This was only on the outer surface and partially into the print. The pictures showing the effect are in Appendix B.

## 4.5 Leaching Experiments

Leaching of residual compounds from 3D prints into liquids they come into contact with is an issue that has been addressed in literature [33, 36, 71]. To test if the 3D prints leach residual compounds, an experiment based on the absorption spectrum of leached compounds was made. Leaching/release profiles of the chemicals were made by using standardized prints (1cm x 1cm x 3 mm) that were submerged in water for either 1 hr, 2 hrs, 3 hrs, or 6 hrs before the water was changed, as described in Section 3.12. The absorption of each water sample was measured every hour after the first water change. An absorption spectrum from the leaching experiment after 3 hrs is presented in Figure 4.4.

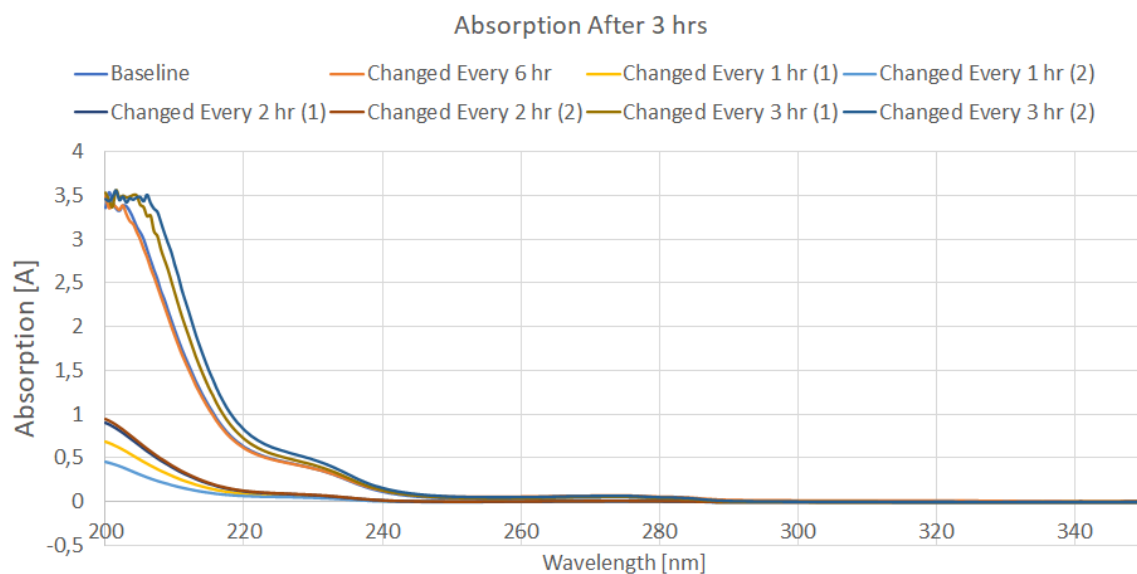
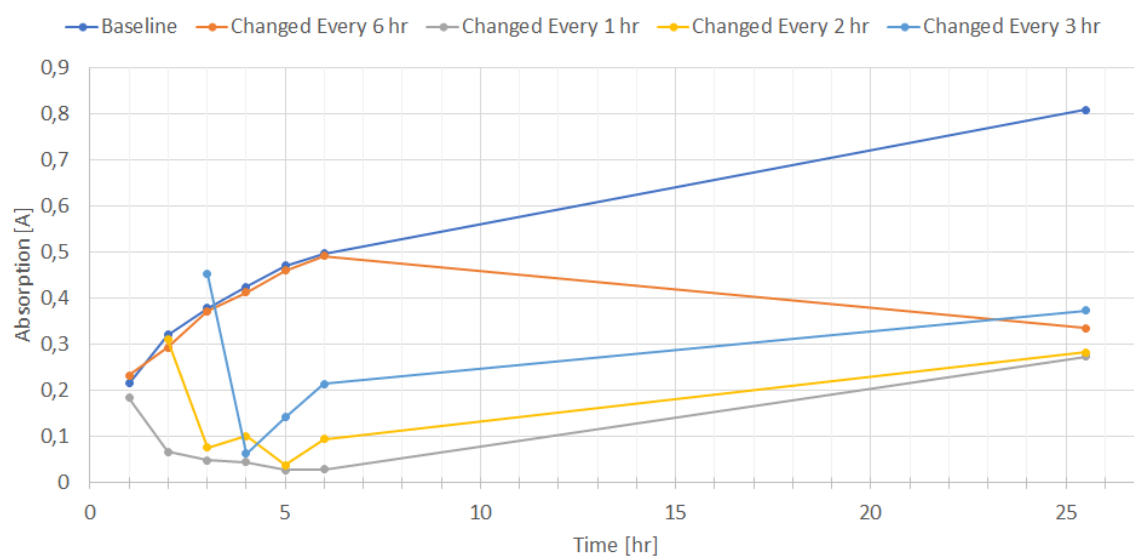


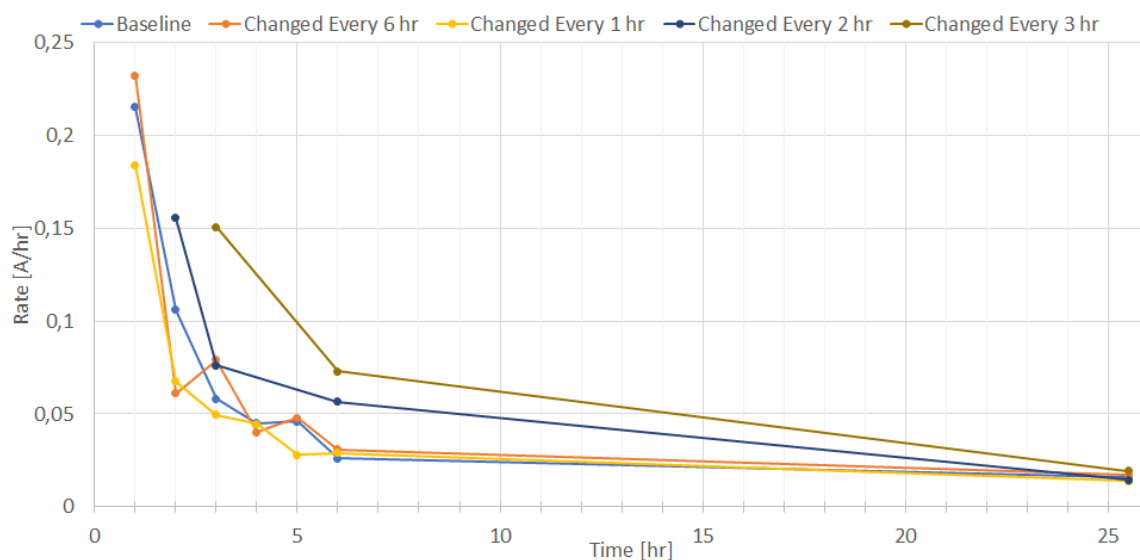
Figure 4.4: Absorption spectrum of leached unknown residual compounds from print into water from freshly printed and cleaned 3D prints (1 cm x 1 cm x 3 mm) after 3 hrs.

An absorption peak is observed at around 230 nm and an increase in absorption occurs in the 200 nm to 220 nm range. What exactly leached from the 3D print is unknown and further testing of the compound(s) is required to determine the malignancy of the compounds. Based on the cytotoxicity of the compounds used in 3D printing resins, the leached compounds are likely toxic [33, 36, 71].

The absorption at 230 nm was plotted over time to determine the leaching/release profiles of the unknown compounds from the 3D prints. The leaching/release profiles are shown in Figure 4.5(a) using the average absorption at 230 nm for each sample. To further highlight the effect of changing the water at different intervals, the rate of change in absorbance over time is plotted, see Figure 4.5(b).



(a)



(b)

Figure 4.5: (a): Leaching/release profile of unknown residual compounds into water from freshly printed and cleaned 3D prints (1cm x 1cm x 3 mm). The absorption is an average for each sample and is measured at 230 nm. The first point is measured at the first change of water and any subsequent water changes are timed according to the sample name. Every drop in absorption is caused by changing the water from the previous measurement. (b): Leaching rate of unknown residual compounds based on (a).

Figure 4.5(a) shows the leaching/release profiles of unknown residual compounds from standardised (1cm x 1cm x 3 mm) 3D prints into water. Every drop in absorption is caused by changing the water from the previous measurement. After the first water change the absorption drops to between 0.06 and 0.07, whereafter the samples, 'changed every 2 hr' and 'changed every 3 hr', have an increase to approximately 0.10 and 0.14, respectively. This indicates that there is still something left within the print that leaches since there is an increase in absorption after the water change for samples changed every 2 hr and every 3 hrs. The same can be said for 'changed every 1 hr', since there continues to be measurable absorption, however after each water change there is a slight decrease in the absorption value. It goes to show that waiting 1 hr, 2 hrs, or 3 hrs does not have large impact on the release of compounds within the first water change since all are in the same range of absorption (0.06 - 0.07).

At the 6 hr mark the water is exchanged for all samples, except for the baseline, and then measured the following day. During this time the samples continue to leach and at approximately 25 hrs the absorption is within a range of 0.27 to 0.38 even though the samples have different intervals at which the water is changed.

Figure 4.5(b) shows that all samples have the highest leaching rate at the first measurement which then decreases as a negative power function over time to a final rate of  $\approx \frac{0.016}{hr}$  at 25 hrs. The trend most likely stems from the concentration difference approaching equilibrium, where at the beginning the unknown compounds can leach into water easily due to the concentration difference that over time decreases as the system approaches equilibrium. Another point that could cause the rate to decrease over time could be that the compounds at the surface can more easily leach into the water compared to the compounds at the core of the print.

As mentioned previously changing the water does have a positive effect concerning the release of unknown compounds from the print, however in Figure 4.5(b) after 25 hrs there are almost no change in the rate of release for all samples. This indicates that over an extended period of time the release rates will become close to equal ( $0.014 \frac{1}{hr}$  -  $0.019 \frac{1}{hr}$ ) as the system approaches equilibrium.

Another leaching experiment was performed by rinsing the channels of the WJ with water,

a design that will be discussed later, and then measuring the absorption of the water, as described in Section 3.12. This was done to investigate the release of residual compounds, within a limited time period when using the WJ for experimentation.

The water injected through the WJ has an average absorption of  $0.190 \pm 28$  at 230 nm. Submerging the WJ in water for an hour and then repeating the experiment reduced the leaching to  $0.085 \pm 0.002$ . This shows that after having been submerged in water, the release of unknown compounds has decreased which was to be expected since the previous experiment has an almost identical setup with the same result. However, the WJ leaching test highlights how the difference in size, surface area and geometry of the prints are all important factors since the tested WJ (shown in Figure 4.8(f)) is vastly different compared to the standardised 1 cm x 1 cm x 3 mm print. This is evident by the time difference between when the samples are first measured in the experiments. For the samples in Figure 4.5(a) the absorption is  $\approx 0.2$  after 1 hr, whereas the leaching from the WJ samples has an average of  $0.190 \pm 28$  within 5 minutes. Other contributors to this difference can also originate from how thoroughly the prints have been cleaned and how long they have been cured in UV.

Based on the leaching experiments some method is necessary to effectively remove the unknown compounds from the print, since a normal wash only seems to be effective in the beginning. Sonication of the structure in water before usage, as proposed by Ngan *et al.*, may be the solution as they by using sonication had success in lowering the toxicity of their prints [71].

## 4.6 Worm Junction - Chemotaxis

The WJ microfluidic system has been designed using Autodesk Inventor for the use in chemotaxis experiments with *C. elegans*. The basic design relies on introducing the species to a compound through a steep concentration gradient in a narrow channel, see Figure 4.6. This steep gradient will be generated through two inlets; one with the compound and one with water. The two streams will move in parallel with as little mixing as possible to limit false negatives, as these may occur through diffusion of the compound into the water stream. If the nematode finds the compound favourable they should swim into the compound stream and exit through the compound outlet. If not, they will exit through the water outlet together with the water stream. Thus, nematodes can be continuously injected into the WJ and be sorted depending on their chemotaxis.

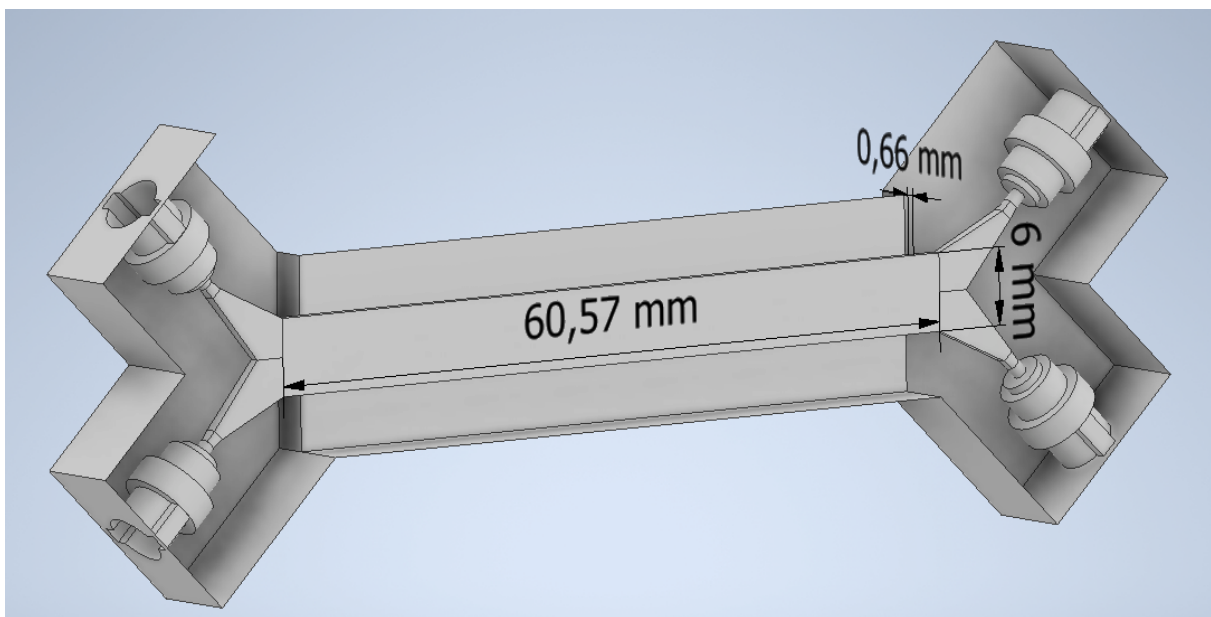


Figure 4.6: Image of WJ microfluidic system drawn in Autodesk Inventor.

One of the key parameters in the design of the WJ is the diffusion coefficient of the compound. It is expected that a higher diffusion coefficient will cause more compound to diffuse into the water stream. Likewise, as diffusion is dependent upon time, a lower flow rate will result in more diffusion, as it takes more time for the water to exit the channel. Therefore, a balance between flow rate, channel width, and channel length for a given nematode swim speed and compound diffusion coefficient must be found that results in

as little compound in the water stream while retaining enough time for the nematode to explore the concentration gradient. The height of the channel is thought to be irrelevant in this balance, as an increase in height will both increase the interface area between the two flows leading to more diffusion, but will also increase the volume of the channels, thus canceling out the increase in concentration through an increase in volume. The only requirement is that the channel is high enough for *C. elegans*, which has an approximate length of 1 mm and a width of 50  $\mu\text{m}$  - 60  $\mu\text{m}$ . The width of the channel was chosen to be 6 mm as this would give 1 mm distance from the wall and 1 mm to the compound/water interface, if the nematode was situated perpendicular to the flow. The 60 mm channel length was chosen as an estimate on the required channel length based on giving the nematode enough time in the channel.

The swimming speed of the nematodes is essential, as they should be able to cross into the compound stream before being ejected from the microfluidic system. The movement of *C. elegans* was studied by Tsechpenakis et al., and they measured a swimming speed of 2.4 mm/s with infrequent short breaks. Since the WJ is 6 mm wide, it would take a *C. elegans* 2.5 seconds to traverse the WJ. This sets the upper flow speed limit at 24 mm/s for the 60 mm long channel, which corresponds to 5.7 ml/min given that the cross sectional area of the channel is 3.96 mm<sup>2</sup>. The experiments presented in Section 4.6.3 were conducted with a flow rate of 4 ml/min, which is too close to the maximum flow rate, as it would only enable *C. elegans* to cross into the compound stream without enough time to return to the water stream if it deems the compound unfavourable. The simulations were updated to match the flow rate used in the experiments to enable comparison between simulated and experimental results.

#### 4.6.1 Simulations of Worm Junction - Chemotaxis

The WJ was simulated using the finite element analysis program COMSOL Multiphysics to simulate if the dimensions and flow rates discussed in the previous section are optimal. The intent of the simulation is to simulate the diffusion of the compound in the WJ.

The simulation of transport of diluted species through the WJ was simulated for 90 seconds using  $D_c = 4.25 \cdot 10^{-6} \frac{\text{cm}^2}{\text{s}}$ ,  $Q_{total} = 4 \frac{\text{mL}}{\text{min}}$ ,  $C = 1 \frac{\text{mmol}}{\text{mL}}$ , and 816272 meshing elements with a MEQ of 0.1322. The results of the simulation can be seen in Figure 4.7.

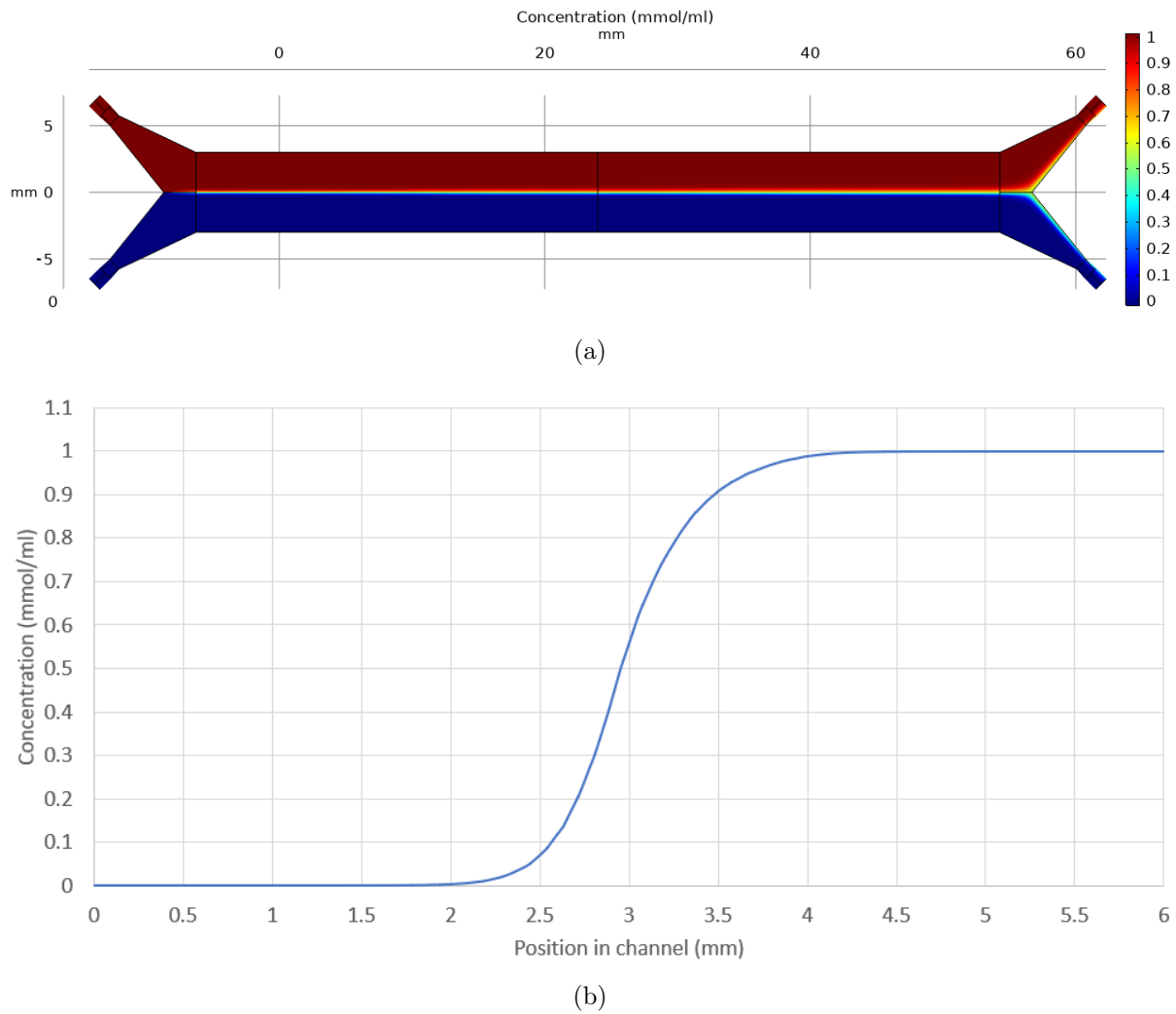


Figure 4.7: (a): Diffusion across the WJ simulated for 90 seconds using  $D_c = 4.25 \cdot 10^{-6} \frac{cm^2}{s}$ ,  $Q_{total} = 4 \frac{mL}{min}$ ,  $C = 1 \frac{mmol}{mL}$ , and 816272 meshing elements with a MEQ of 0.1322. The calculated simulation error was 1.804% and the fluorescein concentration at the water stream outlet was 4.33%. (b): Concentration profile evaluated across the WJ at the point 2 mm before the channel splits.

Figure 4.7(a) shows the result of the simulation of transport of diluted species. The error of 1.804% was estimated by evaluating the volumetric flow at the inlets and at the middle of the structure. The simulation shows that the further down the channel the water travels, the more of the diluted species diffuses into the water stream. For the values stated above, the relative fluorescein concentration at the water stream outlet is 4.33% and 95.67% in the fluorescein stream outlet. The concentration is evaluated as the average over the surface of the outlet, but the majority of the compound is situated close to the compound/water interface between the two streams. The diluted species diffused 1.04 mm into the water stream making the compound/water interface 2.08 mm

wide, see Figure 4.7(b). The compound/water interface is wide enough for *C. elegans* to swim in thus making it possible to give a false positive/negative depending on the preferred concentration, yet it may not be possible to correct this issue. Possible mixing from introducing living moving organisms into the stream is not accounted for making the compound/water interface possibly wider than what is shown here.

In the previous simulation the diffusion coefficient of fluorescein was used, but since the WJ should not only function with fluorescein in mind, the diffusion of other compounds should also be simulated. The diffusion coefficient of some organic compounds are in the region of  $10^{-5} \frac{cm^2}{s}$  to  $10^{-4} \frac{cm^2}{s}$  [72, 73]. For further studying of how the diffusion coefficients change the relative concentration between the outlets a series of simulations were made by varying the diffusion coefficient. The diffusion was simulated for 90 seconds using  $Q_{total} = 4 \frac{mL}{min}$ ,  $C = 1 \frac{mmol}{mL}$ , and 816811 meshing elements with a MEQ of 0.1498. The simulation error was 1.78%. The diffusion coefficients used were  $D_c = 4.25 \cdot 10^{-5} \frac{cm^2}{s}$  and  $D_c = 4.25 \cdot 10^{-4} \frac{cm^2}{s}$  which resulted in compound concentrations of 4.69% and 9.40% in the water stream, respectively. The 10-fold increase in diffusion coefficient only yielded a 0.36%-point increase in compound concentration in the water stream. However, a 100-fold increase in diffusion coefficient increased it to 9.40% indicating that the presented WJ design is best suited for compounds with a diffusion coefficient in the  $10^{-5} \frac{cm^2}{s}$  range.

## 4.6.2 Worm Junction Print

The WJ was designed to function with interchangeable inlets and outlets, such that it can be changed in case of breakage or alterations in the outlet/inlet design. The interlocking system is based on a design by Ryungeun Song et al. that is leak-proofed using O-rings [74]. The design of the WJ, inlets/outlets, and the corresponding 3D printed parts are presented in Figure 4.8.

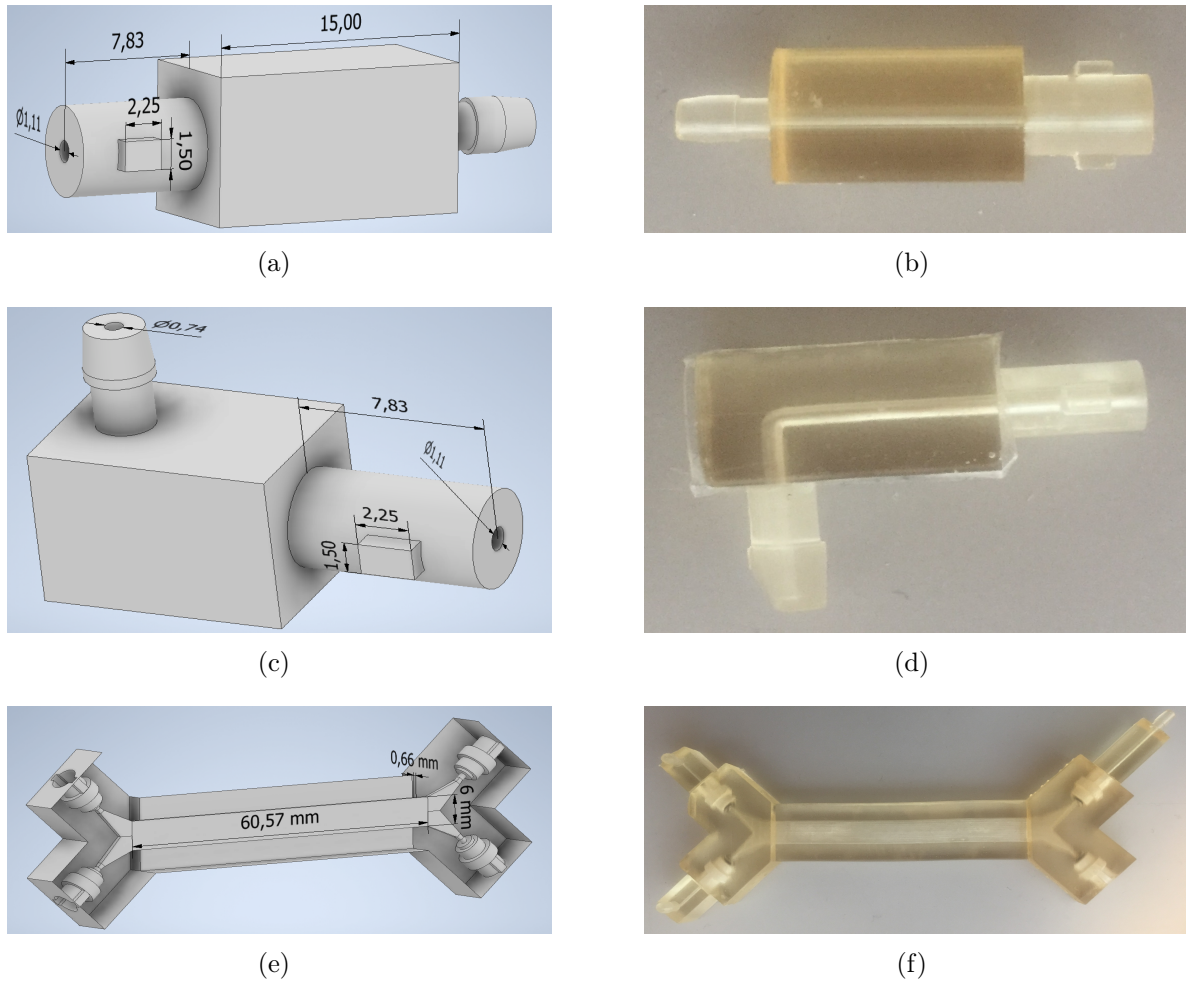


Figure 4.8: All marked dimensions are in millimeters. (a): Design of the inlet to connect with tubing and the WJ. (b): Picture of a printed version of the design in (a). (c): Design of an outlet for collecting samples with a connection piece. (d): Picture of a printed version of the design in (c). (e): Design of the WJ. (f): Picture of a printed version of the design in (e) with one inlet and two outlets connected.

The inner diameter of (a) and (c) (1.11 mm) match the inner diameter within the connection system in the WJ. Printing the inlet/outlet worked without complications, but printing the WJ proved difficult at times. Printing the structure horizontally (or with a slight angle) caused build up of resin in the channel that could not be removed in post-print cleaning with nitrogen blowing or isopropanol despite not being fully polymerized. The best method proved to be a vertical printing (no angle), despite the extremely long printing time (36 hours), as the resin would be cleared from the channel through gravity during printing.

The interlocking inlet/outlet system was prone to breakage, as the forces required to

keep the seal waterproof were too high for the small wings to handle. In case the entire interlocking system broke off, the WJ would have to be scrapped as it would be impossible to remove again. An example of how the interlocking system worked and broke can be seen in Figure 4.8(f). A possible way of reinforcing the interlocking system is through increasing the width of the wings, or increasing the overall thickness of the interlocking parts. Since the interlocking system was more trouble and work than a benefit it was only used for the WJ.

### 4.6.3 Fluorescein Experiments

To test if the printed WJs, seen in Figure 4.8(e) and (f), can be used for chemotaxis experiments and to compare them to the simulations, an experiment with a fluorescein solution and water was made. This was done in accordance with the method described in Section 3.7 to avoid bubbles and gravity influenced changes in the flow profiles. The light absorption of both the fluorescein fraction and the water fraction was measured. Results for multiple WJs are presented in Figure 4.9 with the relative absorbance of fluorescein in % at 474 nm in the water fraction, experiment repeat number, and which WJ is used. All the WJs are identical but have been printed separately.

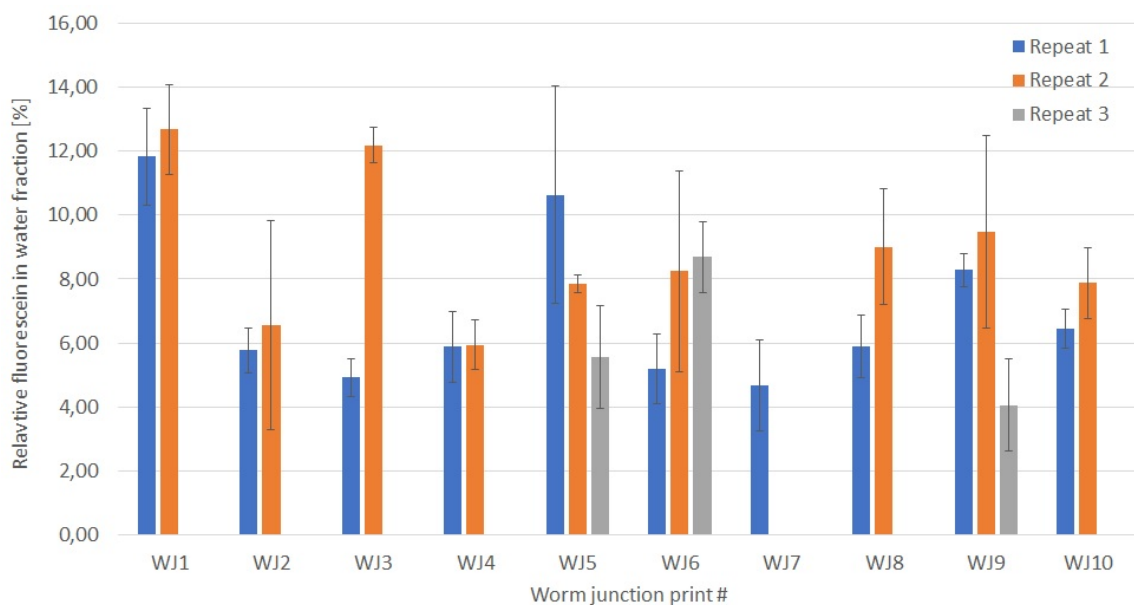


Figure 4.9: Relative absorbance percentage of fluorescein at 474 nm in the water fraction for separately printed WJs. The flowrate at each inlet was  $2 \text{ ml}/\text{min}$ . Each repeat of the experiment consists of at least 5 samples.

Figure 4.9 shows the results of the fluorescein flow experiments. Each result consists of 5 consecutive measurements taken without interrupting the flow. The relative concentration in the water fraction varied from the lowest of  $\approx 4\%$  to the highest of  $\approx 13\%$ . The two biggest difficulties with the design was bubbles and keeping the microfluidic system level enough to avoid gravity induced disparity in flow between the two outlets. Any unevenness between the two outlets were detectable in the relative fluorescein concentration. The unevenness could be corrected using sufficient supporting structure, but can lead to incorrect results if the user is careless. The problem with bubbles may be caused by the aspect ratio between the width and height of the channel (6 mm to 0.66 mm). If a bobble is generated it is likely to stick to the upper and lower walls, yet the flow can continue around the bubble even if it fills half the width of the channel. The bubbles can sometimes be removed by tapping the wall of the microfluidic cell, but may sometimes require emptying the channel entirely and trying again. It may be possible to correct this issue by decreasing the width/height aspect ratio of the channel.

The simulation, as seen in Figure 4.7, resulted in a concentration of 4.33% which corresponds to some of the results of the experiment. The simulation reflects perfect conditions of no external disturbances of flow which are unlikely to be reproducible given the conditions of 3D printed microfluidics and the apparent sensitivity to gravity.

## 4.7 Gradient generator and chamber

Another possible design for a microfluidic system designed for a chemotaxis experiment is the one seen in Figure 2.3. The design consists of a wide chamber with multiple inlets allowing for a concentration gradient perpendicular to the flow direction. To avoid multiple independent inlets with a specific concentration for each, the design is fitted with a gradient generator consisting of a mixing component with a split/combine design.

The first design of the mixing component is based on an article by Shallaan *et. al.* that works on a splitting/combining principle [75]. In this design one of the streams are rotated resulting in a shorter diffusion distance. The design was simulated using COMSOL Multiphysics. The diffusion was simulated for 30 seconds using  $D_c=4.25 \cdot 10^{-6} \frac{cm^2}{s}$ ,  $Q_{total}=1 \frac{mL}{min}$ ,  $C_{max}=1 \frac{mmol}{ml}$  with a mesh consisting of 295407 elements and a MEQ of 0.1496. The results can be seen Figure 4.10.

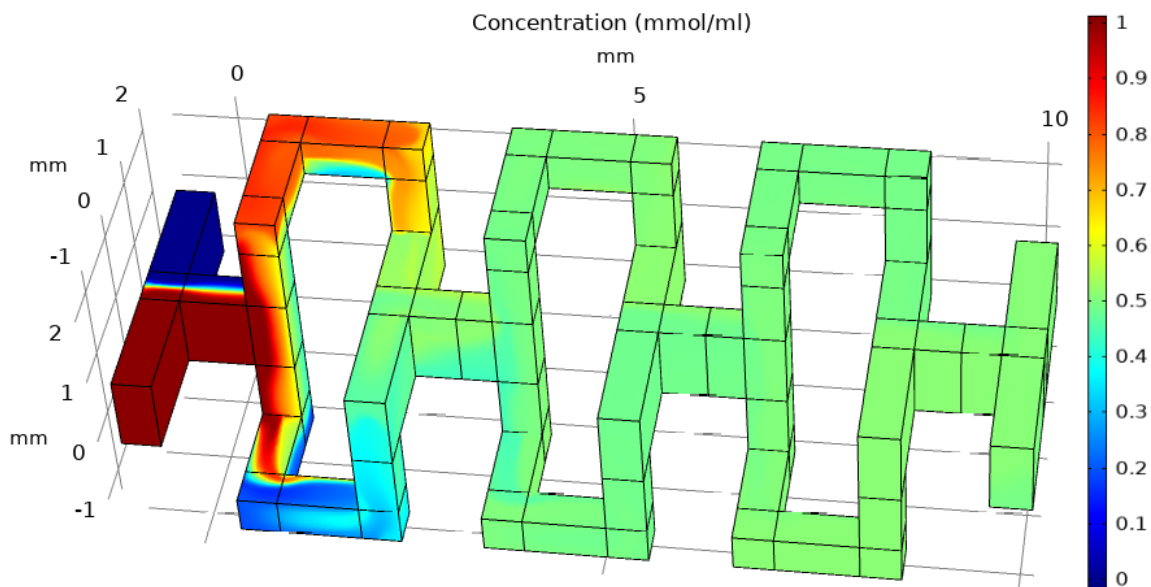


Figure 4.10: Simulation results of transport of diluted species in a mixing component design based upon a design by Shallaan *et. al.* [75]. The dimensions of the wide channels are 1 mm x 0.5 mm and the narrow channels are 0.5 mm x 0.5 mm. The diffusion was simulated for 30 seconds using  $D_c=4.25 \cdot 10^{-6} \frac{cm^2}{s}$ ,  $Q_{total}=1 \frac{mL}{min}$ ,  $C_{max}=1 \frac{mmol}{ml}$  with a mesh consisting of 295407 elements and a MEQ of 0.1496. The simulation error is estimated to be 0.68%.

Figure 4.10 shows the simulation of mixing in the mixing component based upon a design by Shallaan *et. al.* [75]. The mixing is evaluated by the maximum concentration deviation from the average after each split/combine. The deviation is 92.58% after the first, 41.23%

after the second, and 18.26% after the third. While the design is effective at smaller dimensions as compounds have to diffuse a smaller distance, the design is not effective enough at the dimensions that are possible to 3D print in this project. The square channel design is preferred for traditional microfluidic production methods, as they work on a layer by layer basis making creating detailed circular channels difficult. Circular channels are preferred for 3D printing as they require less pressure to achieve fluid flow which makes the channels easier to clean during post-print processing, see Appendix A. The pressure drop from the point at which the two streams meet, over the 3 split/combine units and to the point where the two stream split again is 84.13 Pa. Changing to circular channels and reducing the number of split/combine units should reduce the required pressure. Reducing the number of split/combine units also makes post-print cleaning easier, as ensuring that both channels are cleared simultaneously is not always possible. If one of the channels are cleared before the other further flow is directed into the cleared channel because of path of least resistance. Using high pressure, ultrasonication, and resin solvents has proven to be ineffective in clearing a clogged channel if one is cleared before the other. Thus, a redesign with fewer split/combine units was deemed necessary.

The resulting design, named helix mixer component, is based upon one expanded version of a split/combine unit with circular channels. Initial simulations proved that one split/combine unit was not enough to ensure full mixing, so a coil was added to ensure complete mixing. The new design was simulated for 30 seconds using  $D_c=4.25 \cdot 10^{-6} \frac{cm^2}{s}$ ,  $Q_{total} = 1 \frac{mL}{min}$ ,  $C_{max} = 1 \frac{mol}{L}$  with a mesh consisting of 60449 elements and a MEQ of 0.111. The results can be seen in Figure 4.11.

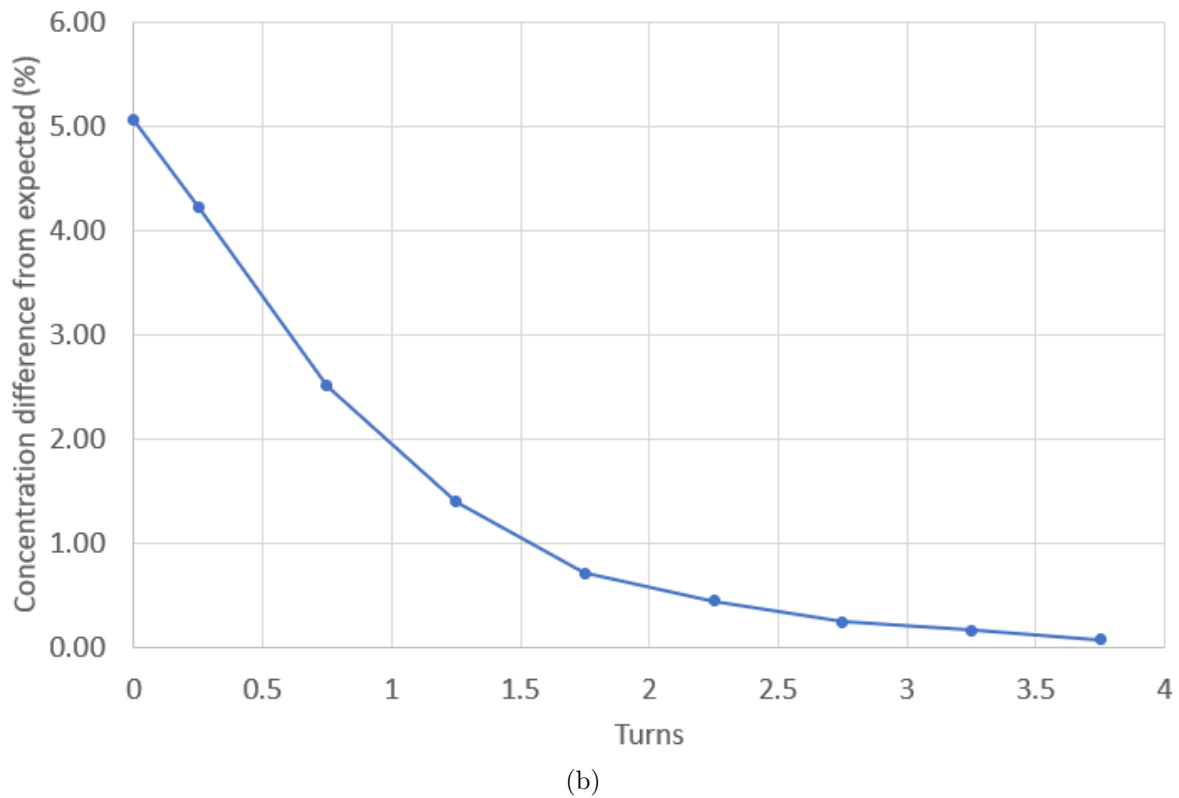
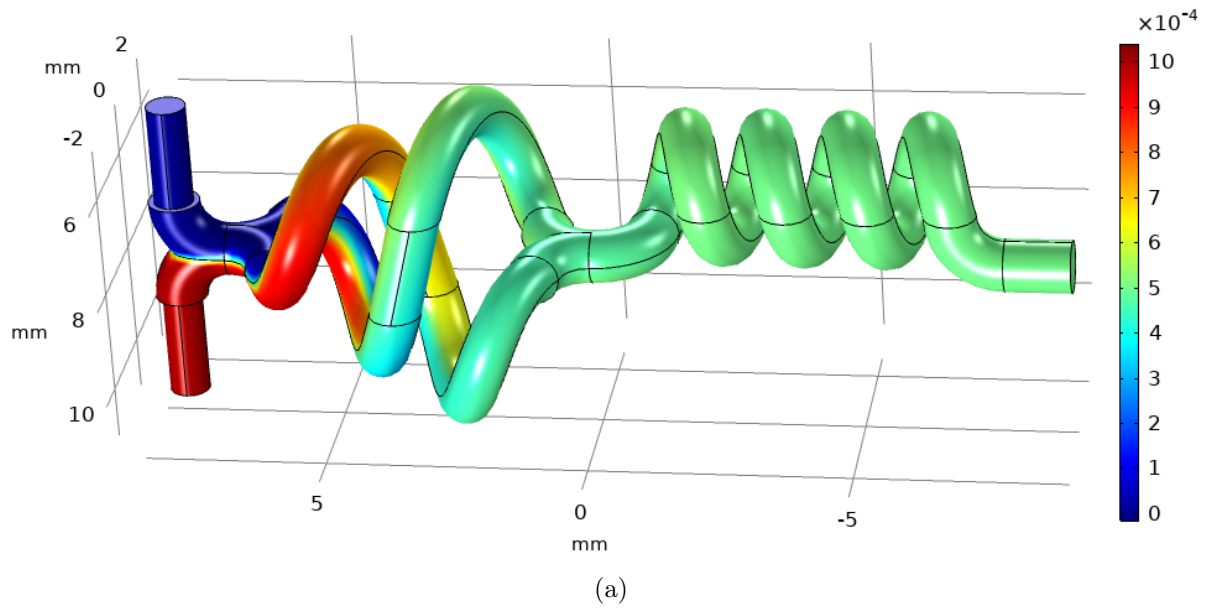


Figure 4.11: (a): Simulation results of transport of diluted species in the helix mixing unit design. The design is based upon the mixing unit seen in Figure 4.10. The diameter of the channels are 1 mm. The diffusion was simulated for 30 seconds using  $D_c=4.25 \cdot 10^{-6} \frac{cm^2}{s}$ ,  $Q_{total} = 1 \frac{mL}{min}$ ,  $C_{max} = 1 \frac{mol}{L}$  with a mesh consisting of 60449 elements and a MEQ of 0.111. The simulation error is estimated to be 0.01%. (b): Result of simulating the mixing of the helix mixer component. The mixing is evaluated by calculating max/min concentration and comparing it to the expected concentration when completely mixed. The values start after the split part.

Figure 4.11(a) shows the simulation of mixing in the redesigned helix mixer component. The mixing is evaluated by the maximum concentration deviation from the average after the split/combine and after each half-turn in the coil unit. The result can be seen in Figure 4.11(b), where turn 0 is taken just after the split/combine unit. After 1.5 turns the concentration difference reaches 1% and is lowered to 0.09 % after 3.75 turns. The pressure from the point at which the two streams meet and to the end of the structure is 30.51 Pa. The design is able to achieve sufficient mixing while also reducing the required pressure making it easier to operate and clean.

Initial printing tests proved it possible to print the helix mixer component, so the component was used in the design of the gradient generator V1. The diffusion of diluted species through the design was simulated for 450 seconds using  $D_c = 4.25 \cdot 10^{-6} \frac{cm^2}{s}$ ,  $Q_0 = 1 \frac{mL}{min}$ , and  $C = 10 \frac{mmol}{m^3}$  with a mesh consisting of 9737656 elements with a MEQ of 0.00434. The results can be seen in Figure 4.12 and Table 4.9.

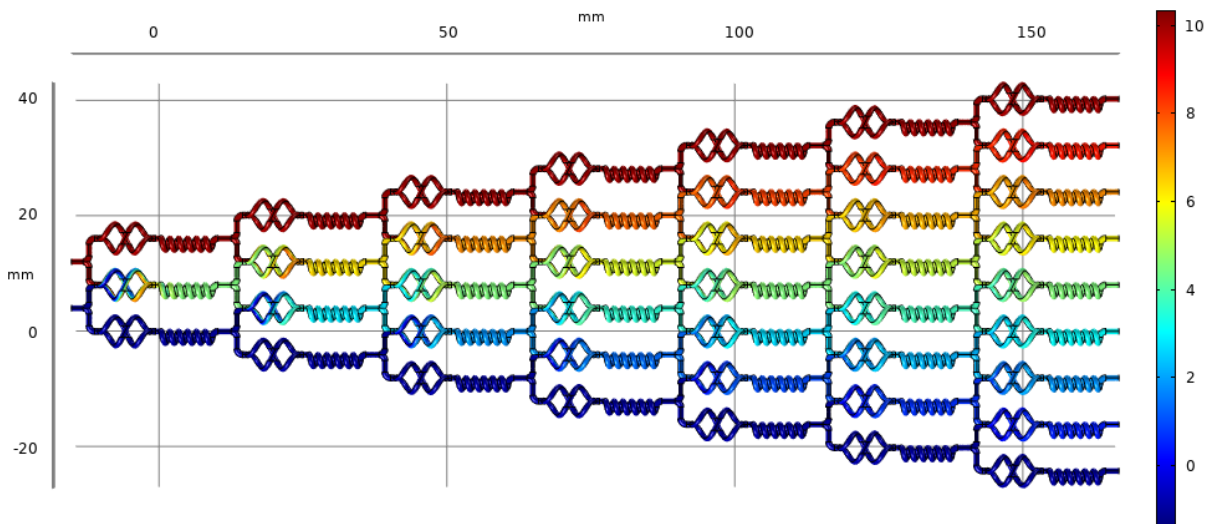


Figure 4.12: COMSOL simulation of the diffusion of diluted species in the gradient generator. Simulated for 450 seconds using  $D_c = 4.25 \cdot 10^{-6} \frac{cm^2}{s}$ ,  $Q_0 = 1 \frac{mL}{min}$ , and  $C = 10 \frac{mmol}{ml}$  with a mesh consisting of 9737656 meshing elements with a MEQ of 0.00434. The calculation error is evaluated to be 3.5%.

The gradient generator V1, seen in Figure 4.12, has been designed to only require two solutions; the maximum concentration and the minimum concentration. The gradient generator consists of a split channel and a spiral for each helix mixer component, which are in parallel with each other, that can be extended with more layers and outlets to

create an increasingly detailed gradient. Optimization of the structure was required as the innermost channels and outlets have a higher flow rate than the outermost channels and outlets. The optimization was performed using the method described in Section 3.6.2. The structure was optimized by narrowing the part connecting the outlet of the previous layer to the inlets of the next layer, resulting in an increased flow resistance towards in middle of the design and thus a relative lower flow resistance in the outer parts of the design. The optimization was done on a layer by layer basis since optimizing all layers simultaneously was too many variables to optimize for. Thus, the first optimization could change the diameter of the connecting parts of the first layer until equal flow between the "outlets" of the first layer was achieved. The next optimization locked the previous diameters, optimized the diameter connecting parts of the next layer until equal flow between the "outlets" of the second layer was achieved while retaining the equal flow between the "outlets" of the previous layer(s). This continued until all layers were optimized. The results of the simulation of diffusion of diluted species after the design was structurally optimization can be seen in Table 4.9.

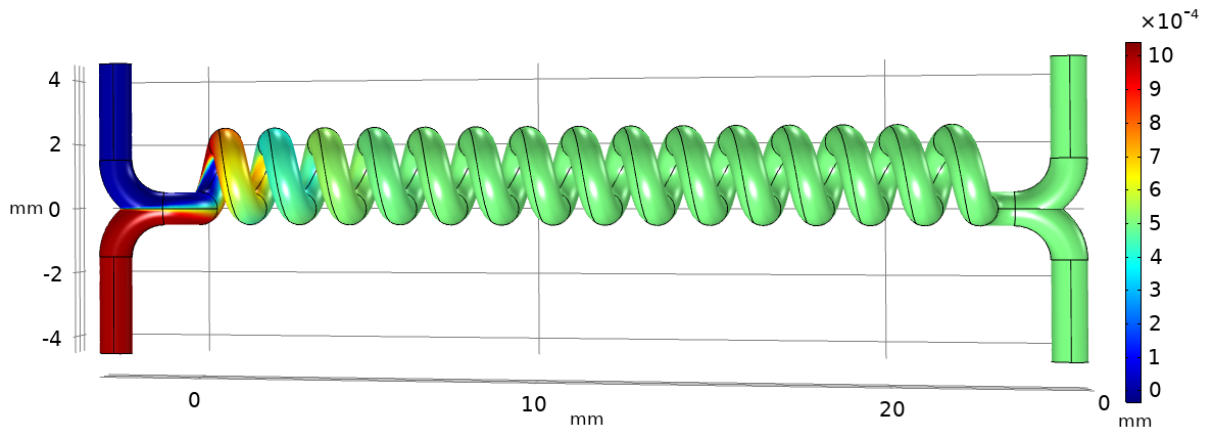
Table 4.9: Flow and concentration results from the gradient generator V1 simulation in Figure 4.12.

Outlet #	Expected V [mL/min]	Result [mL/min]	Error [%]	Expected C [%]	Result [%]	Error [%]
1	0.111	0.103	6.97	0	0	-
2	0.111	0.109	1.53	12.5	13.89	11.10
3	0.111	0.113	2.04	25	26.07	4.28
4	0.111	0.116	4.06	37.5	38.51	2.69
5	0.111	0.116	4.73	50	51.06	2.12
6	0.111	0.116	4.07	62.5	63.61	1.77
7	0.111	0.113	2.04	75	76.04	1.39
8	0.111	0.109	1.50	87.5	88.21	0.81
9	0.111	0.103	6.98	100	100	0

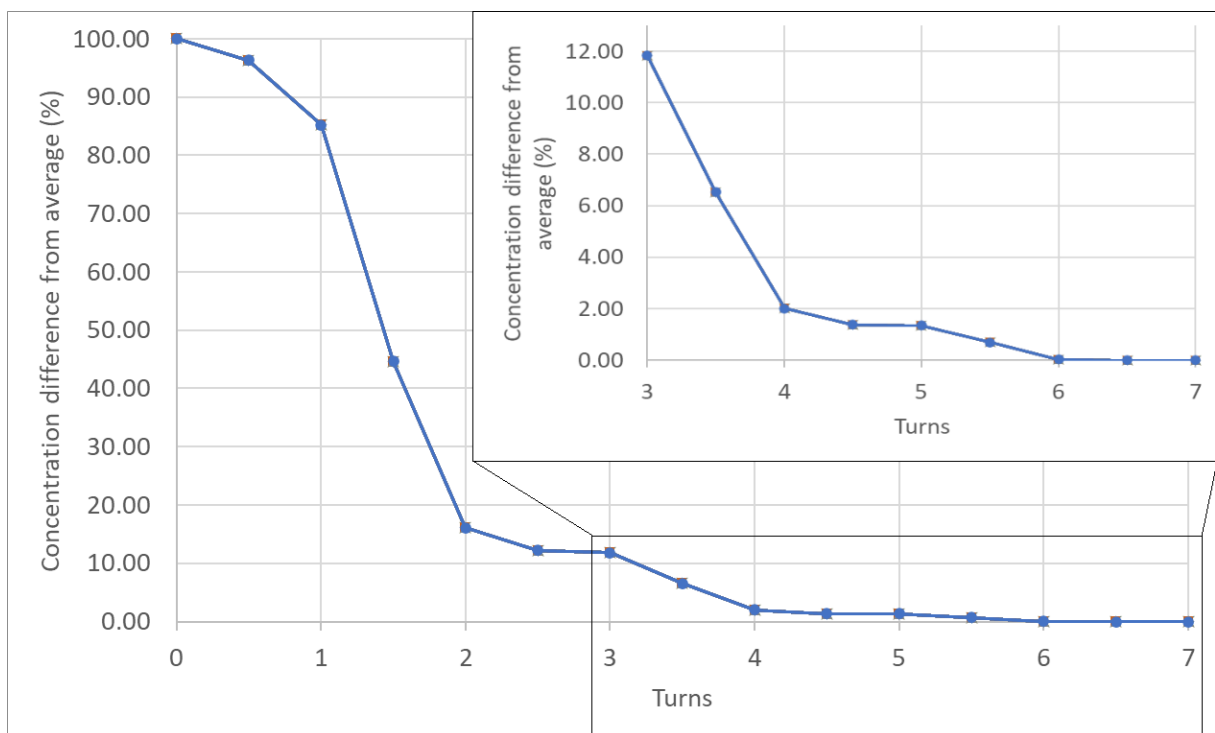
Table 4.9 shows that the flows at the outlets had a deviation of  $<7\%$  from the expected value. The design works on a trade-off between accuracy, structural size, and the resolution of the resulting gradient. Adding more layers to the design increases the gradient resolution but comes at a cost of a larger structure with less accuracy. The loss of accuracy stems from the same problem that the structural optimization tries to solve; higher flow resistance in the outer channels than in the inner channels. As the

flow progresses through the layers a little more is directed towards the center channels. This causes less compound to be directed to the low-concentration side causing a large concentration error in that side, which is increased for each added layer. A reduction in the number of layers is required to limit the error in the concentration. Test prints of the design proved it difficult to ensure that all the split channels were cleared during post-print cleaning when the number of the split channels increased.

To reduce printing difficulty, a new design of the mixing component was made based upon a coil. A simulation of the new mixing component, named coil mixer component, was made. The diffusion was simulated for 30 seconds using  $D_c=4.25 \cdot 10^{-6} \frac{cm^2}{s}$ ,  $Q_{total} = 1 \frac{mL}{min}$ ,  $C_{max} = 1 \frac{mmol}{ml}$  with a mesh consisting of 562315 elements and a MEQ of 0.1361. The results can be seen in Figure 4.13.



(a)



(b)

Figure 4.13: (a): Simulation results of transport of diluted species in the coil mixing unit design. The design is a simplified version of the mixing unit seen in Figure 4.11. The diffusion was simulated for 30 seconds using  $D_c=4.25 \cdot 10^{-6} \frac{cm^2}{s}$ ,  $Q_{total} = 1 \frac{mL}{min}$ ,  $C_{max} = 1 \frac{mmol}{ml}$  with a mesh consisting of 562315 elements and a MEQ of 0.1361. The simulation error is estimated to be 0.33%. (b): Result of simulating the mixing in the coil mixer component. The mixing is evaluated by calculating max/min concentration and comparing it to the expected concentration at when completely mixed.

Figure 4.13(a) shows the simulation results of the coil mixer component and (b) shows the calculated concentration difference. The coil mixer component achieves the same level of maximum concentration difference ( $\approx 5\%$ ) in between 3.5 and 4 coil turns as the

helix mixer component does with the split/combine part. The corresponding length of 3.5 coil turns is 4.5 mm whereas the split/combine unit is 7 mm long. The number of turns required to achieve  $<1\%$  concentration deviation is 5.5 turns. The pressure from the point at which the two streams meet and over 5.5 turns in the coil is 26.47 Pa. The split/combine unit of the helix mixer component can be changed to a simple coil structure reducing printing difficulty and the overall size of the structure.

A new gradient generator, called gradient generator V2, was designed using the coil mixer component with 5.5 turns. A simulation of the transport of diluted species through the redesigned gradient generator V2 was made. The diffusion was simulated for 60 seconds using  $D_c = 4.25 \cdot 10^{-6} \frac{cm^2}{s}$ ,  $Q_{Total} = 1 \frac{ml}{min}$ , and  $C = 1 \frac{mmol}{ml}$ . The mesh had 498735 elements with a MEQ of 0.19 and a calculation error of 2.8%. The results can be seen in Figure 4.14 and Table 4.10.

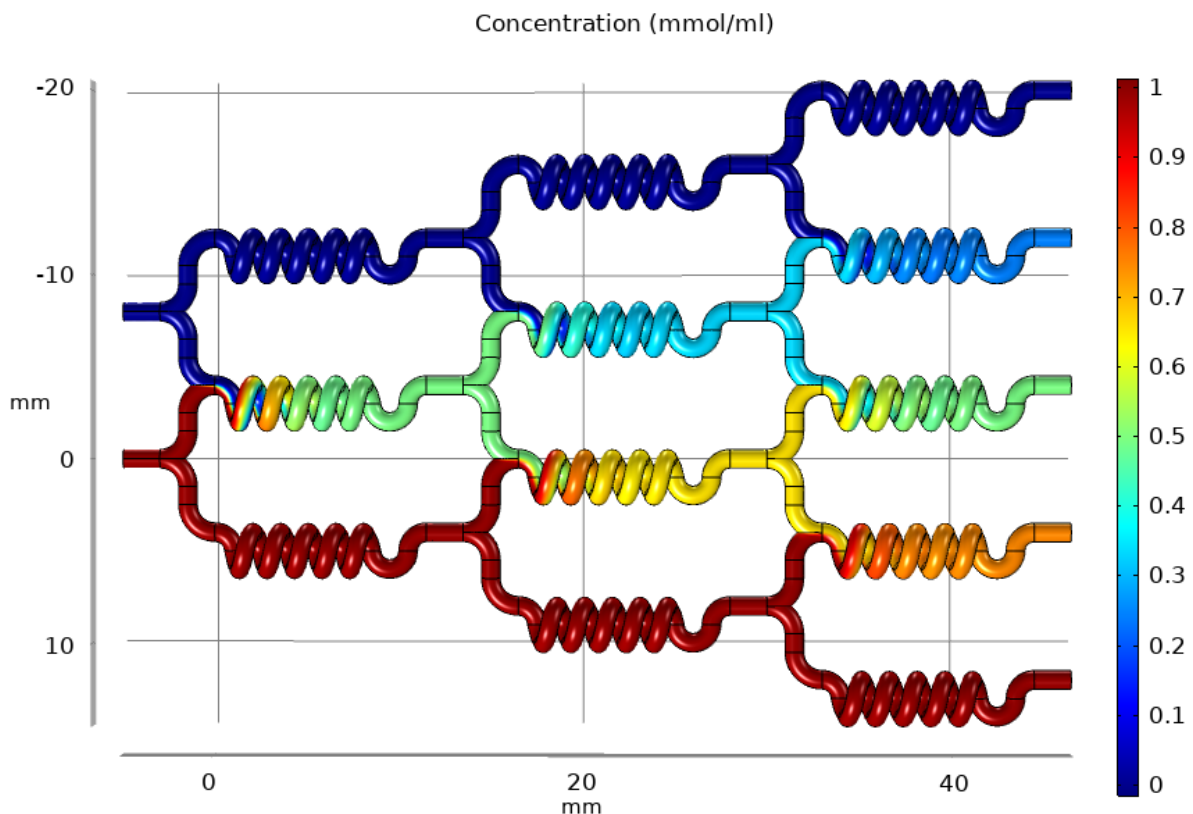


Figure 4.14: COMSOL simulation of the diffusion of diluted species in the gradient generator V2. Simulated for 60 seconds using  $D_c = 4.25 \cdot 10^{-6} \frac{cm^2}{s}$ ,  $Q_{Total} = 1 \frac{ml}{min}$ , and  $C = 1 \frac{mmol}{ml}$ . The mesh had 498735 elements with a MEQ of 0.19 and a calculation error of 2.8%.

Like gradient generator V1, gradient generator V2 has been designed to only require two solutions; the maximum concentration and the minimum concentration. The design was reduced to five outlets to reduce the printing difficulty with a resulting 5 step gradient from 0% to 100%. The results of the simulation can be seen in Table 4.10.

Table 4.10: Flow and concentration results from gradient generator V2 simulation, see Figure 4.14. Q is the volumetric flow and C is the concentration.

Outlet #	Expected Q [ $\mu\text{L}/\text{min}$ ]	Result [ $\mu\text{L}/\text{min}$ ]	Error [%]	Expected C [%]	Result [%]	Error [%]
1	200	191	4.5	0	0	-
2	200	205	2.5	25	24	4
3	200	209	4.5	50	49.3	1.4
4	200	205	2.5	75	74.8	0.3
5	200	191	4.5	100	99.4	0.6

Table 4.10 shows the results of the simulation of the gradient generator V2. The flow is highest in the middle and lower in the sides. The error in the concentration gradient has been reduced from 11.1% in V1 to 4% in V2, but the same tendency of a higher error in the low concentration region is observed in both versions of the gradient generator. Because the error in concentration was only 4%, stemming in part from the reduced number of layers it was deemed unnecessary to further optimize the structure. The gradient generator V2 was printed successfully, see Figure 4.15.

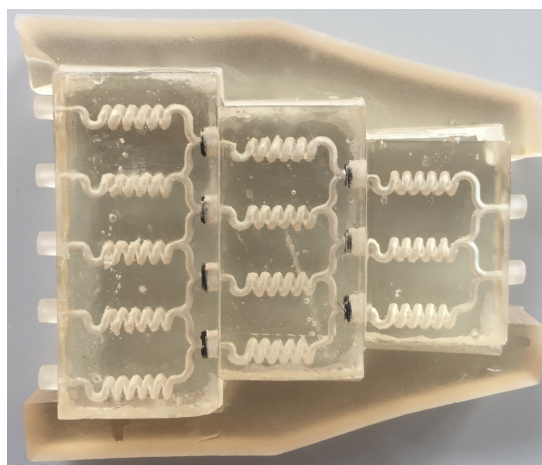


Figure 4.15: Image of the 3D printed gradient generator V2. The surface was coated with nail polish.

Figure 4.15 shows the printed gradient generator V2 used for testing the gradient produced by the structure. All channels were successfully cleaned, but the structure was divided into segments, as post-print cleaning of all the channels was impossible otherwise. Each segment is connected with a small inlet/outlet system that is leak-proofed using an O-ring and a clamp-structure to tighten the segments together. The segmentation of the structure was necessary for the same reason the removal of the split/combine unit was necessary; parallel channels. Applying equal pressure to parallel channels in the middle of the structure is not always possible, as some channels may be cleared by gravity during printing. If one of the parallel channels are opened before the other cleaning the closed channel becomes impossible. Splitting the structure into segments removes this problem, since each channel can be cleaned individually.

The gradient generator V2 was tested using the method used for testing the WJ, see Figure 4.15. The experiment is made using a total flow of 1 ml/min with the samples taken sequentially. Fluorescein with NaOH was used as the diffusing compound, and the samples were diluted to give an absorption between 0.1 and 0.8. The results are evaluated at a wavelength of 489 nm, and are presented in relative absorption to the absorption of outlet 5, see Table 4.11.

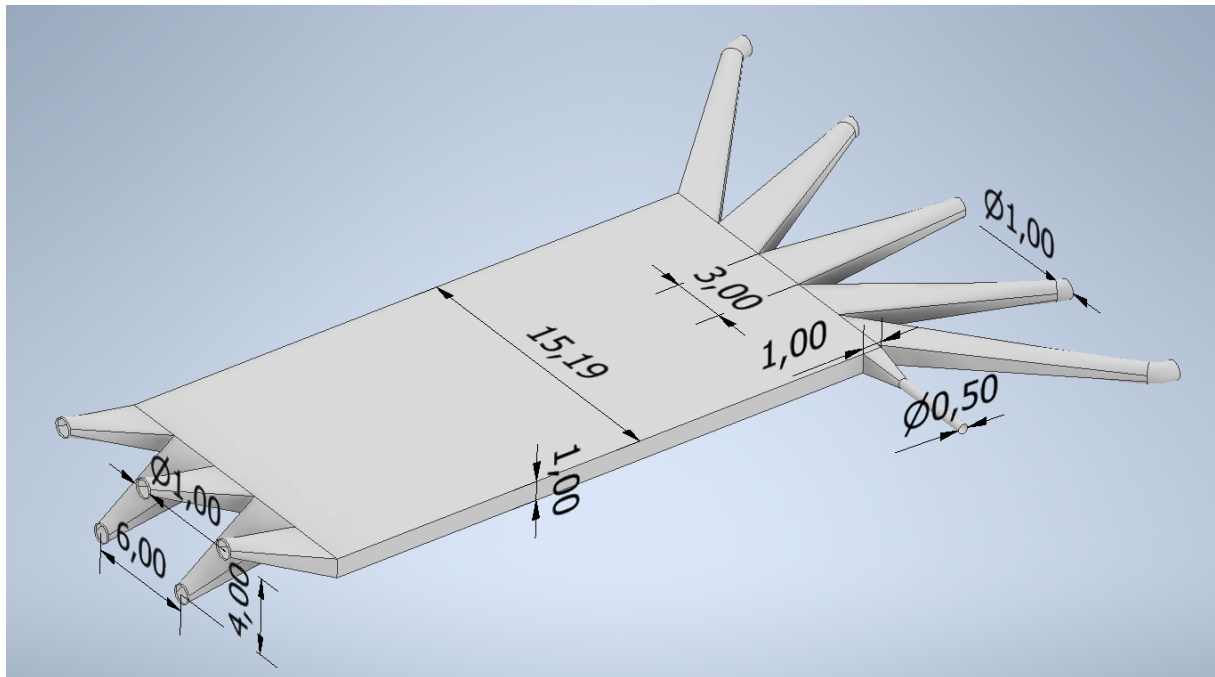
Table 4.11: Concentration results from gradient generator V2 test, see Figure 4.15. C is the concentration.

Outlet #	Expected C [%]	Result C [%]	Std. [%]	Error [%]
1	0	0.48	0	-
2	25	12.12	0.04	51.52
3	50	69.64	3.23	39.28
4	75	94.83	0.26	26.44
5	100	100	0.77	0

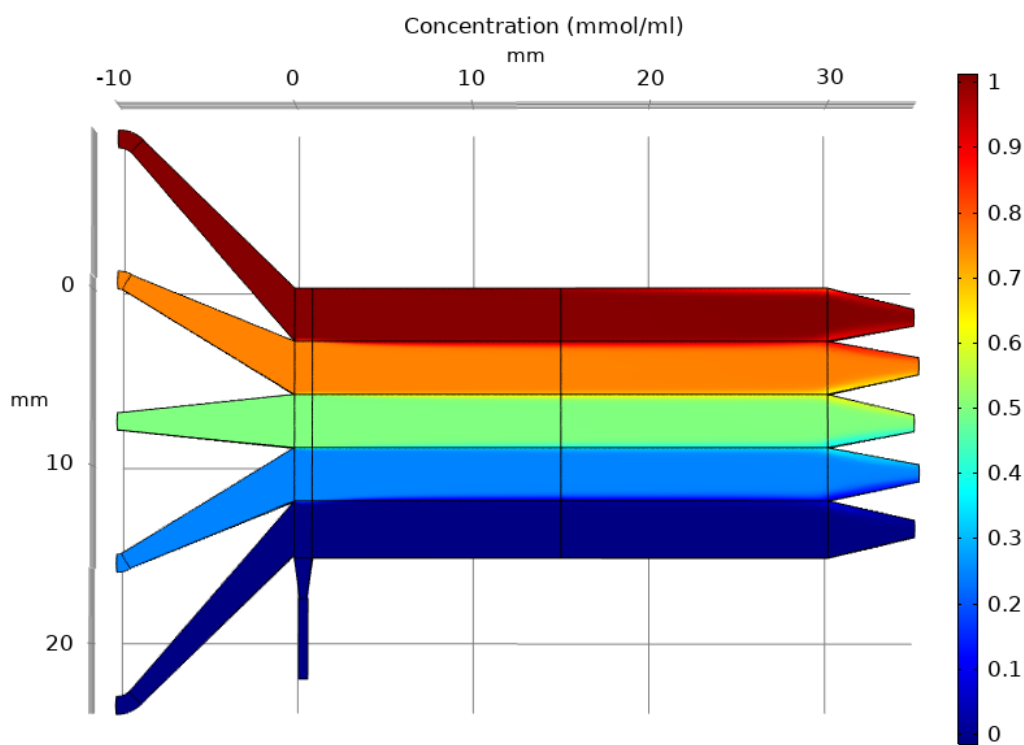
The results of testing the concentration gradient generated by gradient generator V2 can be seen in Table 4.11. The largest error, as expected, is in the low concentration region, which is a problem that was discussed earlier. The experiment is not an example of the gradient generator functioning correctly, but instead an example of one the major flaws. Bubbles were impossible to remove caused by the same issue previously discussed; parallel

channels. Every time a bubble is generated, which happens frequently due to the rough surface of the channels, flow is redirected into a parallel channel. Tapping the structure can remove bubbles, but is a slow and ineffective procedure. The time and ease gained from using a gradient generator may be lost if the preparation of the generator exceeds the time required for making the gradient manually. Further reduction of surface roughness is required if 3D printable designs with parallel channels are to be used.

A chamber was designed to work in conjunction with the gradient generator V2 as the chemotaxis experiment chamber where *C. elegans* would be injected. The design is made with an additional side inlet where the worms will be injected. The additional flow from the side inlet is accounted for by widening the chamber such that the additional flow has the same flow speed as the remaining chamber. A diffusion of diluted species simulation of the experiment chamber was made to simulate how much each gradient zone diffuses into each other. Simulations are made with and without flow from the side inlet. The diffusion was simulated for 300 seconds using  $D_c = 4.25 \cdot 10^{-6} \frac{cm^2}{s}$ ,  $Q_{maininlets} = 1 \frac{mL}{min}$ ,  $V_{sideinlet} = 1 \frac{mm}{s}$  and  $C_{max} = 1 \frac{mmol}{ml}$  with a mesh consisting of 1665642 elements and a MEQ of 0.048. The results can be seen in Figure 4.16 and Table 4.12.



(a)



(b)

Figure 4.16: (a): Inner structure of the flow chamber designed to work in conjunction with the gradient generator V2 as a chemotaxis microfluidic system. The dimensions are in mm. (b): COMSOL simulation of diffusion of fluorescein in the cascade chamber. Simulated with flow from the side inlet. Simulated for 300 seconds using  $D_c = 4.25 \cdot 10^{-6} \frac{cm^2}{s}$ ,  $Q_{maininlets} = 1 \frac{mL}{min}$ ,  $V_{sideinlet} = 1 \frac{mm}{s}$  and  $C_{max} = 1 \frac{mmol}{ml}$  with a mesh consisting of 1665642 elements and a MEQ of 0.048. The simulation error is estimated to be 0.47%.

Figure 4.16(b) shows a transport of diluted species simulation in the flow chamber designed to work in conjunction with the gradient generator V2. The inlets (left side) are spaced to connect with the outlets of the gradient generator V2. The smaller inlet is made for continuous injection of e.g. *C. elegans* into the system. The outlets are spaced in a zig-zag formation to give space for tube connections. Gravity was accounted for in the simulation to calculate the effect of the zig-zag formation. The flow and concentration errors can be seen in Table 4.12.

Table 4.12: Flow and concentration results from the flow chamber simulations, see Figure 4.16. Q is the volumetric flow and C is the concentration.

Worm inlet on						
Outlet #	Expected Q [ $\mu\text{L}/\text{min}$ ]	Result [ $\mu\text{L}/\text{min}$ ]	Error [%]	Expected C [%]	Result [%]	Error [%]
1	211.48	207.19	2.02	0	0.284	-
2	200	201.67	0.835	25	24.434	2.26
3	200	201.71	0.855	50	49.716	0.568
4	200	201.46	0.73	75	75.160	0.21
5	200	199.43	0.285	100	98.849	1.15
Worm inlet off						
Outlet #	Expected Q [ $\mu\text{L}/\text{min}$ ]	Result [ $\mu\text{L}/\text{min}$ ]	Error [%]	Expected C [%]	Result [%]	Error [%]
1	200	204.84	2.42	0	1.4842	-
2	200	199.38	0.31	25	25.672	2.688
3	200	199.42	0.29	50	50.601	1.202
4	200	199.18	0.41	75	75.633	0.844
5	200	197.17	1.415	100	99.154	0.846

Results of the flow and concentration from the simulations are presented in Table 4.12. Introducing flow from the worm inlet into the system creates higher flow in the low concentration side of the chamber, as expected. Due to the inlet being situated perpendicular to the flow direction some flow is directed towards the higher concentration areas. A solution to this problem would be to introduce the inlet parallel to the flow, but this would launch the worms too quickly towards the outlets. By having the inlet

perpendicular to the flow the nematodes are given more time to explore the gradient, reducing the risk of false negative results. The highest error in concentration is 2.26% which should be acceptable.

The simulation with no flow from the worm inlet was made to mimic injecting worms in small volumes. The concentration error in the low concentration area is higher than with the inlet on. This is to be expected as the additional flow from the inlet is not filling the additional space made for the flow.

An evaluation of the concentration profile across the flow chamber was made to evaluate how wide the transition area between the concentration steps are, see Figure 4.17. The transition area between each step when the worm inlet is off is between 1.2 mm and 1.5 mm centered around the position of the outlets. When the worm inlet is on, the transition area is likewise between 1.2 mm and 1.5 mm, but is slightly off-centered from the outlets in the low concentration area. This is likely caused by the perpendicular flow introduced from the inlet shifting the flow sideways and thus shifting the positioning of the transition area.

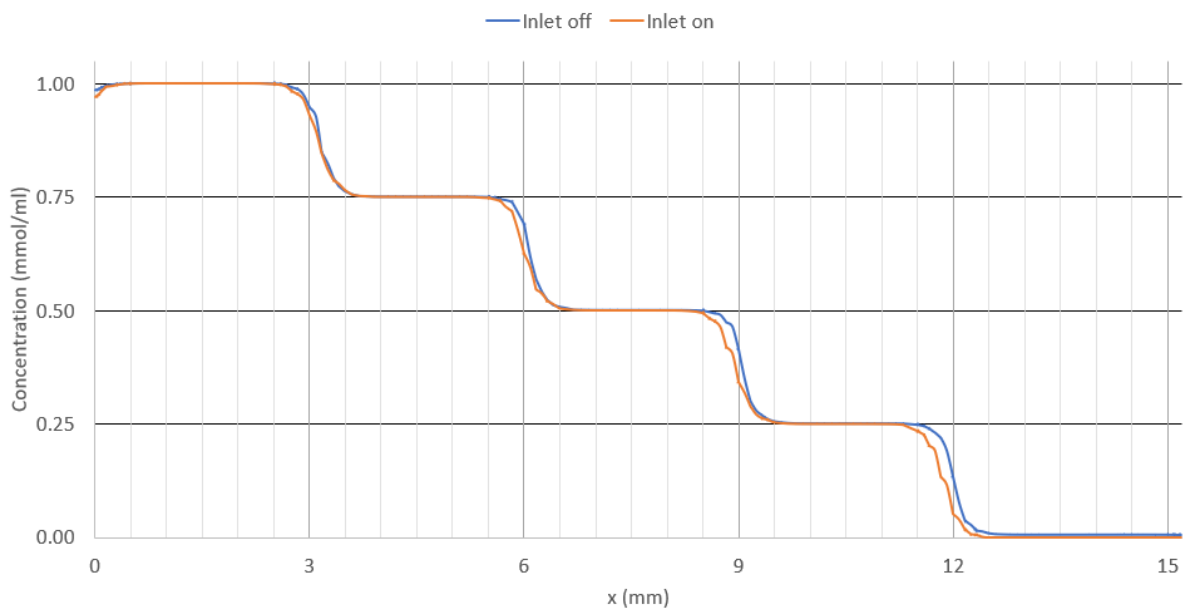


Figure 4.17: Concentration profile from the flow chamber simulation. The profile is evaluated from a line spanning from each side of the chamber, 2 mm from where the chamber splits into the outlet channels.

## 4.8 Droplet Generator

The droplet generator has been designed using Autodesk Inventor to use as a stand alone component and in combination with electrospinning. The design is based on a flow focusing design that accelerates the flow for a short period before deceleration at the orifice exit. The acceleration/deceleration destabilizes the thread head causing spontaneous formation of droplets [76].

The inlets/outlets are made with a luer lock design for easy connection with external tubing.

Figure 4.18 shows the Autodesk Inventor schematic of the inner channel design and the 3D printed version with the surrounding structure. The MFS of the droplet generator refers to the diameter of the flow focusing channel.

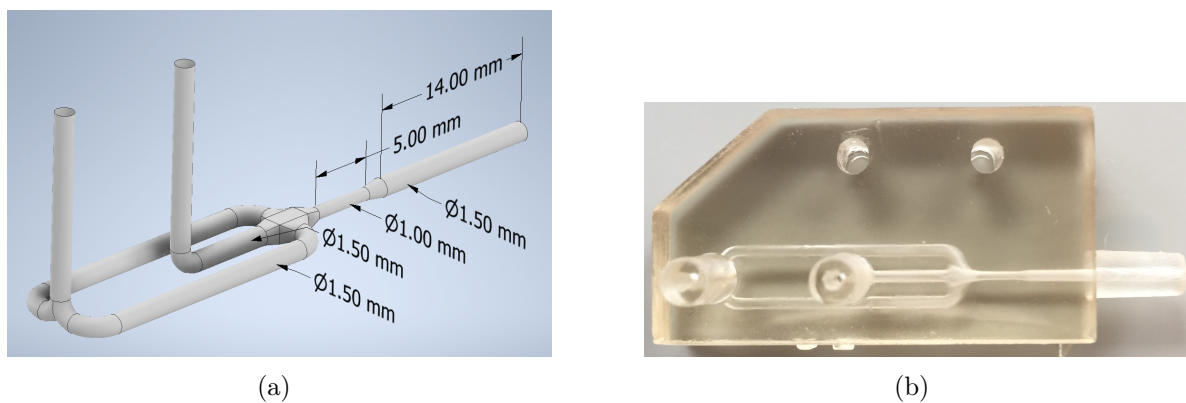


Figure 4.18: (a): Design of channels of the droplet generator with marked dimensions for the flow focusing channel (1 mm diameter), the inlet channels (1.5 mm diameter), and the outlet channel (1.5 mm diameter). (b): Picture of a 3D printed version of the design in (a).

### 4.8.1 Droplet Generator Experiment

The experiment using the droplet generator was performed according to the method described in Section 3.9. The test was performed using PVA in water as the continuous phase and grape seed oil with Nile red as the dispersed phase. Nile red was added to increase the visibility of the droplets. The droplet generator was connected to a silicone tube, which was put under a microscope. When a steady stream of droplets was observed in the silicone tube a picture was taken to determine the average droplet size. An example of the droplets generated can be seen in Figure 4.19.

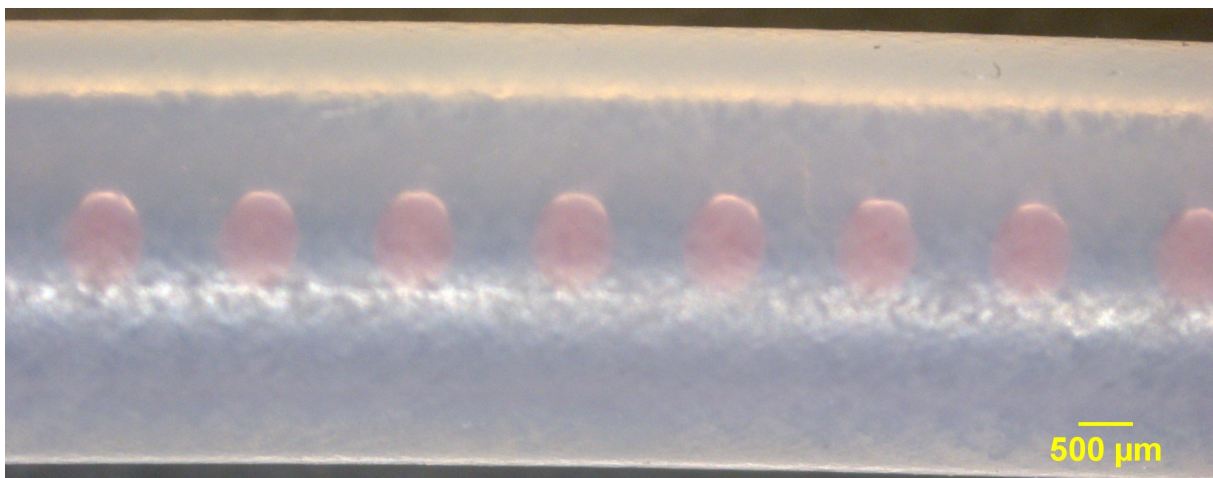


Figure 4.19: Image of droplets in a silicone tube generated using a 3D printed droplet generator. The flowrate of 8% PVA was  $200 \frac{\mu\text{l}}{\text{min}}$  and the flowrate of grape seed oil was  $20 \frac{\mu\text{l}}{\text{min}}$ . The average size of the droplets is  $726 \mu\text{m} \pm 18 \mu\text{m}$ . The MFS of the droplet generator was 0.8 mm and the inlet/outlet diameter was 1.2 mm. The silicone tube had an inner diameter of 2.6 mm.

Figure 4.19 shows droplets of grape seed oil in 8% PVA generated using a droplet generator with a 0.8 mm MFS and using flowrates  $Q_{PVA} = 200 \frac{\mu\text{l}}{\text{min}}$  and  $Q_{oil} = 20 \frac{\mu\text{l}}{\text{min}}$ . The droplets were oval in shape and were measured in the direction of the flow.

A series of measurements of grape seed oil droplets in PVA were generated using droplet generators with the MFS varying from 0.6 mm to 0.8 mm. Nile red was added to the grape seed oil to increase the visibility of the droplets. The concentration of PVA was either 8% or 14% and 3mM SDS was added to some samples. The flow of PVA was set to  $200 \frac{\mu\text{l}}{\text{min}}$  for all samples, and the flow of grape seed oil was varied between  $20 \frac{\mu\text{l}}{\text{min}}$  and  $120 \frac{\mu\text{l}}{\text{min}}$ . The results can be seen in Figure 4.20.

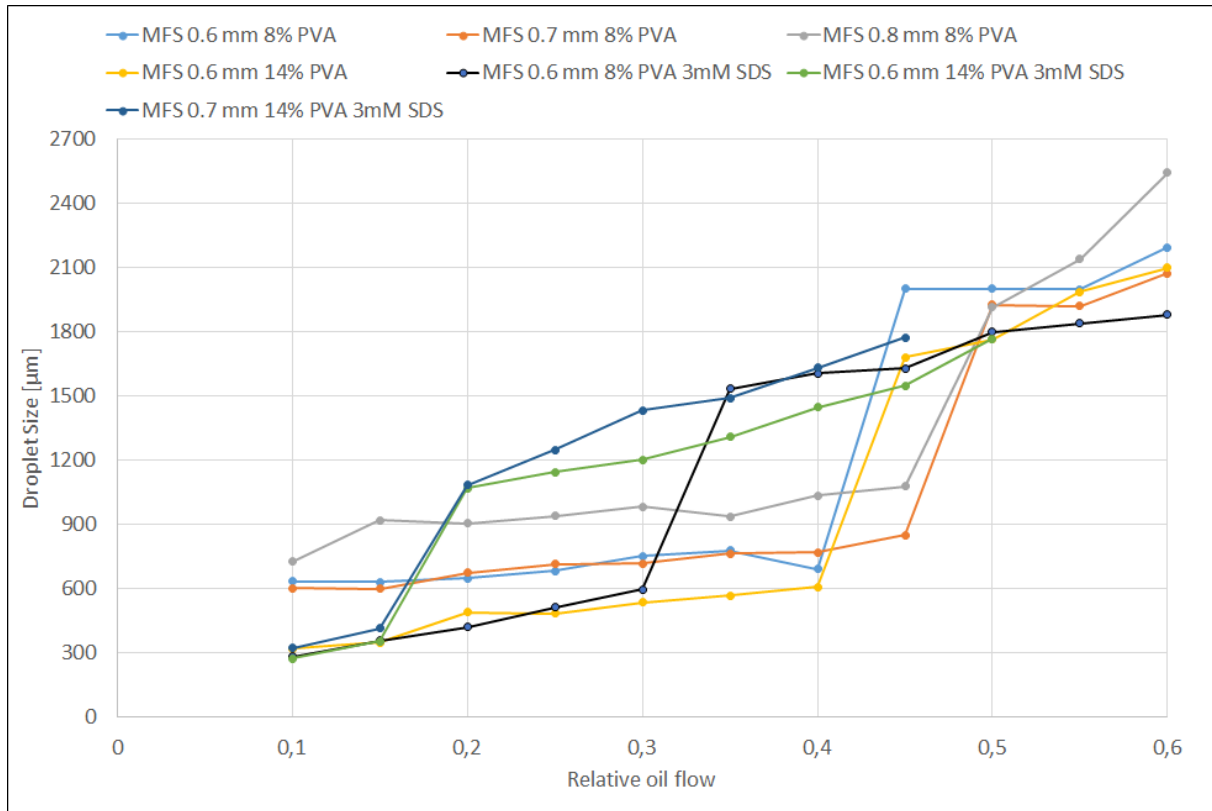


Figure 4.20: Plot of droplet diameter as a function of relative dispersed flow rate. The droplets were generated using the design seen in Figure 4.18. The continuous phase flow rate was a constant  $200 \mu\text{l}/\text{min}$ .

Figure 4.20 shows the droplet sizes as a function of relative dispersed flow rate. The droplets were generated using droplet generators with a varying MFS. Increasing the MFS of the droplet generator resulted in an overall increase in droplet size except for MFS 0.6 mm and 0.7 mm 8% PVA at lower relative oil flows. Increasing the PVA concentration from 8% to 14%, and thus the viscosity of the continuous phase, lowered the droplet size. The droplet size is inversely dependent on the viscosity ratio between the continuous phase and the dispersed phase ( $\lambda = \frac{\eta_d}{\eta_c}$ ). The droplet size decreases as the ratio goes towards 1 after which it starts increasing again [77, 78]. The viscosity ratio for 8% PVA and grape seed oil is approximately 0.195, which is increased to 0.79 for 14% PVA explaining the observed decrease in droplet size.

A sharp increase in size was observed for all samples, as the flow of grape seed oil increased. Increasing the PVA concentration and/or adding SDS to the PVA solution lowered the relative grape seed oil flow required for the sharp increase in size to occur. This can

be explained by the different droplet generating mechanisms that happens at different conditions [77]. The first is the transition area between squeezing and dripping, which is observed in Figure 4.21(a,b). Here the emerging droplet partially and temporarily blocks the continuous flow that causes a build-up of pressure in the continuous flow. The droplet formation is caused by both squeezing pressure and viscous shear as the continuous flow pushes on the dispersed phase and moves faster past the dispersed phase [77]. The second droplet generating mechanism is dripping where viscous forces drag the interface until it overcomes the interfacial tension ultimately rupturing the interface. This mechanism is observed in Figure 4.21(d) which is caused by the increased viscosity of 14% PVA compared to 8% PVA observed in Figure 4.21(a,b). The third droplet generating mechanism is jetting which is a transition from dripping that can occur as the flow rate of the dispersed phase or continuous phase is elevated. Jetting is when an extended liquid jet of dispersed phase is emitted from the dispersed channel that ultimately breaks into droplets at the end of the jet due to stream vibrations called Rayleigh-plateau instability [77]. The jet extension is caused by viscous-drag forces overwhelming the capillary force, stabilizing the dispersed flow inside the continuous flow until Rayleigh-plateau instability breaks the flow. Jetting is split up into two different regimes. The first is the narrowing jetting regime, where the continuous flow is larger than the dispersed flow which thins the jet as it extends resulting in small droplets, see Figure 4.21(e). The second is the widening jet regime which happens as the dispersed flow increases, nearing or exceeding the continuous flow. This causes the dispersed flow to decelerate as it moves downstream where the velocity difference causes viscous shear at the interface resulting in jet widening, and thus larger, but less frequent, droplets, see Figure 4.21(c) [77]. Increasing the dispersed flow rate stabilizes the jet, extending it further into the channel, see Figure 4.21(f).

An increased stability of the flow of oil within the flow of PVA was observed when adding SDS to the PVA solution, as the point of droplet formation moved further and further towards the outlet. The droplet formation had moved past the droplet size detection point for higher relative oil flows of 14% PVA 3 mM SDS solutions. This phenomenon can be explained through the interplay of capillary pressure and viscous drag force that causes the jetting that generates the droplets. Lowering the interfacial tension through

the addition of surface active agents reduces the capillary force thus stabilizing the jet causing it to travel further in the stream before capillary force overcomes the viscous-drag force [77]. Likewise, the reason the jet did not extend just as far for the 8% PVA with 3 mM SDS sample is the reduced viscosity of the continuous phase not stabilizing the jet as strongly as the higher viscosity of the 14% PVA with 3 mM SDS solution.

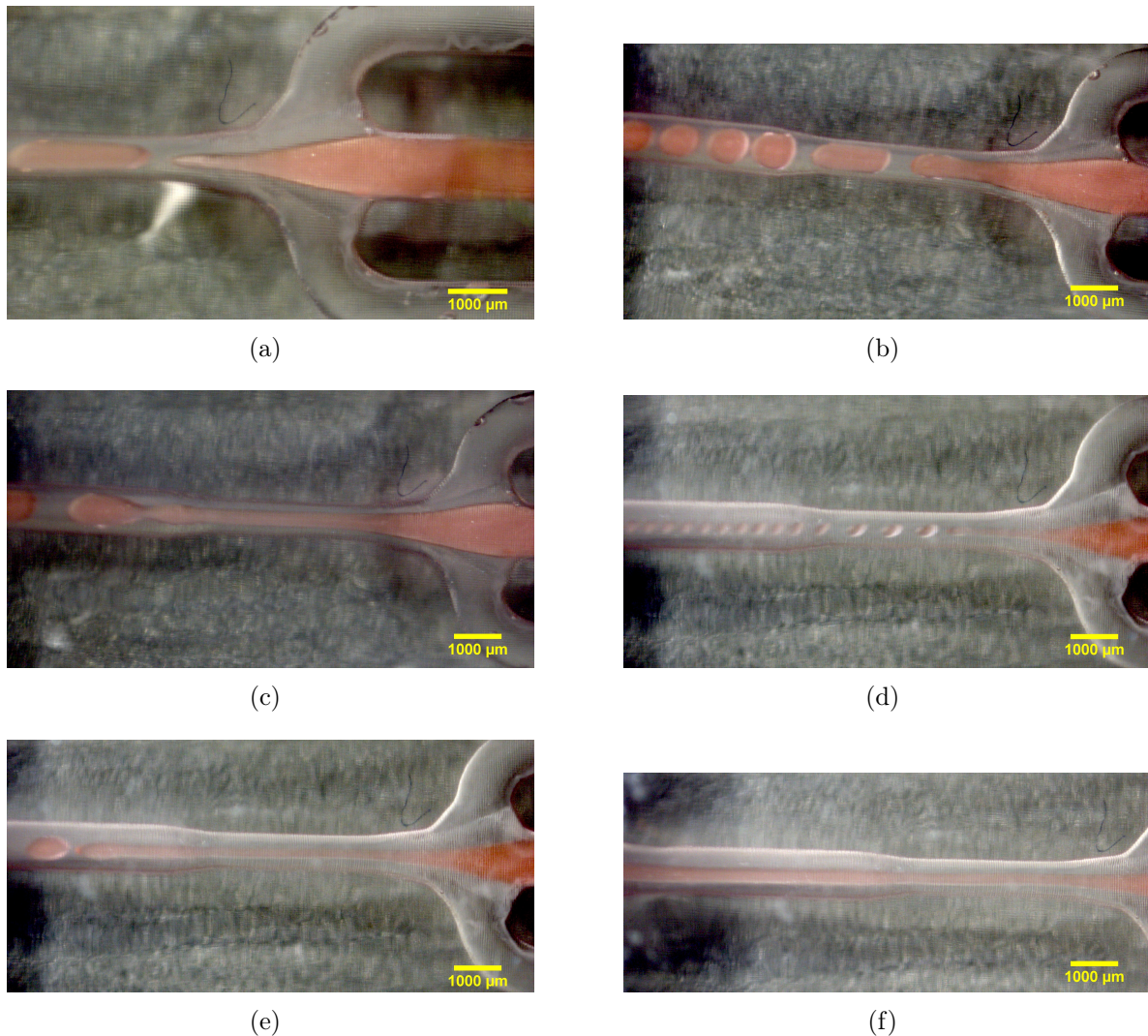


Figure 4.21: Pictures of droplet formation in a droplet generator with a MFS of 0.7 mm. All PVA flows are  $200 \frac{\mu\text{l}}{\text{min}}$ . (a): 8% PVA,  $20 \frac{\mu\text{l}}{\text{min}}$  grape seed oil, dripping/squeezing. (b): 8% PVA,  $70 \frac{\mu\text{l}}{\text{min}}$  grape seed oil, dripping/squeezing. (c): 8% PVA,  $120 \frac{\mu\text{l}}{\text{min}}$  grape seed oil, jet widening. (d): 14% PVA,  $20 \frac{\mu\text{l}}{\text{min}}$  grape seed oil, dripping. (e): 14% PVA,  $70 \frac{\mu\text{l}}{\text{min}}$  grape seed oil, jet narrowing. (f): 14% PVA,  $120 \frac{\mu\text{l}}{\text{min}}$  grape seed oil, extended jet widening.

### 4.8.2 Simulating the Droplet Generator

The simulations of the droplet generator was made to achieve results similar to the experimental results of the previous section. When similar results are obtained further expansion of tested variables can be performed that are difficult to perform experimentally. This can be variables such as viscosity, interfacial tension, and flow rates that can be difficult to change independently experimentally as they can be linked with other variables. The simulations were performed using COMSOL Multiphysics, with an 8% PVA or 14% PVA in water solution as the continuous phase and grape seed oil as the dispersed phase. All user specified values that are used in the simulations, unless otherwise stated, are listed in Table 3.4.

The specific values for the contact angle and interfacial tension are not available for an 8% PVA and grape seed oil solution, therefor an estimation was used. The value of the contact angle was chosen based on wettability. When the angle is between  $90^\circ$  and  $180^\circ$  there is low wettability and should minimize contact to the surface of the droplet generator. However based on physical observations the droplets were not in contact with the surface, therefor  $\pi$  rad ( $180^\circ$ ) was chosen, see Figure 4.21. The interfacial tension for grape seed oil in a PVA solution was estimated based on its compositional similarity to sunflower oil. Sunflower oil has an interfacial tension of  $23.91 \pm 0.06$  mN/m in water at pH 6 and  $25^\circ\text{C}$  [79, 80]. This leads to an estimate of 24.0 mN/m for the interfacial tension of grape seed oil in PVA in the simulations.

The first simulations were made with the same setting as the experiments in Figure 4.21: A MFS of 0.7 mm, 8% PVA and 14% PVA,  $Q_{PVA}=200\frac{\mu\text{l}}{\text{min}}$ ,  $Q_{Grapeseedoil}=[20, 70, 120]\frac{\mu\text{l}}{\text{min}}$ . The mesh consisted of 54625 elements with a MEQ of 0.2361. The results can be seen in Figure 4.22 and Figure 4.23. The images are a side view of the structure for a better view of the droplet generating mechanism. See Figure 4.18(a) for the entire structure. The larger channel to the far left is made to simulate the connection with the silicon tube that was used for evaluating the droplet sizes in the experiment in Section 4.8.1. PVA is denoted as red and grape seed oil is denoted as blue, while grey is the interface between the two phases. There is contact between the channel surface and grape seed oil when blue can be observed in the image.

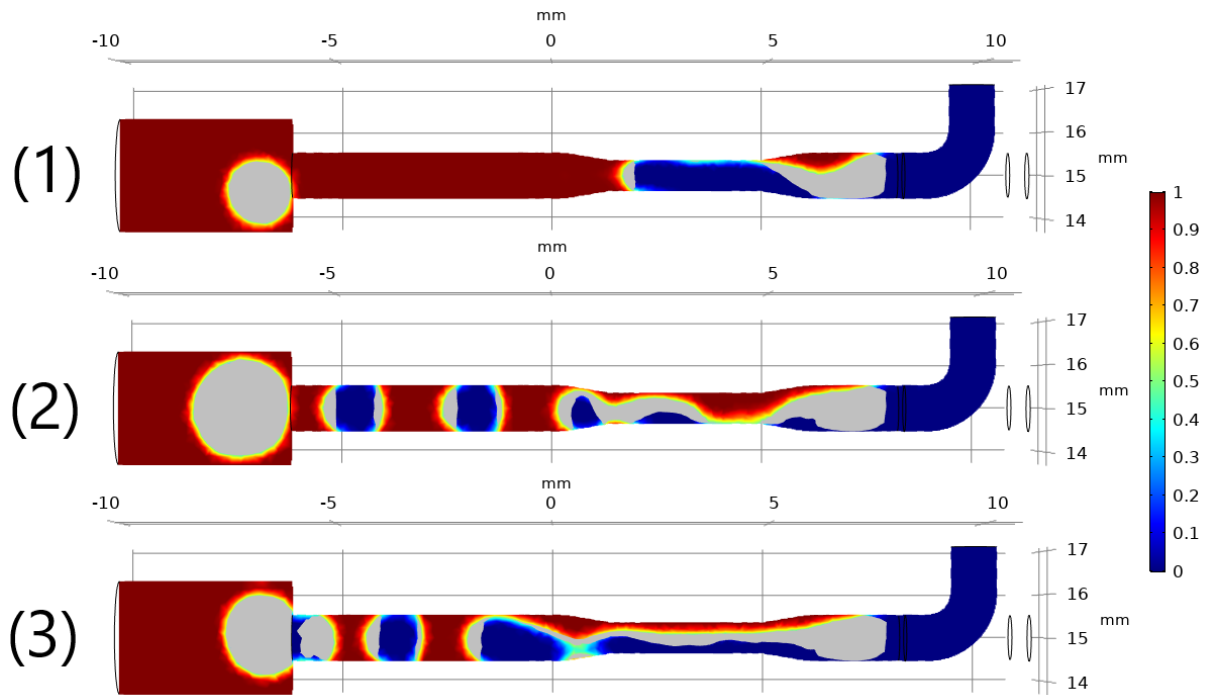


Figure 4.22: Simulation of a droplet generator with a MFS of 0.7 mm using 8% PVA as the continuous phase and grape seed oil and the dispersed phase.  $Q_{PVA} = 200 \frac{\mu\text{l}}{\text{min}}$ . (1):  $Q_{\text{Grapeseedoil}} = 20 \frac{\mu\text{l}}{\text{min}}$ . (2):  $Q_{\text{Grapeseedoil}} = 70 \frac{\mu\text{l}}{\text{min}}$ . (3):  $Q_{\text{Grapeseedoil}} = 120 \frac{\mu\text{l}}{\text{min}}$ .

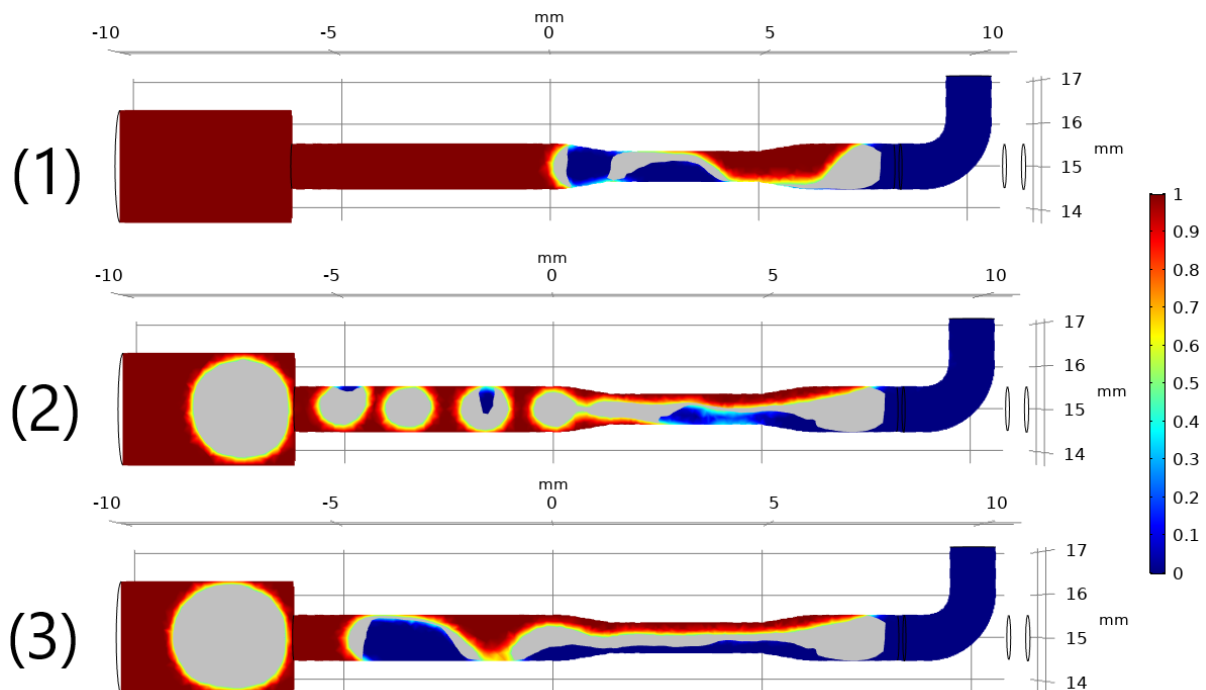


Figure 4.23: Simulation of a droplet generator with a MFS of 0.7 mm using 14% PVA as the continuous phase and grape seed oil and the dispersed phase.  $Q_{PVA} = 200 \frac{\mu\text{l}}{\text{min}}$ . (1):  $Q_{\text{Grapeseedoil}} = 20 \frac{\mu\text{l}}{\text{min}}$ . (2):  $Q_{\text{Grapeseedoil}} = 70 \frac{\mu\text{l}}{\text{min}}$ . (3):  $Q_{\text{Grapeseedoil}} = 120 \frac{\mu\text{l}}{\text{min}}$ .

Figure 4.22 is the simulation of droplets of grape seed oil in 8% PVA generated using a droplet generator with a MFS of 0.7 mm. The oil phase appears to cling to the bottom of the channel giving rise to only partially recognizable droplet formation mechanisms. The results partially resembles what is observed in Figure 4.21(a,b,c) which is dripping/squeezing and jet widening. Increasing the PVA concentration to 14% in Figure 4.23 only partly resembles the experimental results seen in Figure 4.21(d,e,f). The expected result of  $20 \frac{\mu\text{l}}{\text{min}}$  grape seed oil is dripping, but the simulated result is squeezing. The simulated result of  $70 \frac{\mu\text{l}}{\text{min}}$  grape seed oil is jet narrowing which matches the experimental result, but is still in contact with the bottom of the channel. The expected result of  $120 \frac{\mu\text{l}}{\text{min}}$  grape seed oil is an extended jet, but the simulated result resembles jet widening that is in contact with the bottom channel.

Simulations with 8% PVA and 14% PVA in a droplet generator with a MFS of 0.4 mm using  $Q_{PVA} = 200 \frac{\mu\text{l}}{\text{min}}$ , and  $Q_{Grapeseedoil} = 50 \frac{\mu\text{l}}{\text{min}}$  and a mesh consisting of 112258 elements with a MEQ of 0.2399 was made to see if the issue persisted. The oil flow did not stick to the side of the channel, see Figure 4.24. This indicates that the issue may be mesh resolution, since the mesh is adapted when the structure size changes. Two simulations using more meshing elements were made, see Figure 4.25. The simulations was made with a MFS of 0.7 mm, 8% PVA,  $Q_{PVA} = 200 \frac{\mu\text{l}}{\text{min}}$ , and  $Q_{Grapeseedoil} = [20, 120] \frac{\mu\text{l}}{\text{min}}$ . The number of meshing elements was increased from 54625 with a MEQ of 0.2361 to 671311 meshing elements with a MEQ of 0.1766.

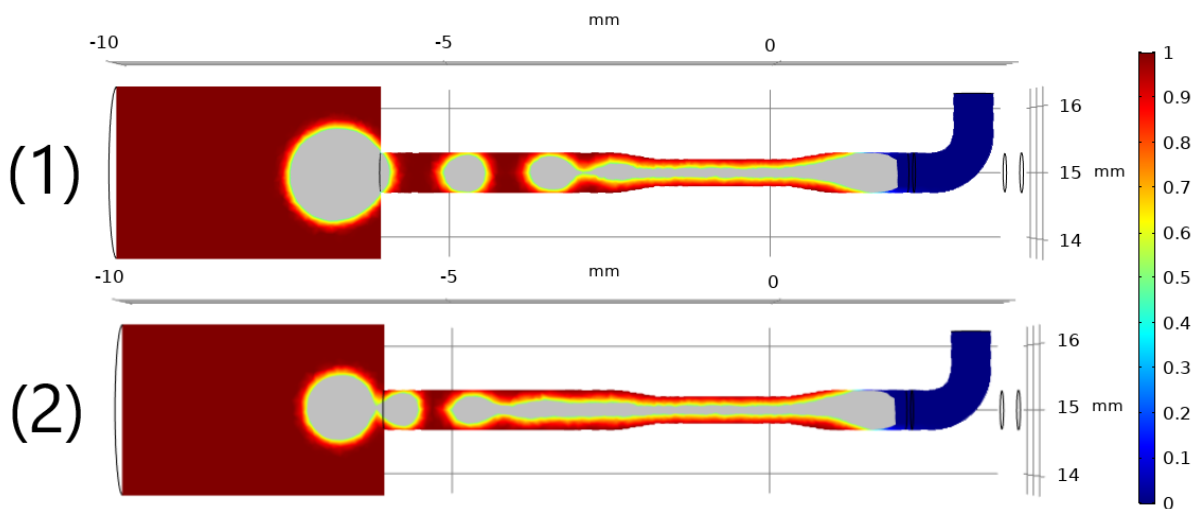


Figure 4.24: Simulation of a droplet generator with a MFS of 0.4 mm using  $Q_{PVA} = 200 \frac{\mu\text{l}}{\text{min}}$  and  $Q_{Grapeseedoil} = 50 \frac{\mu\text{l}}{\text{min}}$ . (1): 8% PVA, (2): 14% PVA.

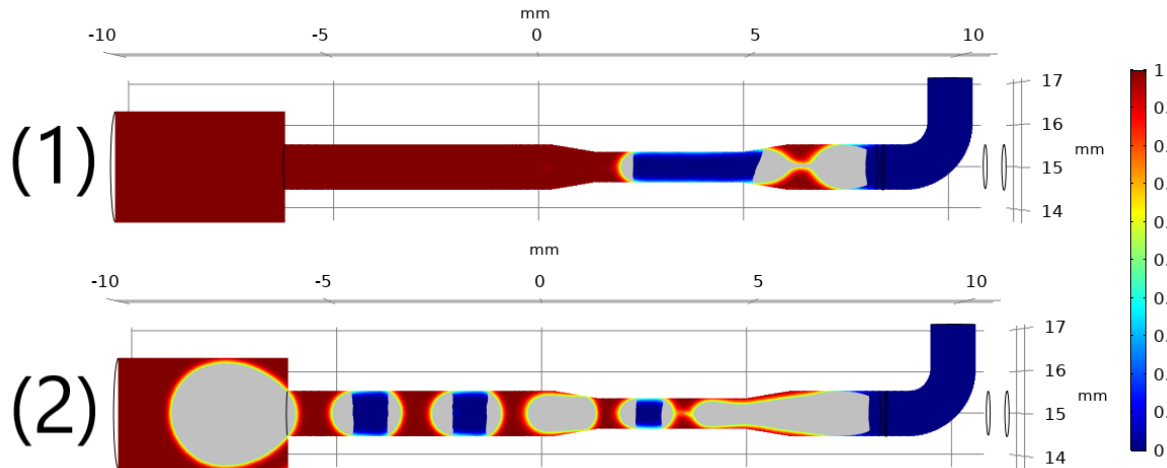


Figure 4.25: Simulation of a droplet generator with a MFS of 0.7 mm using 8% PVA as the continuous phase and grape seed oil and the dispersed phase.  $Q_{PVA} = 200 \frac{\mu\text{l}}{\text{min}}$  and (1):  $Q_{\text{Grapeseedoil}} = 20 \frac{\mu\text{l}}{\text{min}}$ , (2):  $Q_{\text{Grapeseedoil}} = 120 \frac{\mu\text{l}}{\text{min}}$ .

The issue of contact with the lower channel surface is gone, but the simulations still does not match the experimental result seen in Figure 4.21(a,c). The expected result for  $Q_{\text{Grapeseedoil}} = 20 \frac{\mu\text{l}}{\text{min}}$  is squeezing/dripping for 8% PVA, but the simulated result is squeezing. The expected result of  $Q_{\text{Grapeseedoil}} = 120 \frac{\mu\text{l}}{\text{min}}$  is jet widening for 8%, but the simulated result is squeezing/dripping.

Given the mismatch between the simulated results and the experimental results, further investigation of meshing and the user specified values is required before the simulations can be used for investigating the effects of altering variables such as viscosity, interfacial tension, and flow rates.

## 4.9 Electrospinning

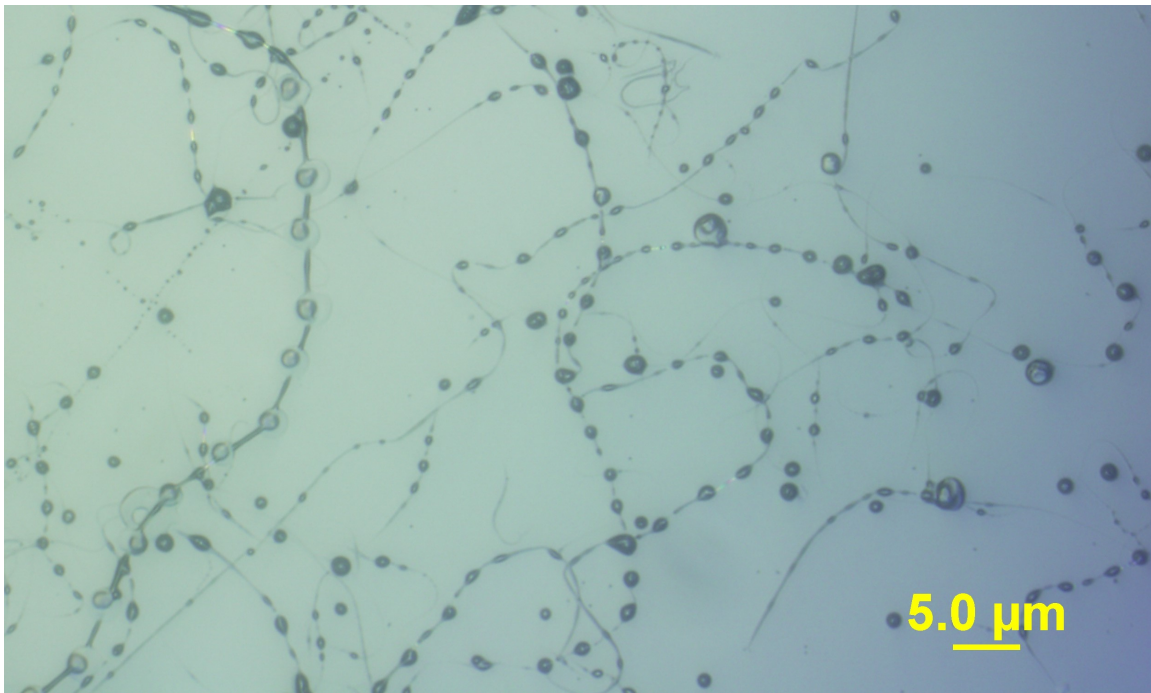
The droplet generator was connected to an electrospinning setup to continuously generate droplets into the flow of plastic being electrospun. The combination will allow for automated generation of emulsions removing the need for preparing emulsified solutions beforehand that may take longer to produce and with less monodisperse droplets [81, 82]. Thus, incorporating a droplet generator into the electrospinning setup can allow for faster and automated production of emulsion fibers. The expected result is droplets situated

inside the resulting fibers, as the droplets will be pulled along with the fiber during spinning, see Figure 2.5(a).

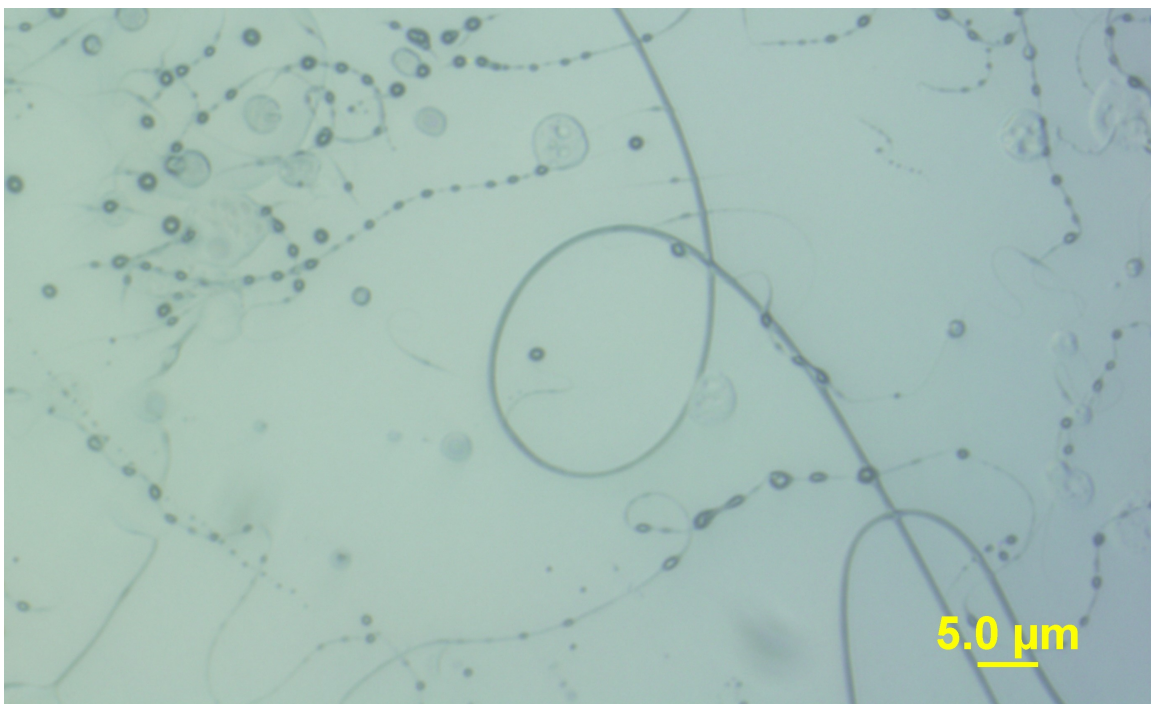
A series of electrospinning experiments were run with varying droplet generator MFSs, PVA concentrations, and oil flows to investigate the effect of these variables on the fiber and droplet diameters. A stable flow of droplets at the spinneret tip was ensured before initiating spinning. The flow (50  $\mu\text{l}/\text{min}$  PVA and 10-20  $\mu\text{l}/\text{min}$  grape seed oil) was kept intentionally too high, as the droplets would otherwise merge before reaching the spinneret tip. This had the side effect of breaking the spinning every time the droplet at the spinneret tip became too large and fell off. Initial tests using PCL in DCM with water droplets proved possible yet difficult as the water droplets would be ejected from the stream during spinning. Changing to PVA and grape seed oil removed this issue possibly because of the slight conductivity of grape seed oil due to its content of free fatty acids.

Four examples of the resulting PVA fibers with grape seed oil droplets in the beads on a string formation can be seen in Figure 4.26 and Figure 4.27. The fibers and droplets in Figure 4.26(a) are made with 8% PVA and 10  $\frac{\mu\text{l}}{\text{min}}$  grape seed oil. The fibers are overall thinner than the droplets, but what appears to be droplets with a diameter similar to the fiber diameter can be observed. The same trend is observed with 10% PVA and 10  $\frac{\mu\text{l}}{\text{min}}$  grape seed oil as seen in Figure 4.26(b). Increasing the PVA concentration to 14% with or without SDS, results in more uniform fibers with droplets equal to the fiber diameter, as seen in Figure 4.27(a,b).

The average fiber diameter and droplet diameter of the samples for each combination of settings can be seen in Table 4.13. The fiber diameters are evaluated by taking the cross section of the fibers. The droplets are assumed to be the dark circles/orbs in the fibers, as fibers produced from only PVA does not create these structures, see Figure 7.4 in Appendix C. The droplet diameters are evaluated in their narrow region in cases of oval droplets.

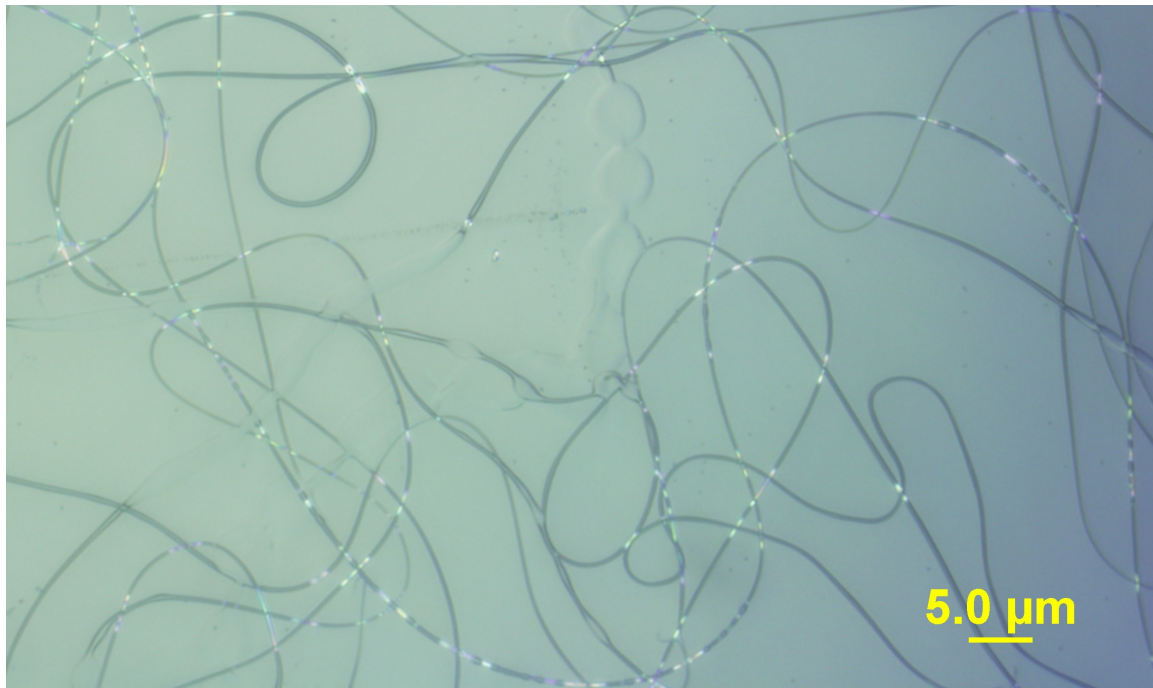


(a)

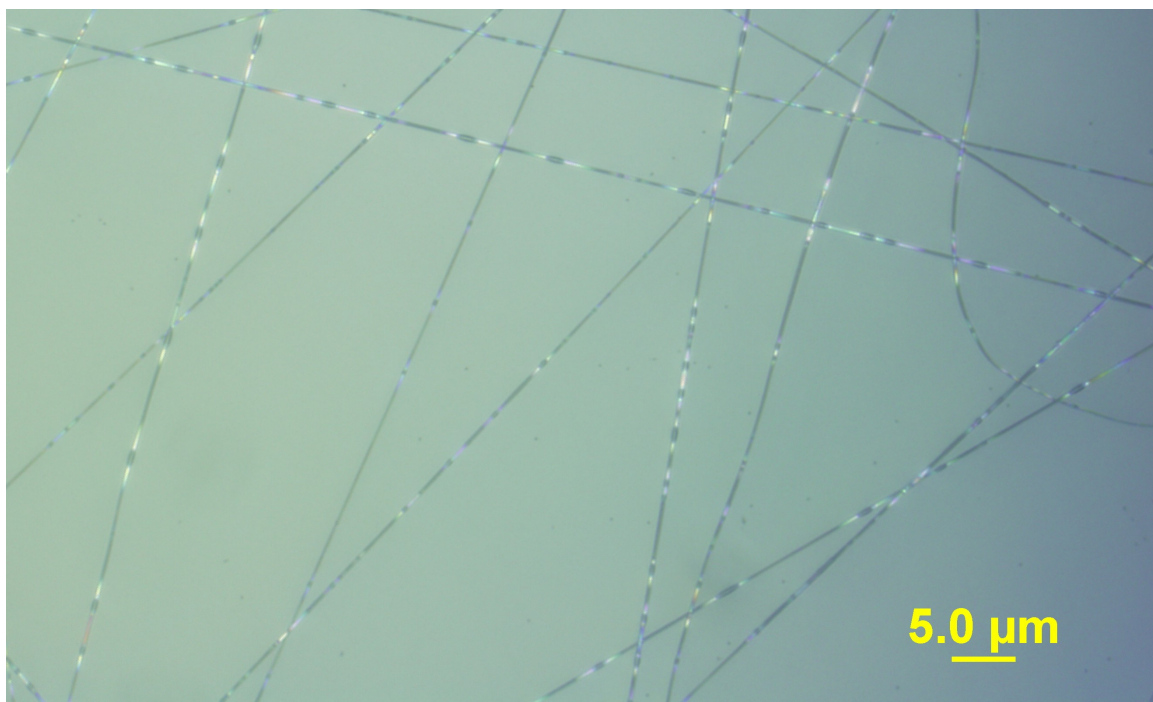


(b)

Figure 4.26: (a): Fibers with droplets spun at 17-18 kV using 50  $\mu\text{l}/\text{min}$  8% PVA and 10  $\mu\text{l}/\text{min}$  grapeseed oil through a droplet generator with a 0.7 mm MFS. (b): Fibers with droplets spun at 17-18 kV using 50  $\mu\text{l}/\text{min}$  10% PVA and 10  $\mu\text{l}/\text{min}$  grapeseed oil through a droplet generator with a 0.6 mm MFS.



(a)



(b)

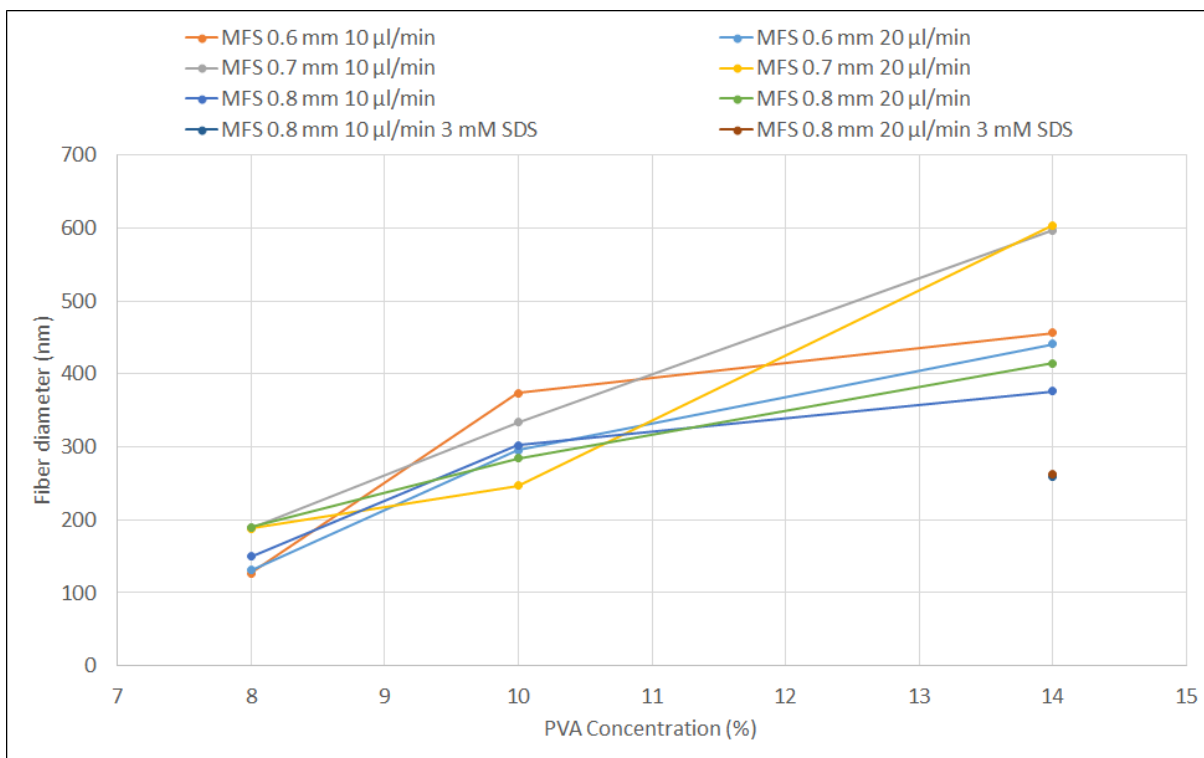
Figure 4.27: (a): Fibers with droplets spun at 17-18 kV using 50  $\mu\text{l}/\text{min}$  14% PVA and 10  $\mu\text{l}/\text{min}$  grapeseed oil through a droplet generator with a 0.7 mm MFS. (b): Fibers with droplets spun at 17-18 kV using 50  $\mu\text{l}/\text{min}$  14% PVA with 3 mM SDS and 10  $\mu\text{l}/\text{min}$  grapeseed oil through a droplet generator with a 0.7 mm MFS.

Table 4.13: Fiber and droplet diameters from electrospinning droplet generated emulsions at 17-18 kV. The flow of PVA was kept at a constant 50  $\mu\text{l}/\text{min}$ .

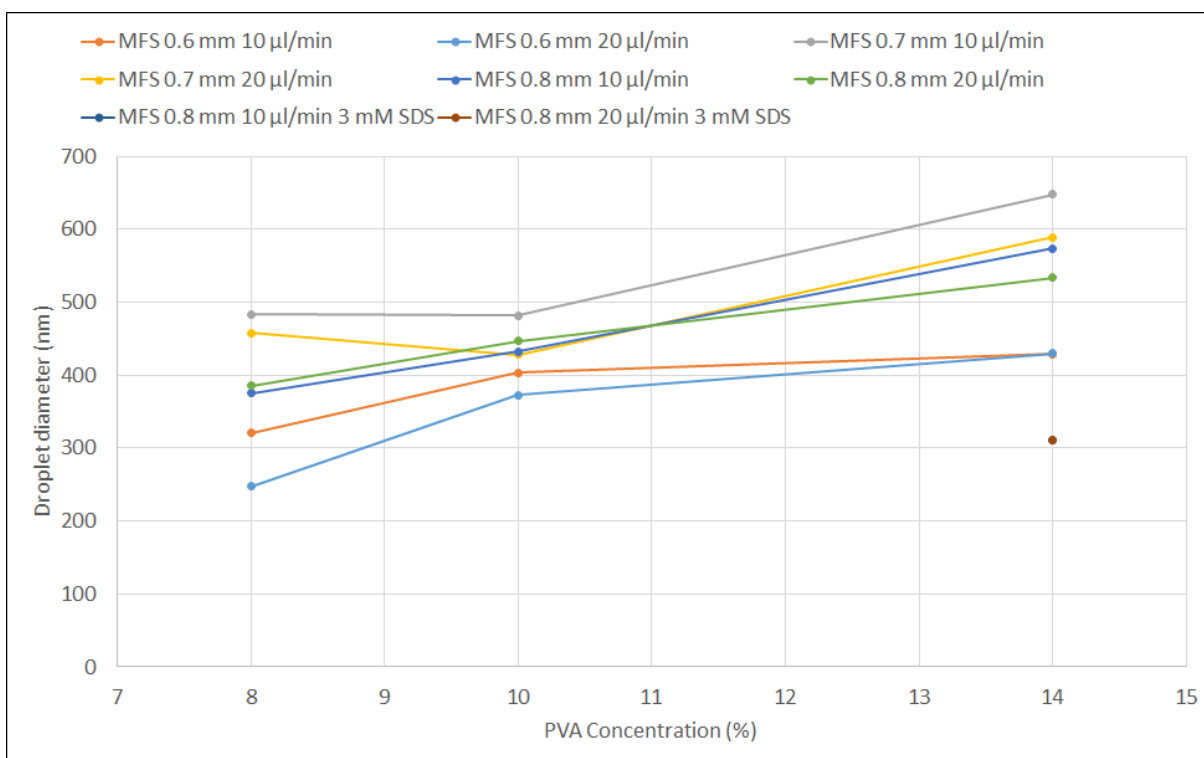
MFS mm	PVA [%]	Oil V [ $\mu\text{l}/\text{min}$ ]	SDS [mM]	$D_{fiber}$ [nm]	Std. [nm]	$D_{droplet}$ [nm]	Std. [nm]
0.6	8	10	0	127	43	321	71
0.6	8	20	0	131	40	247	70
0.7	8	10	0	189	52	483	144
0.7	8	20	0	188	43	458	122
0.8	8	10	0	150	33	375	96
0.8	8	20	0	190	35	385	158
0.6	10	10	0	374	111	403	93
0.6	10	20	0	295	82	373	104
0.7	10	10	0	334	62	482	113
0.7	10	20	0	247	45	428	76
0.8	10	10	0	302	73	432	71
0.8	10	20	0	284	58	447	90
0.6	14	10	0	456	62	429	98
0.6	14	20	0	441	82	430	69
0.7	14	10	0	597	142	648	149
0.7	14	20	0	604	257	589	138
0.8	14	10	0	376	129	574	170
0.8	14	20	0	415	89	534	108
0.8	14	10	3	260	70	310	62
0.8	14	20	3	263	74	310	53

Table 4.13 shows the fiber and droplet diameters from electrospinning droplet generated emulsions of grape seed oil in PVA. The standard deviation is an indication of how uniform the resulting fibers and droplets were for the given settings.

The correlation between the tested parameters and the fiber/droplet diameters were investigated by plotting fiber/droplet diameter against the parameters. The results can be seen in Figure 4.28, Figure 4.29, and Figure 4.30.

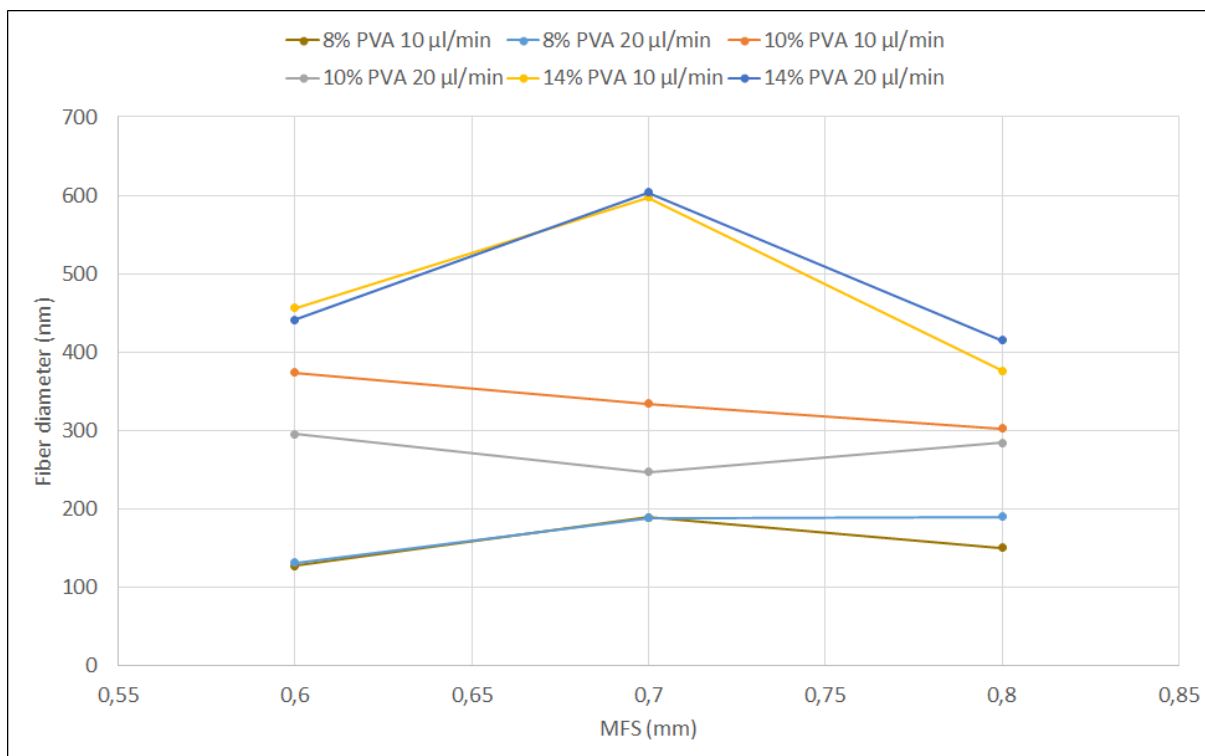


(a)

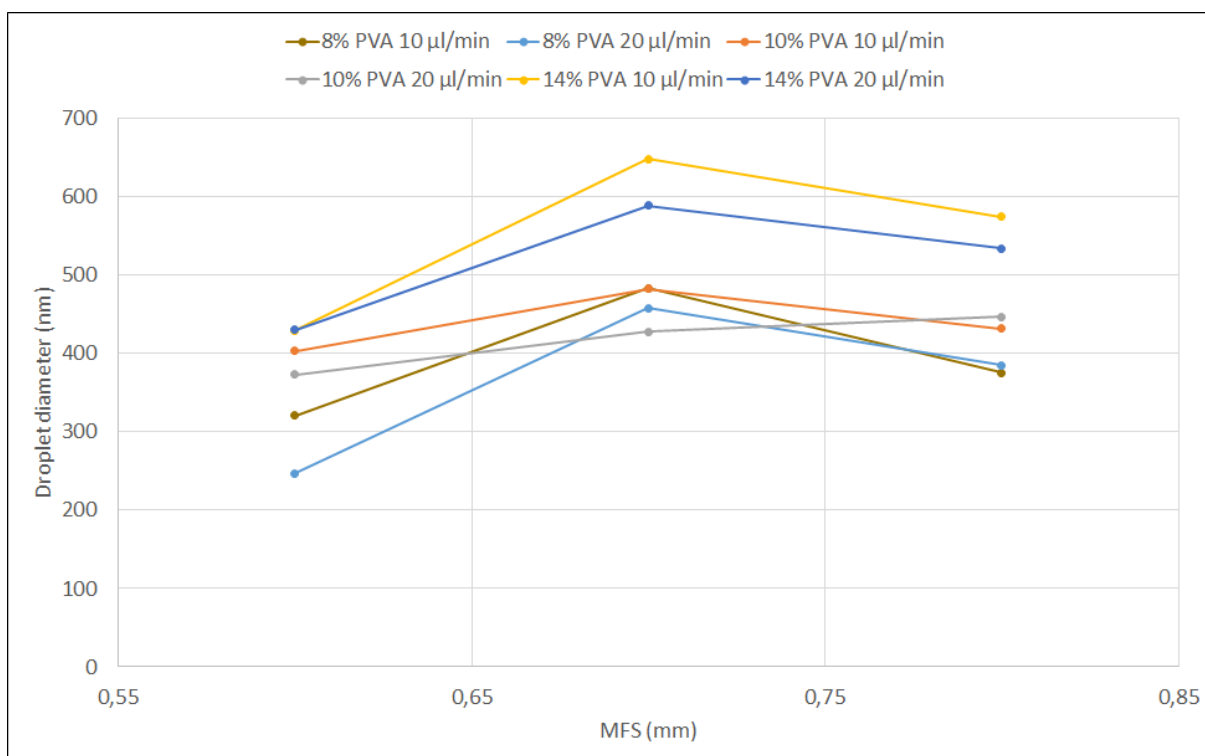


(b)

Figure 4.28: (a): Plot of diameter of fibers electrospun from emulsions of grape seed oil in different concentrations of PVA generated using droplet generators. (b): Plot of diameter of droplets in fibers electrospun from emulsions of grape seed oil in different concentrations of PVA generated using droplet generators.

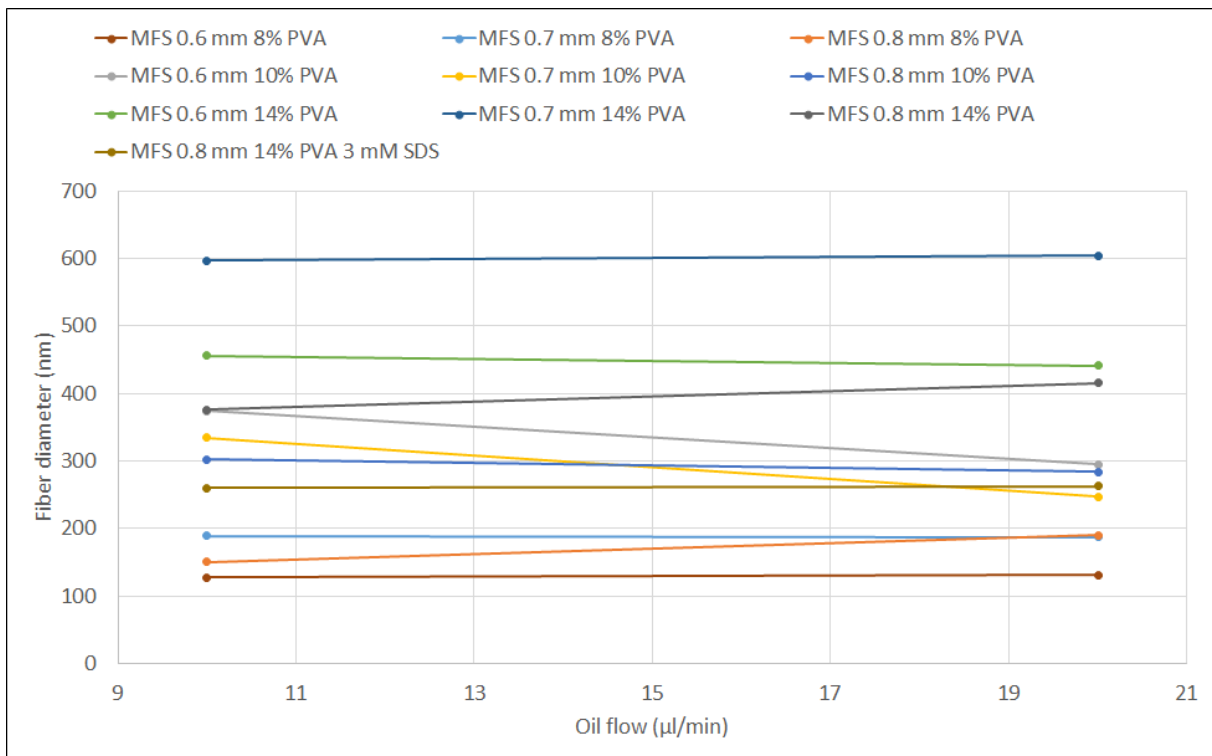


(a)

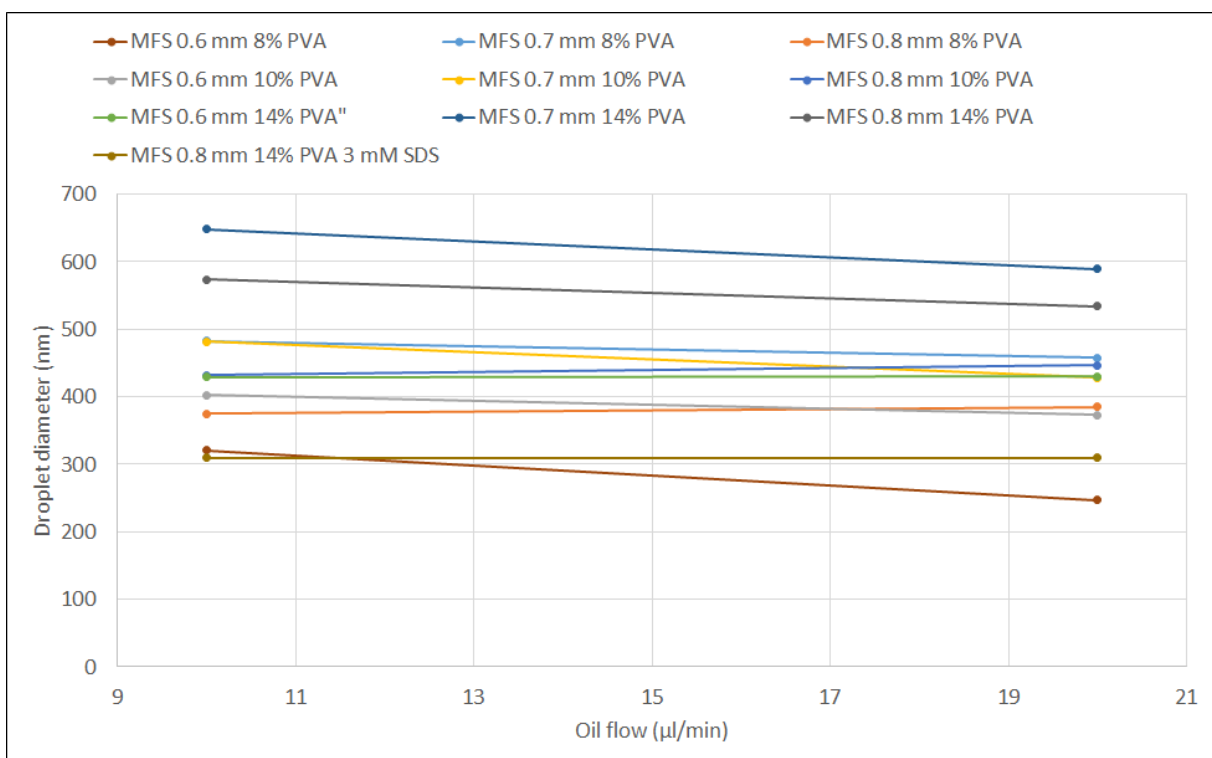


(b)

Figure 4.29: (a): Plot of diameter of fibers electrospun from emulsions of grape seed oil in PVA generated using droplet generators with a varying MFS. (b): Plot of diameter of droplets in fibers electrospun from emulsions of grape seed oil in PVA generated using droplet generators with a varying MFS.



(a)



(b)

Figure 4.30: (a): Plot of diameter of fibers electrospun from emulsions of grape seed oil in PVA generated using droplet generators with varying flows of grape seed oil. (b): Plot of diameter of droplets in fibers electrospun from emulsions of grape seed oil in PVA generated using droplet generators with varying flows of grape seed oil.

Figure 4.28(a) shows the diameter of the fibers electrospun from droplet generated grape seed oil emulsions in PVA. The fiber diameter increases with increasing PVA concentration for all samples, which shows that spinning droplets into the fibers does not change the expected correlation between fiber diameter and PVA concentration. Figure 4.29(a) shows the fiber diameter dependence on the MFS of the droplet generator. No clear tendency can be observed, which correlates with the expected non-correlation between the two variables. Figure 4.30(a) shows the fiber diameter dependence on the grape seed oil flow. No clear tendency is observed, indicating no correlation between the two variables.

Figure 4.28(b) shows the droplet diameter of droplets in fibers electrospun from grape seed oil emulsions in PVA made using droplet generators. Like the fiber diameter, the droplet diameter also increases as the PVA concentration increases. Figure 4.20 shows that a higher PVA concentration generated smaller droplets, which is contradictory to what is observed for droplets in fibers. The upper limit of droplet diameters in fibers may be more dependent upon diameter of the fiber than the droplets in the emulsion used for spinning. However, Figure 4.20 shows that an increase in MFS correlates with an increase in droplet diameter, which when combined with Figure 4.29(b) shows that an increase in the generated droplet size results in larger droplets in the fiber. In short, higher PVA concentrations lead to larger fibers, which appears to stabilize larger droplets, but also causes the droplet generator to make smaller droplets, which can be counteracted by using a droplet generator with a larger MFS. Figure 4.30(b) shows the droplet diameter of droplets in fibers tend to decrease with an increased relative oil flow. The change in droplet diameter may be an artifact, as the supply of grape seed droplets in the PVA flow was already higher than necessary for 10  $\mu\text{l}/\text{min}$  grape seed oil.

Based on the results from the previous section the size of generated droplets are in the range of 300  $\mu\text{m}$  to 2500  $\mu\text{m}$ . Thus, the droplets are considerably larger than the droplets found in the PVA fibers which are in the range of 250 nm to 650 nm with the given setup and settings. To be electrospun into the beads on a string formation, the droplets must be broken down into smaller droplets during the spinning process. Based on observations of droplets situating themselves at the point of spinning we propose that a droplet generation occurs at the point of spinning, see Figure 4.31. A combination of polarization of the oil in the electric field pulling it upwards together with the encapsulating flow of PVA may

be what causes droplet generation during spinning. It forms a co-flow formation with focusing as the jet is thinned during spinning. H. Kim *et. al.* observed electrospaying of droplets from a Taylor cone of the dispersed phase inside a droplet generator when applying an electric field to the setup [83]. The same may be what causes the formation of smaller droplets inside the Taylor cone at the tip of the spinneret during electrospinning. Additionally, C. Yeh *et. al.* found that reducing the interfacial tension between the continuous phase and the dispersed phase reduces the droplet size during electrospaying of droplets [84]. This may explain why adding SDS to the PVA resulted in some of the smallest droplets in the fibers, as seen in Table 4.13. Imaging of the event site is required to confirm if droplet generation through electrospaying is the mechanism creating smaller droplets during electrospinning.

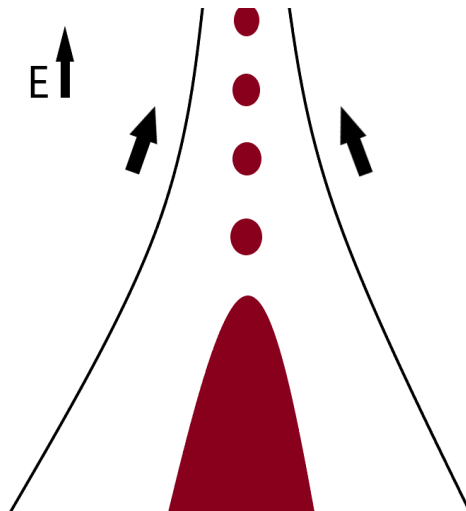


Figure 4.31: Proposed point for droplet formation in the Taylor cone during electrospinning.

---

## 5. Conclusion

---

Printing of microfluidic systems using the Anycubic Photon 3D DLP Printer proved to be possible and fast, but the minimum feature size is limited to 0.4x0.4 mm by the printer resolution and printing material. The surface roughness caused by the pixelation of the DLP creates both a discrepancy between simulation and experiments, and the need for surface treatments to make the prints transparent. The microfluidic systems are limited to fluids and solvents that do not damage the structure. Leaching of unknown chemicals from the 3D printed structures were confirmed, but needs additional testing to investigate the identity and possible malignancy of the leached compounds.

The microfluidic system, Worm Junction, designed for the use in chemotaxis experiments of *C. elegans* is theoretically usable, but has issues with bubbles, gravity induces flow fluctuations, and fluctuations of compound concentration in the water fraction. Testing with live *C. elegans* is required to validate and optimize the design for chemotaxis experiments.

Simulations of the gradient generator showed that a gradient with a low error percentage can be achieved, but 3D printing of the structure proved difficult due to cleaning of the parallel channel design. Use of the gradient generator proved to be time inefficient since clearing of bubbles was time consuming due to the parallel channel design. Simulations of the flow chamber showed it to be a promising microfluidic design for chemotaxis of *C. elegans* with a negligible disruption of the injected concentration gradient. Further printing and testing of the structure is required to evaluate the design for the use in chemotaxis experiments.

The droplet generator design was successful since the droplet size could be altered through the change in droplet generator channel size. Incorporating the droplet generator into the electrospinning setup resulted in continuous generation of emulsions into fibers. The size of the droplets in the fibers could be altered through the PVA concentration, the dispersed flow rate, and the minimum feature size of the droplet generator.

In summery the use of the Anycubic Photon DLP 3D printer for the use in rapid prototyping of microfluidic systems is possible and increases the testing speed of designs, but comes with its own set of challenges and limitations.

---

## 6. Future Implications

---

Printing and cleaning of complex channel designs like parallel channels proved to be difficult. Further investigation of alternative printing methods, e.g. splitting the design into parts for later recombining.

Reduction of channel surface roughness through injection of polishing material can be tested to reduce surface roughness induced flow issues.

Further experimentation with reduction of chemical leaching through methods such as ultrasonication, and further investigation of the identity of the unknown leached compounds.

Experimental testing of the chemotaxis microfluidic systems with *C. elegans* for further evaluation of the designs.

Further investigation of the user specified values for the droplet generator simulations such that they can be used for simulating the effect of various parameters.

Investigation of the effect of using droplet generators with smaller MFSs on the morphology of the electrospun emulsion fibers.

Investigation of the release profile of compounds from electrospun emulsion fibers to investigate the effect of electrospinning parameters on the release profile.

Investigation of the position of emulsions in the emulsion fibers through the addition of detectable compounds to the emulsions.



---

# Bibliography

---

- [1] Bharat Bhushan and Matt Caspers. An overview of additive manufacturing (3d printing) for microfabrication. *Microsystem Technologies*, 23:1117–1124, Apr 2017.
- [2] Tim Femmer, Alexander Jans, Rudi Eswein, Naveed Anwar, Martin Moeller, Matthias Wessling, and Alexander J.C. Kuehne. High-throughput generation of emulsions and microgels in parallelized microfluidic drop-makers prepared by rapid prototyping. *ACS Applied Materials & Interfaces*, 7(23):12635–12638, 2015.
- [3] Mark B. Romanowsky, Adam R. Abate, Assaf Rotem, Christian Holtze, and David A. Weitz. High throughput production of single core double emulsions in a parallelized microfluidic device. *Lab Chip*, 12:802–807, 2012.
- [4] Gregory P. Nordin et al. 3d printing for lab-on-a-chip devices with 20  $\mu\text{m}$  channels. *Proceedings of Spie*, 10932, 2019.
- [5] Chengpeng Chen, Benjamin T. Mehl, Akash S. Munshi, Alexandra D. Townsend, Dana M. Spence, and R. Scott Martin. 3d-printed microfluidic devices: fabrication, advantages and limitations—a mini review. *Anal. Methods*, 8:6005–6012, 2016.
- [6] Kyoung G. Lee, Kyun Joo Park, Seunghwan Seok, Sujeong Shin, Do Hyun Kim, Jung Youn Park, Yun Seok Heo, Seok Jae Lee, and Tae Jae Lee. 3d printed modules for integrated microfluidic devices. *RSC Adv.*, 4:32876–32880, 2014.
- [7] Kari B. Anderson, Sarah Y. Lockwood, R. Scott Martin, and Dana M. Spence. A 3d printed fluidic device that enables integrated features. *Analytical Chemistry*, 85(12):5622–5626, 2013.
- [8] Ho Nam Chan, Yiwei Shu, Bin Xiong, Yangfan Chen, Yin Chen, Qian Tian, Sean A. Michael, Bo Shen, and Hongkai Wu. Simple, cost-effective 3d printed microfluidic components for disposable, point-of-care colorimetric analysis. *ACS Sensors*, 1(3):227–234, 2016.

- 
- [9] William G. Patrick, Alec A. K. Nielsen, Steven J. Keating, Taylor J. Levy, Che-Wei Wang, Jaime J. Rivera, Octavio Mondragón-Palomino, Peter A. Carr, Christopher A. Voigt, Neri Oxman, and David S. Kong. Dna assembly in 3d printed fluidics. *PLOS ONE*, 10(12):1–18, 2016.
- [10] Alex J. L. Morgan, San J. Lorena Hidalgo, William D. Jamieson, Jennifer M. Wymant, Bing Song, Phil Stephens, David A. Barrow, and Oliver K. Castell. Simple and versatile 3d printed microfluidics using fused filament fabrication. *PLoS One*, 11(4), 2016.
- [11] Aliaa I. Shallan, Petr Smejkal, Monika Corban, Rosanne M. Guijt, and Michael C. Breadmore. Cost-effective three-dimensional printing of visibly transparent microchips within minutes. *Analytical Chemistry*, 86(6):3124–3130, 2014.
- [12] Chad I. Rogers. et. al. 3d printed microfluidic devices with integrated valves. *Biomicrofluidics*, 9(1), 2015.
- [13] Hua Gong, Adam T. Woolley, and Gregory P. Nordin. High density 3d printed microfluidic valves pumps and multiplexers. *Lab Chip*, 16:2450–2458, 2016.
- [14] Hua Gong, Michael Beauchamp, Steven Perry, Adam T. Woolley, and Gregory P. Nordin. Optical approach to resin formulation for 3d printed microfluidics. *RSC Adv.*, 5:106621–106632, 2015.
- [15] Tuan D. Ngo, Alireza Kashani, Gabriele Imbalzano, Kate T.Q. Nguyen, and David Hui. Additive manufacturing (3d printing): A review of materials, methods, applications and challenges. *Composites Part B: Engineering*, 143:172 – 196, 2018.
- [16] Yayue Pan, Chi Zhou, and Yong Chen. A Fast Mask Projection Stereolithography Process for Fabricating Digital Models in Minutes. *Journal of Manufacturing Science and Engineering*, 134(5):1 – 2, 09 2012.
- [17] Xiaoyu Zheng, Joshua Deotte, Matthew P. Alonso, George R. Farquar, Todd H. Weisgraber, Steven Gemberling, Howon Lee, Nicholas Fang, and Christopher M. Spadaccini. Design and optimization of a light-emitting diode projection micro-stereolithography three-dimensional manufacturing system. *Review of Scientific Instruments*, 83(12), 2012.
-

- [18] C. Sun, N. Fang, D.M. Wu, and X. Zhang. Projection micro-stereolithography using digital micro-mirror dynamic mask. *Sensors and Actuators A: Physical*, 121(1):113 – 115, 2005.
- [19] Hossam Kadry et. al. Digital light processing (dlp) 3d-printing technology and photoreactive polymers in fabrication of modified-release tablets. *European Journal of Pharmaceutical Sciences*, 135:60 – 67, 2019.
- [20] Ferry P.W. Melchels, Jan Feijen, and Dirk W. Grijpma. A review on stereolithography and its applications in biomedical engineering. *Biomaterials*, 31(24):6121 – 6130, 2010.
- [21] R. Scott et. al. 3d-printed microfluidic devices: fabrication, advantages and limitations—a mini review. *Anal. Methods*, 8:6005–6012, 2016.
- [22] Michael J. Beauchamp, Gregory P. Nordin, and Adam T. Woolley. Moving from millifluidic to truly microfluidic sub-100- $\mu\text{m}$  cross-section 3d printed devices. *Analytical and Bioanalytical Chemistry*, 409:4311–4319, 2017.
- [23] Hua Gong, Bryce P. Bickham, Adam T. Woolley, and Gregory P. Nordin. Custom 3d printer and resin for 18  $\mu\text{m}$   $\times$  20  $\mu\text{m}$  microfluidic flow channels. *Lab Chip*, 17:2899–2909, 2017.
- [24] Megan Carve and Donalds Wlodkovic. 3d-printed chips: Compatibility of additive manufacturing photopolymeric substrate with biological applications. *Micromachines*, 9, 2018.
- [25] Shyam Dev Maurya, S. K. Kurmvanshi, S. Mohanty, and Sanjay K. Nayak. A review on acrylate-terminated urethane oligomers and polymers: Synthesis and applications. *Polymer-Plastics Technology and Engineering*, 57(7):625–656, 2018.
- [26] V. S. D. Voet et. al. Biobased acrylate photocurable resin formulation for stereolithography 3d printing. *ACS Omega*, 3:1403–1408, 2018.
- [27] B. Huang et al. Preparation of a novel hybrid type photosensitive resin for stereolithography in 3d printing and testing on the accuracy of the fabricated parts. *Journal of Wuhan University of Technology-mater. sci. ed.*, 32, 2017.

- [28] Marco Sangermano, William Carbonaro, Giulio Malucelli, and Aldo Priola. Uv-cured interpenetrating acrylic-epoxy polymer networks: Preparation and characterization. *Macromolecular Materials and Engineering*, 293(6):515–520, 2008.
- [29] S. Lantean et al. Development of new hybrid acrylic/epoxy dlp-3d printable materials. *inventions*, 3:13, 2018.
- [30] Jing Zhang, Pu Xiao, Celine Dietlin, Damien Campolo, Frederic Dumur, Didier Gigmes, Fabrice Morlet-Savary, Jean-Pierre Fouassier, and Jacques Lalevée. Cationic photoinitiators for near uv and visible leds: A particular insight into one-component systems. *Macromolecular Chemistry and Physics*, 217(11):1214–1227, 2016.
- [31] D. B. Short et. al. 3d printing (rapid pprototyping) photopolymers: An emerging source of antimony to the environment. *3D Printing*, 1(1):24–33, 2014.
- [32] W. Geurtsen. Biocompatibility of resin-modified filling materials. *Crit. Rev. Oral Biol. Med.*, pages 333–355, 2000.
- [33] Mehmet Ata Cebe, Fatma Cebe, Mehmet Fatih Cengiz, Ali Rıza Cetin, Osman Fatih Arpag, and Bora Ozturk. Elution of monomer from different bulk fill dental composite resins. *Dental Materials*, 31(7):141 – 149, 2015.
- [34] Thaiane R. Aguiar, Michele [de Oliveira], César A.G. Arrais, Glaucia M.B. Ambrosano, Frederick Rueggeberg, and Marcelo Giannini. The effect of photopolymerization on the degree of conversion, polymerization kinetic, biaxial flexure strength, and modulus of self-adhesive resin cements. *The Journal of Prosthetic Dentistry*, 113(2):128 – 134, 2015.
- [35] D. Arenholdt-Bindslev G. Schmalz. *Biocompatibility of Dental Materials*. Springer: Germany, 2009.
- [36] S M Oskui et. al. Assessing and reducing the toxicity of 3d-printed parts. *Environmental letters*, pages 1–6, 2016.
- [37] B. Behkam M. Aziz Traore. A peg-da microfluidic device for chemotaxis studies. *J. Micromech. Microeng.*, page 9, 2013.

- [38] N. M. Fuad et. al. Characterization of 3d-printed moulds for soft lithography of millifluidic devices. *Micromachines*, 9(116):59–69, 2018.
- [39] COMSOL. *COMSOL Multiphysics - Reference Manual*. Version 5.5, 2019.
- [40] Strogatz Steven H. Watts, Duncan J. Collective dynamics of ‘small-world’ networks. *Nature*, 393(6684):440–442, Jun 1998.
- [41] M. Zaremba R.A. Kosinski. Dynamics of the model of the caenorhabditis elegans neural network. *Acta Physica Polonica B*, 38(6):2201, April 2007.
- [42] G. Tsechpenakis et. al. A novel computational approach for simultaneous tracking and feature extraction of *C. elegans* populations in fluid environments. *IEEE Transaction on biomedical engineering*, 55(5):1539–1549, 2008.
- [43] C. I. Bargmann. Chemosensation in c. elegans. *WormBook Online Review*, 2006.
- [44] Hobert Oliver Remy, J-Jean. An interneuronal chemoreceptor required for olfactory imprinting in c. elegans. *Science*, 309(5735):787–790, Jul 2005.
- [45] H. J. Cho A. Karbalaei. Microfluidic devices developed for and inspired by thermotaxis and chemotaxis. *Micromachines*, 9(4):28, 2018.
- [46] I. N. Maruyama T. Murayama. Plate assay to determine caenorhabditis elegans response to water soluble and volatile chemicals. *Bio-protocol*, 8(4), 2018.
- [47] I. ChinSang O. Margie, C. Palmer. C. elegans chemotaxis assay. *J. Vis. exp*, 74(e50069):6, 2013.
- [48] S. H. Kim S. Park H. Hwang, E. Kim. A sensitive c. elegans chemotaxis assay using microfluidic device generating a linear gradient of chemoeffectors. *Bull. Korean Chem. Soc.*, 36:1096–1099, 2015.
- [49] C. Bargmann N. Chronis, M. Zimmer. Microfluidic for in vivo imaging of neuronal and behavioral activity in caenorhabditis elegans. *Nature methods*, 4(9):727–731, 2007.
- [50] W. Du B. Liu J. Wang, X. Genf. Microfluidic worm-chip for in vivo analysis of neuronal activity upon dynamic chemical stimulations. *Ana. Chi. Acta*, 701:23–28, 2011.

- 
- [51] Jiajia Xue et. al. Electrospinning and electrospin nanofibers: methods, materials, and applications. *Chemical reviews*, 119(8):5298–5415, 2019.
- [52] M.M. Demir et. al. Electrospinning of polyurethane fibers. *Polymer*, 43:3303–3309, 2002.
- [53] Juanping Hu et. al. One-step electro-spinning/netting technique for controllably preparing polyurethane nano-fibers/net. *Macromolecular journals*, 32:1729–1734, 2011.
- [54] C. J. Luo et. al. Mapping the influence of solubility and dielectric constant on electrospinning polycaprolactone solutions. *Macromolecules*, 45:4669–4680, 2012.
- [55] C. J. Angamma et. al. A modified electrospinning method for conductive and insulating materials. *Proc. ESA Annual Meetong on electrostatics*, L3, 2010.
- [56] C. J. Angamma et. al. Analysis of the effects of solution conductivity on electrospinning process and fiber morphology. *IEEE Trans. Ind. Appl.*, 47:1109–1117, 2011.
- [57] N. A. M. Barakat et. al. Spider-net within the n6, pva and pu electrospun nanofiber mats using salt addition: Novel strategy in the electrospinning process. *Polymer*, 50:4389–4396, 2009.
- [58] X. Wang et. al. Large-scale fabrication of two-dimensional spider-web-like gelatin nano-nets via electro-netting. *Colloids and Surfaces B: Biointerfaces*, 86:345–352, 2011.
- [59] G. Yang et. al. Influence of working temperature on the formation of electrospun polymer nanofibers. *Nanoscale research letters*, 12(55), 2017.
- [60] C.J. Thompson et. al. Effects of parameters on nanofiber diameter determined from electrospinning model. *Polymer*, 48, 2007.
- [61] D. S. Katti et. al. Bioresorbable nanofiber-based systems for wound healing and drug delivery: Optimization of fabrication parameter. *Journal of Biomedical Materials Research*, 70:286–296, 2004.

- [62] W. E. King III et. al. Characterization of polydioxanone in near-field electrospinning. *Polymers*, 12, 2019.
- [63] H. Qi et. al. Encapsulation of drug reservoirs in fibers by emulsion electrospinning: Morphology characterization and preliminary release assessment. *Biomacromolecules*, 7, 2006.
- [64] Y. Jin et. al. Fabrication of necklace-like structure via electrospinning. *Langmuir*, 26, 2010.
- [65] D. Crespy et. al. Colloid-electrospinning: Fabrication of multicompart ment nanofibers by the electrospinning of organic or/and inorganic dispersions and emulsions. *Macromol. Rapid commun.*, 33, 2012.
- [66] W. Yuan et. al. Structural evolution of electrospun composite fibers from the blend of polyvinyl alcohol and polymer nanoparticles. *Langmuir*, 28, 2012.
- [67] Bernat Esteban, Jordi-Roger Riba, Grau Baquero, Antoni Rius, and Rita Puig. Temperature dependence of density and viscosity of vegetable oils. *Biomass and Bioenergy*, 42:167, 2012.
- [68] Lemuel M. Diamante and Tianying Lan. Absolute viscosities of vegetable oils at different temperatures and shear rate range of 64.5 to 4835  $s^{-1}$ . *Journal of Food Processing*, 2014:4, 08 2014.
- [69] Mohsen Mohsen-Nia and Hamid Modarress. Viscometric study of aqueous poly(vinyl alcohol) (pva) solutions as a binder in adhesive formulations. *Journal of Adhesion Science and Technology*, 20(12):1278–1279, 2006.
- [70] Ashkan Babaie, S. Madadkhani, and Boris Stoeber. Evaporation-driven low reynolds number vortices in a cavity. *Physics of Fluids (1994-present)*, 26:5, 03 2014.
- [71] C G Y Ngan et. a. Optimising the biocompatibility of 3d printed photopolymer constructs *in vitro* and *in vivo*. *Biomedical Materials*, 14, 2019.
- [72] J. M. P. Q. Delgado. Molecular diffusion coefficients of organic compounds in water at different temperatures. *Jour. of Phase Equil. and Diff.*, 28(5):427–432, 2007.

- [73] P. Schwille Z. Petrášek. Precise measurement of diffusion coefficients using scanning fluorescence correlation spectroscopy. *Biophysics Journal*, 94:1437–1448, 2008.
- [74] Ryungeun Song, Muhammad Salman Abbasi, and Jinkee Lee. Fabrication of 3d printed modular microfluidic system for generating and manipulating complex emulsion droplets. *Microfluidics and Nanofluidics*, 23(7):92, Jun 2019.
- [75] Aliaa I. Shallan, Petr Smejkal, Monika Corban, Rosanne M. Guijt, and Michael C. Breadmore. Cost-effective three-dimensional printing of visibly transparent microchips within minutes. *Analytical Chemistry*, 86(6):3124–3130, 2014.
- [76] P. Wu et. al. Drag-induced breakup mechanism for droplet generation in dripping within flow focusing microfluidics. *Chinese Jour. of Chem. Eng.*, pages 7–14, 2015.
- [77] L. Wang P. Zhu. Passive and active droplet generation with microfluidics: a review. *Lab on a chip*, 27:42, 2017.
- [78] S. Tomotika. On the instability of a cylindrical thread of a viscous liquid surrounded by another viscous fluid. *Proc. R. Soc. Lond. A.*, 150:322–337, 1935.
- [79] Juliano Garavaglia, Melissa M. Markoski, Aline Oliveira, and Aline Marcadenti. Grape seed oil compounds: Biological and chemical actions for health. *Nutrition and Metabolic Insights*, 9:NMI.S32910, 2016.
- [80] L.R. Fisher, E.E. Mitchell, and N.S. Parker. Interfacial tensions of commercial vegetable oils with water. *Journal of Food Science*, 50(4):1201–1202, 1985.
- [81] Abir Khalil, François Puel, Yves Chevalier, Jean-Marc Galvan, Alain Rivoire, and Jean-Paul Klein. Study of droplet size distribution during an emulsification process using in situ video probe coupled with an automatic image analysis. *Chemical Engineering Journal*, 165(3):946 – 957, 2010.
- [82] Casper Ho Yin Chung, Binbin Cui, Ruyuan Song, Xin Liu, Xiaonan Xu, and Shuhuai Yao. Scalable production of monodisperse functional microspheres by multilayer parallelization of high aspect ratio microfluidic channels. *Micromachines*, 10(9):592, Sep 2019.

- [83] H. Kim et. al. Controlled production of emulsion drops using an electric field in a flow-focusing microfluidic device. *App. Physics Lett.*, 91:3, 2007.
- [84] C.H. Yeh et. al. Using an electro-spraying microfluidic chip to produce uniform emulsions under a direct-current electric field. *Microfluid Nanofluid*, 12:475–484, 2012.



---

## 7. Appendix

---

### Appendix A

Simulations of flow through a square channel and a circular channels with equal cross-areas were made to measure the pressure difference required to achieve a flow of  $1 \frac{mL}{min}$ . The simulations were run for 30 seconds. The results can be seen in Figure 7.1.

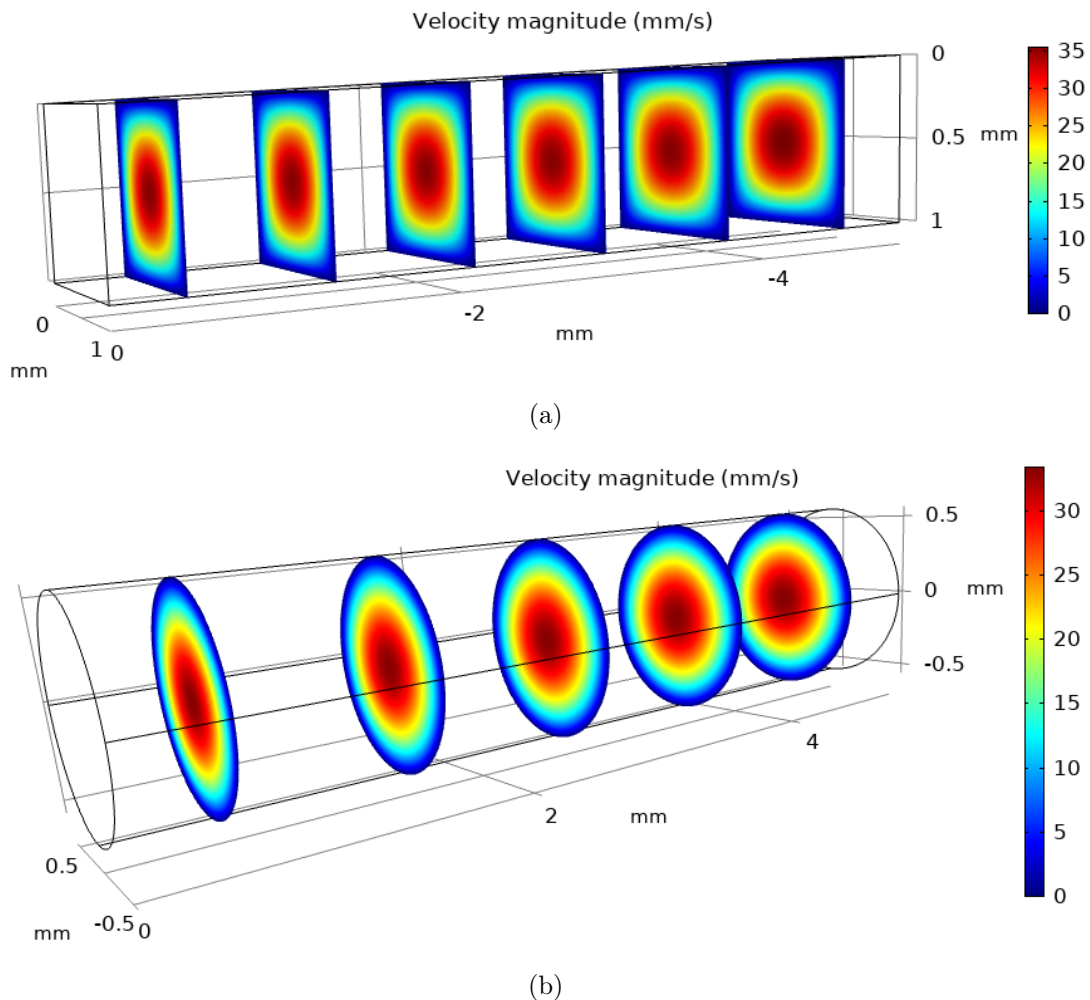


Figure 7.1: (a) Simulation of flow through a square 1mm x 1mm x 5mm channel. The simulation was run for 30 seconds using water with  $Q_{total} = 1 \frac{mL}{min}$ . The mesh consisted of 97400 elements with a MEQ of 0.4075. The simulation error is estimated to be 0.05%. (b) Simulation of flow through a circular channel with diameter 1.1284 and length 5mm. The simulation was run for 30 seconds using water with  $Q_{total} = 1 \frac{mL}{min}$ . The mesh consisted of 177936 elements with a MEQ of 0.4117. The simulation error is estimated to be 0.08%.

Figure 7.1 shows the results of simulating flow through a square and a circular channel with equal cross-areas. The pressure drop over the square channel were 2.3724 Pa compared to the 2.098 Pa pressure drop over the circular channel. Thus it requires 11.5% less pressure to achieve  $1 \frac{mL}{min}$  in the circular channel compared to the square channel.

## Appendix B

Pictures of a droplet generator before and after being submerged in 40% acetic acid for approximately 2 months. As mentioned previously the discoloration of the print is removed after an extended period in acetic acid.

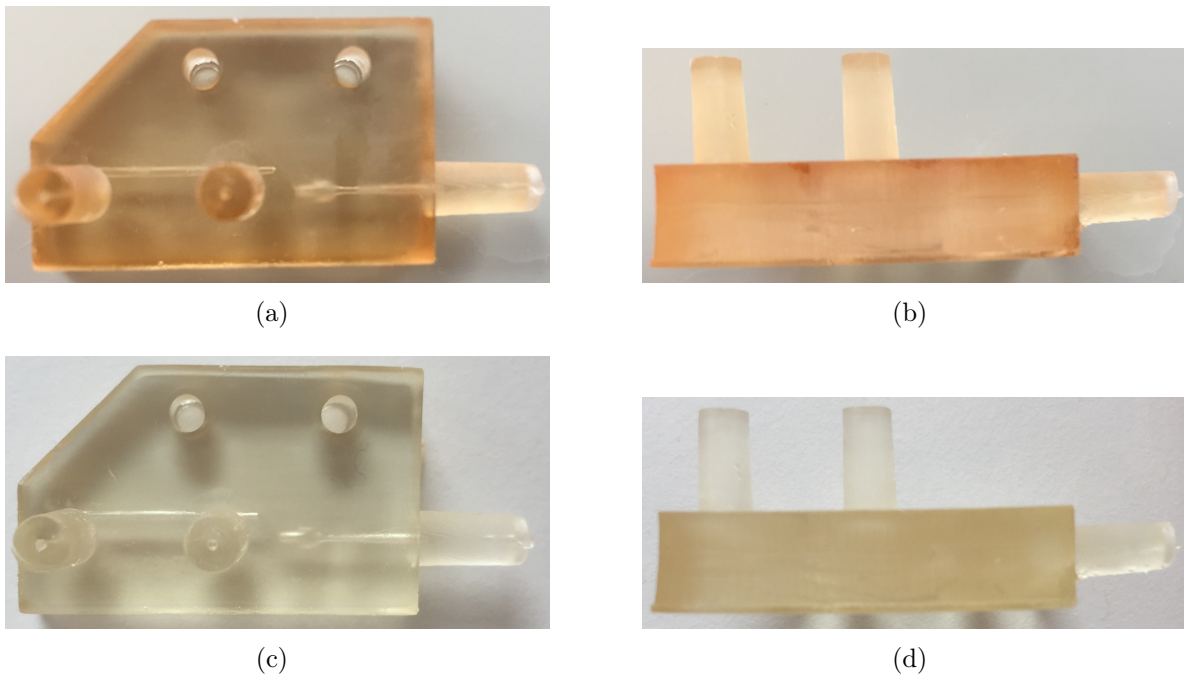


Figure 7.2: (a) top view of a droplet generator before being submerged in 40% acetic acid, (b) side view before submersion. (c) top view of the droplet generator after being submerged for approximately 2 months, (d) side view after submersion.



Figure 7.3: Side view of the cross sectional area of the droplet generator after approximately 2 months in acetic acid.

## Appendix C

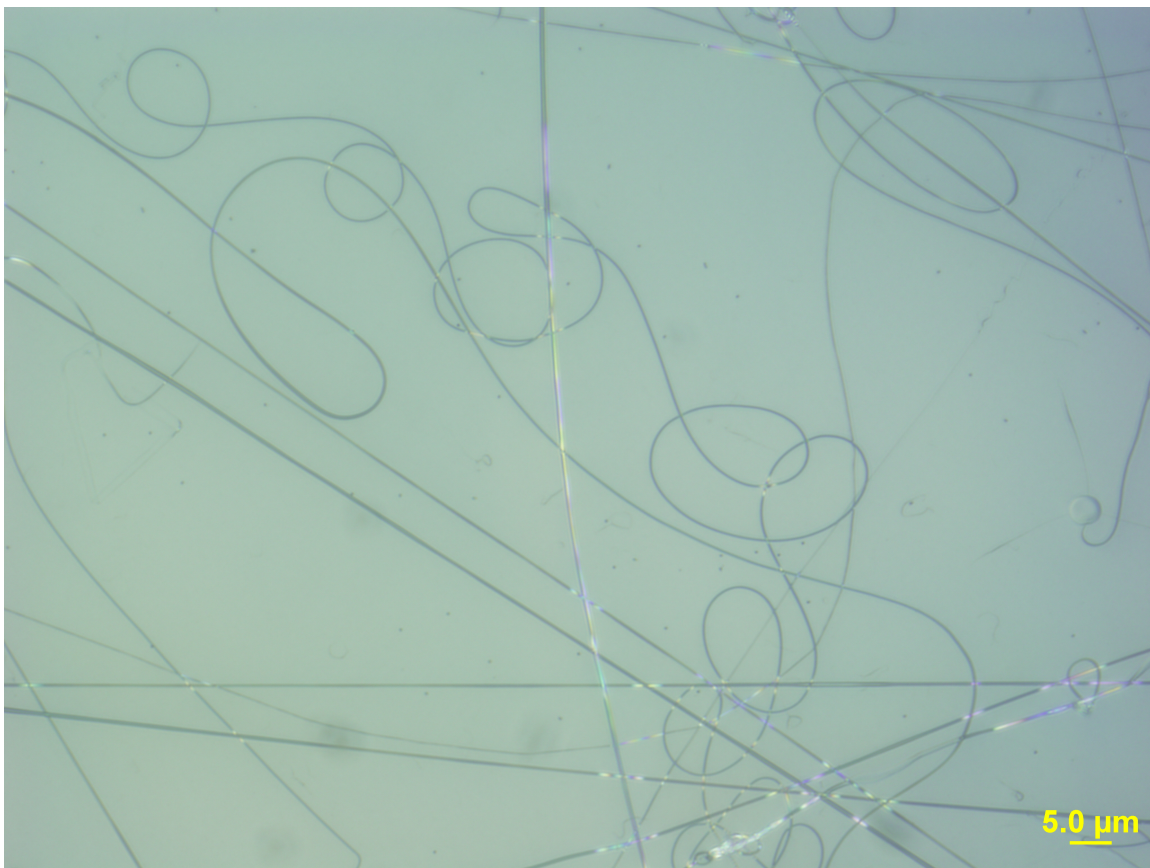


Figure 7.4: Fibers electrospun at 17-18 kV using 50  $\mu\text{l}/\text{min}$  14% PVA.